Interfaces and defects in topological model systems of 3D micro-printed waveguides

Dissertation

Christina Jörg

Vom Fachbereich Physik der Technischen Universität Kaiserslautern zur Verleihung des akademischen Grades „Doktor der Naturwissenschaften“ genehmigte Dissertation

Betreuer: Prof. Dr. Georg von Freymann
Zweitgutachter: Prof. Dr. Michael Fleischhauer

Datum der wissenschaftlichen Aussprache: 27.09.2019

D 386

Zusammenfassung

Topologische Isolatoren (TIs) stellen eine vielversprechende neue Materialklasse dar. Sie sind in ihrem Innern (genannt *bulk*) Isolatoren, also Nicht-Leiter, und besitzen somit eine Bandlücke. An der Oberfläche und den Rändern leiten sie jedoch Strom reibungsfrei. Das liegt an Randzuständen, die die Bandlücke durchqueren, und damit aufgrund ihrer Gruppengeschwindigkeit nur in eine Richtung laufen können. Diese Randzustände sind durch die Topologie des Gesamtsystems geschützt gegen Unordnung und die meisten Arten von Defekten. Unter anderem wird in dieser Dissertation untersucht, ob das auch für zeitabhängige Defekte gilt. Der robuste Transport ohne Rückstreuung macht topologische Systeme interessant für eine große Reihe von Anwendungen. Auch in der Photonik haben topologische Systeme großes Potential, z.B. für robusten Datentransfer [1–3] — auch auf der Quantenebene [4, 5] — oder für robustere photonische Instrumente [6, 7]. Mit der topologischen Photonik hat sich daher ein eigenständiges neues Forschungsfeld entwickelt [8–10].

Kontrollierbare Modellsysteme versprechen einen tieferen Einblick in die Mechanismen, die hinter topologisch geschütztem Transport stecken. Sie ermöglichen eine gute Kontrolle über einen großen Parameterbereich. Mit ihnen können unterschiedliche Gitter-Anordnungen untersucht, und sogar einzelne Gitterplätze manipuliert werden. Außerdem erlauben sie die Untersuchung von Effekten, die im Festkörper auf sehr kurzen Zeitskalen ablaufen, und damit schwer zugänglich sind. Ideal dafür geeignet sind Modellsysteme aus evaneszent gekoppelten optischen Wellenleitern. Diese Wellenleiter sind in einem Gitter angeordnet. Fokussiert man Licht in einen Wellenleiter, breitet es sich durch evanszentes Koppeln in transversaler Richtung im Gitter aus, koppelt also in die anderen Wellenleiter über. Diese transversale Verteilung ist analog zu der Ausbreitung von Elektronen, die im Atomgitter tunneln. Die Basis dafür bildet die mathematische Äquivalenz der Schrödinger Gleichung zur paraxialen Helmholtz Gleichung. Dabei wird die Zeit in der Schrödinger Gleichung ersetzt durch die Propagationsrichtung z im Wellenleiter. Dadurch können wir die zeitliche Änderung der Wellenfunktion von Elektronen im Festkörper simulieren, da sie der Verteilung des elektrischen Feldes in der Wellenleiteranordnung entlang von z entspricht.

Magnetische und elektrische Felder haben einen großen Einfluss auf Elektronen im Festkörper, jedoch kaum auf Photonen. In der photonischen Plattform müssen sie daher künstlich eingefügt werden als künstliche Eichfelder. Diese Eichfelder müssen so auf die Photonen wirken, wie ihre „echten“ elektromagnetischen Vorbilder auf die Elektronen.

Um z.B. ein photonisches Modell eines topologischen Isolators zu erhalten, krümmt man die Wellenleiter spiralförmig entlang der Propagationsachse, um den Einfluss eines magnetischen Feldes zu simulieren [3]. Daher müssen die Wellenleiter-Anordnungen dreidimensional gefertigt sein.

In dieser Arbeit wird eine neue Methode vorgestellt, um Wellenleiter 3D zu drucken. Die inverse Struktur wird mittels direktem Laserschreiben hergestellt, und nach dem Entwickeln mit einem anderen Material mit höherem Brechungsindex infiltriert. Dieses Modellsystem aus evaneszent gekoppelten Wellenleitern benutzen wir, um verschiedene Effekte in topologischen Systemen zu untersuchen. Insbesondere betrachten wir Floquet topologische Systeme, in denen die nicht-triviale Topologie durch zeitliche Modulation erzeugt wird.

Zu Beginn betrachten wir ein topologisch triviales System aus zwei gleichen Feldern von Wellenleitern mit unterschiedlichen künstlichen Eichfeldern. Die Grenzfläche zwischen diesen beiden Feldern hat einen großen Einfluss auf den transversalen Wellenvektor eines Lichtpakets, welches über diese Grenzfläche läuft. Wir leiten eine analytische Gesetzmäßigkeit für die Änderung dieses Wellenvektors, analog zum Snell'schen Brechungsgesetz, her und bestätigen sie durch Messungen.

Danach betrachten wir Floquet topologische Systeme (FTIs) aus spiralförmigen Wellenleitern, angeordnet in einem Honigwaben-Gitter. Wir finden zusätzliche triviale Randmoden am Übergang zwischen zwei FTIs mit gegensätzlicher Helizität der Wellenleiter. Damit können wir die Interaktion von topologischen und trivialen Moden untersuchen, die am gleichen Ort existieren.

Danach analysieren wir die Robustheit der topologischen Randzustände gegen zeitabhängige Defekte. Zunächst arbeiten wir mit einem 1D topologischen Modell (Su-Schrieffer-Heeger Modell [11]). Wir betrachten einen periodisch modulierten Wellenleiter am Rand zwischen zwei topologisch verschiedenen Teilen der Anordnung. Diese Modulation erzeugt Floquet Kopien vom Randzustand, die in einem bestimmten Frequenzbereich der Modulation mit Bulk-Zuständen koppeln können. Dadurch wird der Randzustand entvölkert. In einem zweidimensionalen FTI fügen wir einen einzelnen Defekt am Rand ein. Defekte mit gleicher Frequenz wie die Bulk-Wellenleiter, aber unterschiedlichem zeitlichen Verhalten beeinflussen die Randmode nicht. Das Licht läuft um den Defekt herum, oder durch ihn hindurch, ohne Rückstreuung und ohne Streuung in den Bulk. Defekte mit anderen Frequenzen verursachen jedoch Streuung des Randzustands in den Bulk.

Zum Schluss wird kurz eine neu entwickelte Methode zur Herstellung von Wellenleitern mit kleinerem Brechungsindexkontrast vorgestellt. Außerdem folgt ein Ausblick auf eine neue Art zur Erzeugung von künstlichen Eichfeldern in Wellenleiterstrukturen, durch die Ausnutzung des Bahndrehimpulses von Licht.

Abstract

Topological insulators (TI) are a fascinating new state of matter. Like usual insulators, their band structure possesses a band gap, such that they cannot conduct current in their bulk. However, they are able to conduct current along their edges and surfaces, due to edge states that cross the band gap. What makes TIs so interesting and potentially useful are these robust unidirectional edge currents. They are immune to significant defects and disorder, which means that they provide scattering-free transport.

In photonics, using topological protection has a huge potential for applications, e.g. for robust optical data transfer [1–3] — even on the quantum level [4, 5] — or to make devices more stable and robust [6, 7]. Therefore, the field of topological insulators has spread to optics to create the new and active research field of topological photonics [8–10].

Well-defined and controllable model systems can help to provide deeper insight into the mechanisms of topologically protected transport. These model systems provide a vast control over parameters. For example, arbitrary lattice types without defects can be examined, and single lattice sites can be manipulated. Furthermore, they allow for the observation of effects that usually happen at extremely short time-scales in solids. Model systems based on photonic waveguides are ideal candidates for this. They consist of optical waveguides arranged on a lattice. Due to evanescent coupling, light that is inserted into one waveguide spreads along the lattice. This coupling of light between waveguides can be seen as an analogue to electrons hopping/tunneling between atomic lattice sites in a solid. The theoretical basis for this analogy is given by the mathematical equivalence between Schrödinger and paraxial Helmholtz equation. This means that in these waveguide systems, the role of time is assigned to a spatial axis. The field evolution along the waveguides' propagation axis z thus models the temporal evolution of an electron's wave-function in solid states. Electric and magnetic fields acting on electrons in solids need to be incorporated into the photonic platform by introducing artificial fields. These artificial gauge fields need to act on photons in the same way that their electro-magnetic counterparts act on electrons. E.g., to create a photonic analogue of a topological insulator the waveguides are bent helically along their propagation axis to model the effect of a magnetic field [3]. This means that the fabrication of these waveguide arrays needs to be done in 3D.

Abstract

In this thesis, a new method to 3D micro-print waveguides is introduced. The inverse structure is fabricated via direct laser writing, and subsequently infiltrated with a material with higher refractive index contrast. We will use these model systems of evanescently coupled waveguides to look at different effects in topological systems, in particular at Floquet topological systems.

We will start with a topologically trivial system, consisting of two waveguide arrays with different artificial gauge fields. There, we observe that an interface between these trivial gauge fields has a profound impact on the wave vector of the light traveling across it. We deduce an analog to Snell's law and verify it experimentally.

Then we will move on to Floquet topological systems, consisting of helical waveguides. At the interface between two Floquet topological insulators with opposite helicity of the waveguides, we find additional trivial interface modes that trap the light. This allows to investigate the interaction between trivial and topological modes in the lattice.

Furthermore, we address the question if topological edge states are robust under the influence of time-dependent defects. In a one-dimensional topological model (the Su-Schrieffer-Heeger model [11]) we apply periodic temporal modulations to an edge waveguide. We find Floquet copies of the edge state, that couple to the bulk in a certain frequency window and thus depopulate the edge state.
In the two-dimensional Floquet topological insulator, we introduce single defects at the edge. When these defects share the temporal periodicity of the helical bulk waveguides, they have no influence on a topological edge mode. Then, the light moves around/through the defect without being scattered into the bulk. Defects with different periodicity, however, can — likewise to the defects in the SSH model — induce scattering of the edge state into the bulk.

In the end we will briefly highlight a newly emerging method for the fabrication of waveguides with low refractive index contrast. Moreover, we will introduce new ways to create artificial gauge fields by the use of orbital angular momentum states in waveguides.

Contents

1 Introduction

In 2016's announcement of the nobel prize in physics, one member of the Nobel Committee brought his lunch in form of a cinnamon bun, a bagel and a pretzel to explain topology [12]. The prize was awarded to Thouless, Haldane and Kosterlitz for theoretical discoveries made in the 1970s and 80s, that lead to "a huge amount of international research" [12] on topological systems nowadays. While it does not seem straightforward to explain topological properties of matter by comparing it to the number of holes in geometrical objects (or baked goods), it is the existence of a global invariant that is common to both. The topological invariant is a global property of a system that does not change under (small) deformations, as, for example, the actual shape of the system. Also, this global invariant allows to deduce something about local properties of the system, which is a principle called bulk-boundary correspondence. This theorem states that the difference between the topological invariants of two systems equals the number of edge states at the boundary between the systems. These topological edge states are the most apparent and eminent forms of topology. They provide scattering free transport of charge, spin or light as they are immune to defects and disorder that usually cause resistance and heat. With this property comes the hope to revolutionize electronic devices, and to use topological spin transport in spintronics [13]. In combination with superconductors, topological insulators could be the basis of new quantum computers [14, 15].

While the material sciences focus on finding new compounds of materials with topological properties, another branch of physics started to look more into the origins of topology using model systems. Among the abundance of model systems are experiments using ultracold atoms in optical lattices [16–19], optomechanics [20], coupled microwave resonators [21] (see Fig. 1.1 a)), cavity and circuit quantum electrodynamics [22], electric circuits [23–25] (see Fig. 1.1 b)), acoustic setups [26–28] (see Fig. 1.1 c)), exciton polaritons [29] and photonic systems [8–10]. This plethora of model systems shows, how universal topology is. It is inherent in all these totally different systems. With such model systems, the understanding of topological concepts and the finding of new aspects of topology gradually grows. Implementations in model systems range from 'simple' topological systems [30] and Floquet topological insulators [3] to topological insulators in synthetic dimension [31, 32], higher order topological insulators [21, 33, 34] and many more. In addition to real-space characteristics like edge modes, also band structure characteristics as Weyl points [35] and exceptional points [36] have been observed in model systems.

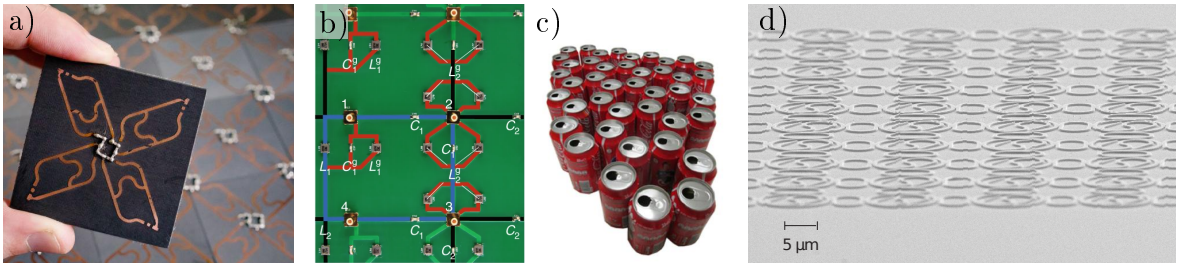

Figure 1.1: Examples of topological model systems: a) coupled microwave resonators [21] (taken from [37]), b) topolectrical circuit (taken from [24]), c) acoustic topological systems of soda cans (taken from [28] licensed under [38]), d) topological array of S-microresonators (adapted from [7]). Though these are totally different systems, they all share the underlying concept of topology.

Photonic systems are especially interesting. They do not merely serve as model systems, but topology might prove useful for photonic applications. Again, it is the topological edge states that want to be harnessed. The robust and unidirectional flow of light along edges promises to overcome limitations common to photonics that are induced by fabricational defects, disorder and back-reflection [8, 10]. The first demonstration of topological photonics suggested to use it for robust optical delay lines [2]. Also, topological edge states in photonic crystals can guide light around sharp bends and corners [39], even without the need for large refractive index contrasts [3] unlike topologically trivial photonic crystals. Another example is the concept of a topological laser, that has been shown to be robust against defects and disorder [6, 7]. Robust topological transport has also been shown to work at the quantum level with single photons [5]. Possible applications thus also include quantum information processing, sensing, and robust optical data transfer. Again, implementations in photonic systems can have many different forms. They include sytems of ring resonators [7, 30] (Fig. 1.1 d)), lattices of gyromagnetic rods [1], fibre loops [40], and plasmonic [41] and photonic [42–44] waveguides. This allows to choose the most advantageous system for each precise aspect one wants to examine, or for each application one has in mind.

In this thesis, we use photonic model systems that consist of lattices of evanescently coupled optical waveguides. Lattices of waveguides in general allow to model electronic effects in solids. This is due to the correspondence between the paraxial Helmholtz equation, describing light evolution in a waveguide and the time-dependent Schrödinger equation of the solid state system [45, 46] (chapter 2). To achieve a mathematical equivalence between the two equations we identify the waveguide's propagation axis with time. This provides an optimal access to apply temporal modulations (as done in chapter 6), as well as visualizing the evolution of states in time. Also, waveguide lattices have the advantage of single site control, as we can easily change a single waveguide by, e.g., changing its size or shifting its position. Furthermore, we work in the optical regime, such that the intensity of the wave function (i.e., its probability density) is directly observable.

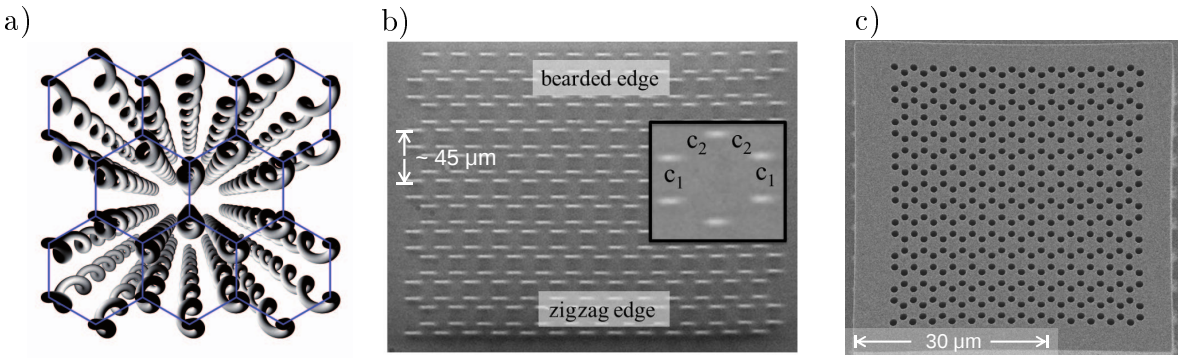

Figure 1.2: Floquet topological insulators of coupled waveguides. a) Schematic setup (taken from [3]). b) Implementation of waveguides in glass by femtosecond laser writing (adapted from [56]), c) 3D micro-printed inverse waveguide template (adapted from [57], licensed under [38]).

If we want to use waveguide lattices to mimic electronic effects in solids, we also need the fields that prevail there. Electron dynamics in solids is mainly governed by electric and magnetic fields. However, photons do scarcely interact with electro-magnetic fields. Therefore, we need to create 'artificial' gauge fields [30, 47–49], i.e., fields that have the same effect on photons (by directing their paths for example) as the corresponding electro-magnetic fields have on electrons. Raghu and Haldane [50, 51] suggested using Faraday-effect media to model magnetic fields, and to induce photonic topological edge modes in photonic crystals. Other approaches use the effects of periodic temporal modulation (Floquet) [52–54]. As we will see in chapter 2, applying these Floquet modulations allows to change the band structure of a system. Oka and Aoki proposed that the illumination of graphene with circularly polarized laser light can open a gap in graphene's band structure [55]. This approach was translated to waveguide systems and implemented in [3] to create a so-called photonic Floquet topological insulator (see Fig. 1.2). As in waveguide systems the role of time is assigned to the propagation axis z, Floquet modulations are in fact spatially periodic modulations of the waveguides in z here. Therefore, for the fabrication of such waveguide systems, we need a process that allows a truly three-dimensional fabrication of waveguides.

One possibility is to use femtosecond laser writing in glass [46, 58, 59]. Focused femtosecond laser pulses locally change the refractive index of fused silica by about $\Delta n \approx 10^{-4}$, which allows to create elliptical waveguides with a three-dimensional trajectory (see Fig. 1.2 b)). In this thesis, we use a different method: 3D micro-printing of structures in polymer [60, 61], also known as direct laser writing (DLW) [62–68]. Via DLW the inverse template of the waveguide array is created, i.e., only the material surrounding the waveguides is polymerized (see Fig. 1.2 c)). After development, the sample is then infiltrated with another photoresist to create the actual waveguides. This approach has the advantage that we can fabricate waveguides with almost arbitrary trajectories and a proper circular cross-section. This way we ensure isotropic coupling of light from one waveguide to its neighbors. Also, the infiltration step makes

it possible to use a wide range of different materials with different optical properties (see section 7.1).

Using this model system of 3D micro-printed waveguides we examine one aspect of topological robustness: the effects of interfaces and time-dependent defects on topological edge modes. As the robustness of a topological edge mode is the key criterion for possible applications, we set out to explore how far this robustness holds.

Structure of the thesis

We start with the general theory of waveguide model systems and topology, needed to understand the rest of the thesis, in chapter 2. The fabrication process of the waveguide samples as well as experimental methods are explained in chapter 3.

In chapter 4 we explore the effect of an interface between two trivial, but different artificial gauge fields on a wave traveling across it. Those artificial gauge fields are achieved by tilting the waveguides in one array with respect to the other. In all other aspects (e.g. size of the waveguides and material) the arrays are identical. Still, we find that such an interface alters the properties of a wave packet crossing it.

In chapter 5 we look at the interface between two photonic Floquet topological insulators (FTIs) with opposite sign of the topological invariant. Interestingly, at the interface between our two photonic FTIs we can trap a trivial mode that oscillates between the edges of that interface.

This motivates us to shrink one of the FTIs into a single waveguide, rotating differently from the rest of the lattice. We examine under which circumstances such a time-dependent defect alters the properties of a topological edge mode in chapter 6.

In the end, in chapter 7, we give an outlook to a different method to create artificial gauge fields, using states carrying orbital angular momentum of light. Also, we introduce a new single-step fabrication process for the creation of waveguides.

2 Theory

In this thesis we use waveguide structures as model systems to study electronic effects in solids. We will point out the analogy between these two systems in sections 2.1 and 2.3. In particular, we will use the waveguide system to look at topological effects. The concept of topology will be introduced in section 2.4 and specified to Floquet topological systems in sections 2.5-2.7. In the end, we will go through the example of a Floquet-modulated honeycomb lattice, as it will be of importance for the following chapters in this thesis.
Here and in the following we set $\hbar = 1$.

2.1 Why can we use waveguides?

The waveguides that we are going to use are cylindrical step index waveguides. They consist of a core made of a material with a higher refractive index than its surrounding. Light is guided inside the core region due to total internal reflection (Fig. 2.1 a)). Outside the core, the wave's amplitude decreases exponentially.

Light propagation inside a waveguide can be mathematically described by the paraxial Helmholtz equation. It can be derived from Maxwell's equations found in textbooks (e.g. [69]). We will skip the first part of the derivation (if interested, see section 2.1 in [69]) and start with the wave equation in a non-homogeneous but non-magnetic medium without sources or currents

$$\underbrace{2\boldsymbol{\nabla}\left(\boldsymbol{E}\cdot\boldsymbol{\nabla}\ln\sqrt{\epsilon_\mathrm{r}}\right)}_{\approx 0}+\nabla^2\boldsymbol{E}=\left(\frac{n(x,y)}{c}\right)^2\frac{\partial^2}{\partial t^2}\boldsymbol{E}. \tag{2.1}$$

Here, $\boldsymbol{E}$ is the electric field, $\boldsymbol{\nabla}$ is the gradient, time is t, ϵ_r is the material's relative permittivity, $n(x,y)$ is the refractive index depending on the spatial coordinates x and y, and c is the vacuum speed of light. The first term accounts for vectorial parts of the wave function and is, e.g., important for the description of orbital angular momentum as in section 7.1. However, if we consider single-mode waveguides with a small refractive index contrast to their surrounding, the first term tends to zero. Thus, we can neglect it for most parts of this thesis and use the scalar wave equation only.

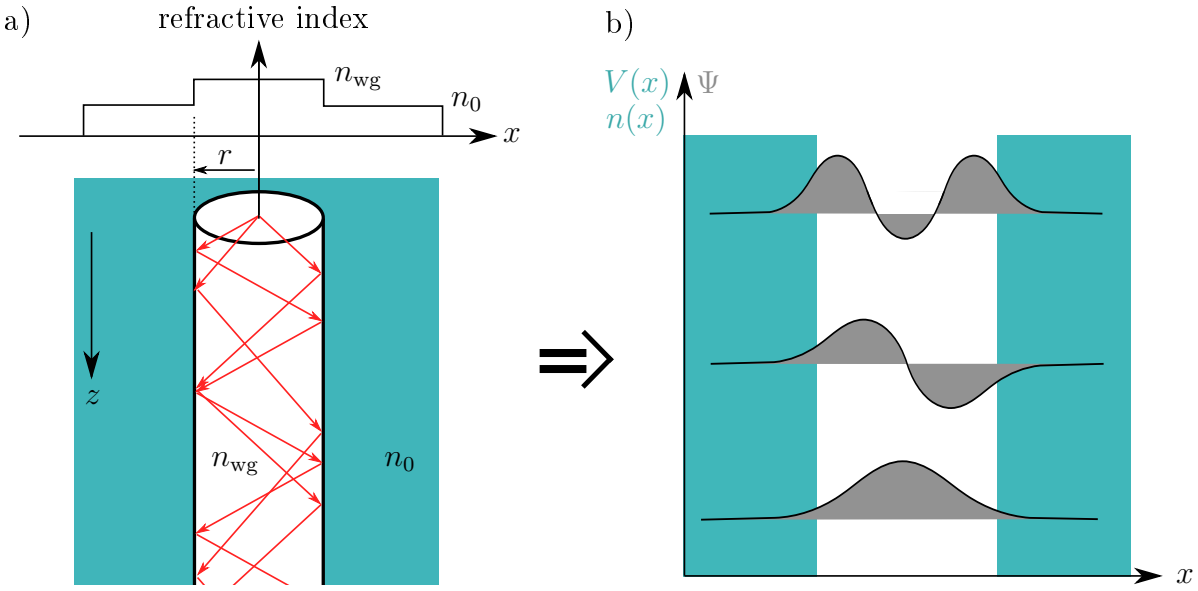

Figure 2.1: A waveguide with refractive index contrast is equivalent to a potential well. a) Cylindrical waveguide with radius r. The refractive index of the core is n_{wg} and the one of the cladding n_0. Light is guided inside the core region along z due to total internal reflection. b) In the modal picture, a waveguide is a potential well with potential $V(x)$ given by the refractive index change in $n(x)$. The fundamental mode in a cylindrical potential is a Gaussian. Outside the potential well, the amplitude of the wave function decreases exponentially.

We assume that there is a main axis of propagation along the waveguide, such that the angle between the light's wave-vector $\boldsymbol{k}$ and the waveguide axis is small. Then we can split the electric field $\boldsymbol{E}$ into a term Ψ, describing the amplitude part that varies slowly in the axial (z) direction, and a term that oscillates with the wave's frequency ω

$$\boldsymbol{E}(x, y, z, t) = \Psi(x, y)\, e^{\mathrm{i}(\beta z - \omega t)}\, \hat{\boldsymbol{e}}_x. \tag{2.2}$$

Here, the polarization was chosen to be in the $\hat{\boldsymbol{e}}_x$-direction. The phase constant $\beta = \frac{2\pi}{\lambda} n_{\text{eff}}$ of the light propagating in the waveguide is the z-component of the wave-vector propagating in a material with an effective refractive index n_{eff} and wavelength λ. As light is not strictly confined to the waveguide area with refractive index n_{wg}, but evanescently decays into the surrounding material with n_0, the effective refractive index is $n_0 < n_{\text{eff}} < n_{\text{wg}}$.

Inserting Eq. (2.2) into (2.1) and neglecting the vectorial term in Eq. (2.1) yields

$$\nabla^2 \Psi + 2\mathrm{i}\beta \frac{\partial \Psi}{\partial z} - \beta^2 \Psi = -n^2(x, y) \frac{\omega^2}{c^2} \Psi. \tag{2.3}$$

If Ψ changes slowly along the distance $1/\beta$ in z, then $|\frac{\partial^2 \Psi}{\partial z^2}| \ll |2\mathrm{i}\beta \frac{\partial \Psi}{\partial z}|$. This means

that we can neglect the term $\frac{\partial^2\Psi}{\partial z^2}$ in the Laplacian, and Eq. (2.3) transforms into the paraxial Helmholtz equation

$$\mathrm{i}\frac{\partial\Psi}{\partial z} = -\left[\frac{1}{2\beta}\nabla_\perp^2 + \frac{1}{2\beta}\left(n^2(x,y)\frac{\omega^2}{c^2} - \beta^2\right)\right]\Psi, \tag{2.4}$$

with the transversal gradient $\nabla_\perp$ acting in the x- and y-direction.

This equation is mathematically analog to the Schrödinger equation

$$\mathrm{i}\frac{\partial\Psi}{\partial t} = -\left[\frac{1}{2m}\nabla_\perp^2 + V(x,y)\right]\Psi \tag{2.5}$$

for electrons of mass m in a potential well V (Fig. 2.1 b)). The equivalence holds if we map time onto the spatial z-axis [46]. In this thesis, we will use t and z synonymously.

We see that the refractive index contrast

$$V(x,y) = \frac{\beta}{2}\frac{n^2(x,y) - n_{\mathrm{eff}}^2}{n_{\mathrm{eff}}^2} \tag{2.6}$$

in Eq. (2.4) plays the role of a potential for light. For $n_{\mathrm{eff}} \approx n_0$, i.e., small refractive index contrast between waveguide and surrounding material, the potential is zero everywhere but at the sites of the waveguides[(1)]

$$V(x,y) = \begin{cases} \frac{k_0}{2}\frac{n_{\mathrm{wg}}^2 - n_0^2}{n_0^2} & \text{for } x,y \text{ inside the waveguide} \\ 0 & \text{otherwise,} \end{cases} \tag{2.7}$$

with $k_0 = n_0 2\pi/\lambda$. Eq. (2.4) then is approximated by

$$\mathrm{i}\frac{\partial\Psi}{\partial z} = -\frac{1}{2k_0}\left[\nabla_\perp^2 + k_0^2\frac{n^2(x,y) - n_0^2}{n_0^2}\right]\Psi. \tag{2.8}$$

What we have obtained by now is a Schrödinger-like equation for a single waveguide, modeling a single electron in a potential well. By itself, this would be rather boring. The interesting single-particle effects in solid states arise from the interplay of many lattice sites. In the following section we will review how we can combine single sites and deduce an effective model for a lattice of potential wells. In the end, we will be able to formulate a Hamiltonian of the system based on an effective hopping model.

(1) If $n_{\mathrm{eff}} \approx n_0$ does not hold, we basically have a positive potential at the sites of the waveguides and a negative one in the surrounding material. We can then add a constant offset to the potential, such that we can still write the spatially dependent part of the potential as in Eq. (2.7).

2.2 Effective hopping model

Since most concepts in solid state physics can be well described by the Schrödinger equation, we can apply the same mechanisms for treating the waveguide system as we can for treating potential wells. Although the derivation is done in the language of solid states, following [70], it maps to waveguide systems equivalently. We will comment on that in section 2.3.

We start with the time-dependent Schrödinger equation

$$\mathrm{i}\partial_t|\psi\rangle = H|\psi\rangle, \tag{2.9}$$

with the Hamiltonian H of a single lattice site

$$H = \frac{p^2}{2m} + V(\boldsymbol{r}). \tag{2.10}$$

As usual, p is the momentum and m the mass of a particle, and $\boldsymbol{r} = (x, y)$. We assume that the solution of this single-particle equation $H\varphi_n = E_n\varphi_n$ is already known for all quantum numbers n. We now want to move to a (two-dimensional) lattice of potentials, where the electron at each site is influenced by the potential at the other lattice sites $\boldsymbol{R}$

$$H = \frac{p^2}{2m} + \sum_{\boldsymbol{R}} V(\boldsymbol{r} - \boldsymbol{R}) = H_0(\boldsymbol{R}) + \sum_{\boldsymbol{R'} \neq \boldsymbol{R}} V(\boldsymbol{r} - \boldsymbol{R'}), \tag{2.11}$$

where $\boldsymbol{R}$ is a lattice vector. The first part H_0 will give us the eigenenergy E_0 of the atomic wave function at its own lattice site, while the second term is the influence of the other lattice sites and will be treated as a perturbation. This perturbation leads to a splitting of energy levels into the ones for anti-symmetric and symmetric wave functions with lower and higher energy. For a system consisting of enough lattice sites, these energy levels are spaced closely and thus form bands. If we only consider uncoupled sites, the eigenstates of the Hamiltonian in Eq. (2.11) are the eigenstates of each uncoupled atom $\varphi_n(\boldsymbol{r})$. We can then use them to construct Bloch-wave functions for N lattice sites:

$$\Psi_{n,\boldsymbol{k}}(\boldsymbol{r}) = \frac{1}{\sqrt{N}} \sum_{\boldsymbol{R}} \exp\left(\mathrm{i}\boldsymbol{k} \cdot \boldsymbol{R}\right) \varphi_n(\boldsymbol{r} - \boldsymbol{R}) \tag{2.12}$$

with

$$\Psi_{n,\boldsymbol{k}}(\boldsymbol{r} + \boldsymbol{R}) = \exp\left(\mathrm{i}\boldsymbol{k} \cdot \boldsymbol{R}\right) \Psi_{n,\boldsymbol{k}}(\boldsymbol{r}). \tag{2.13}$$

For the coupled sites, these Bloch functions are no longer eigenstates of the Hamiltonian

in Eq. (2.11), and moreover are not orthogonal to each other[2]

$$\begin{aligned}\langle\Psi_{n,\boldsymbol{k}}|\Psi_{n',\boldsymbol{k}}\rangle &= \frac{1}{N}\sum_{\boldsymbol{R}_1,\boldsymbol{R}_2}\exp\left(\mathrm{i}\boldsymbol{k}\cdot(\boldsymbol{R}_1-\boldsymbol{R}_2)\right)\int \mathrm{d}^2r\ \varphi_n^*(\boldsymbol{r}-\boldsymbol{R}_2)\ \varphi_{n'}(\boldsymbol{r}-\boldsymbol{R}_1)\\ &= \delta_{n,n'}+\sum_{\boldsymbol{R}\neq 0}\exp\left(-\mathrm{i}\boldsymbol{k}\cdot\boldsymbol{R}\right)\alpha_{n,n'}(\boldsymbol{R}).\end{aligned} \tag{2.14}$$

In the last equality we have set $\boldsymbol{R}_1 = 0$ and $\boldsymbol{R}_2 = \boldsymbol{R}$ without loss of generality. $\alpha_{n,n'}$ is the overlap integral between the two wave functions

$$\alpha_{n,n'} = \int \mathrm{d}^2r\ \varphi_n^*(\boldsymbol{r}-\boldsymbol{R})\ \varphi_n(\boldsymbol{r}). \tag{2.15}$$

Nevertheless, we can use the constructed Bloch functions of Eq. (2.12) as an approximation of the exact eigenstates.

Now we apply perturbation theory. The energies are then given by

$$\varepsilon_n(\boldsymbol{k}) = \frac{\langle\Psi_{n,\boldsymbol{k}}|H|\Psi_{n,\boldsymbol{k}}\rangle}{\langle\Psi_{n,\boldsymbol{k}}|\Psi_{n,\boldsymbol{k}}\rangle} = E_n + \frac{E_n^{\mathrm{pert}}(\boldsymbol{k})}{\langle\Psi_{n,\boldsymbol{k}}|\Psi_{n,\boldsymbol{k}}\rangle} \tag{2.16}$$

with

$$\begin{aligned}E_n^{\mathrm{pert}}(\boldsymbol{k}) = \frac{1}{N}\sum_{\boldsymbol{R}_1,\boldsymbol{R}_2}&\exp\left(\mathrm{i}\boldsymbol{k}\cdot(\boldsymbol{R}_1-\boldsymbol{R}_2)\right)\\ &\int \mathrm{d}^2r\ \varphi_n^*(\boldsymbol{r}-\boldsymbol{R}_2)\sum_{\boldsymbol{R}_3\neq\boldsymbol{R}_1} V(\boldsymbol{r}-\boldsymbol{R}_3)\ \varphi_n(\boldsymbol{r}-\boldsymbol{R}_1).\end{aligned} \tag{2.17}$$

We now consider three cases for E_n^{pert}:
1) $\boldsymbol{R}_1 = \boldsymbol{R}_2 \neq \boldsymbol{R}_3$: 
(wave functions at the same site, potential at another)
The overlap of the wave functions is large. Then the contribution to E_n^{pert}

$$\begin{aligned}E_{\mathrm{offs}} &= \frac{1}{N}\sum_{\boldsymbol{R}_1}\int \mathrm{d}^2r\ \varphi_n^*(\boldsymbol{r}-\boldsymbol{R}_1)\sum_{\boldsymbol{R}_3\neq\boldsymbol{R}_1} V(\boldsymbol{r}-\boldsymbol{R}_3)\ \varphi_n(\boldsymbol{r}-\boldsymbol{R}_1)\\ &= \int \mathrm{d}^2r\ \varphi_n^*(\boldsymbol{r})\sum_{\boldsymbol{R}_3\neq 0} V(\boldsymbol{r}-\boldsymbol{R}_3)\ \varphi_n(\boldsymbol{r})\end{aligned} \tag{2.18}$$

is the expectation value of the potential of all other sites, acting upon lattice site $\boldsymbol{R}_1$. It only gives a constant offset to the energy, as it is not dependent on $\boldsymbol{k}$, and the same

[2] For a waveguide system this non-orthogonality was shown to lead to deviations of the experiments from theoretical calculations using coupled mode theory [71].

for all lattice sites.

2) $\boldsymbol{R}_2 = \boldsymbol{R}_3 \neq \boldsymbol{R}_1$: 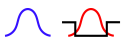
The overlap between one wave function and the potential is large. The energy

$$\begin{aligned}&\frac{1}{N}\sum_{\boldsymbol{R}_1\neq\boldsymbol{R}_2}\exp\left(\mathrm{i}\boldsymbol{k}\cdot(\boldsymbol{R}_1-\boldsymbol{R}_2)\right)\int \mathrm{d}^2r\ \varphi_n^*(\boldsymbol{r}-\boldsymbol{R}_2)V(\boldsymbol{r}-\boldsymbol{R}_2)\ \varphi_n(\boldsymbol{r}-\boldsymbol{R}_1)\\ &=\sum_{\boldsymbol{R}\neq 0}\exp\left(-\mathrm{i}\boldsymbol{k}\cdot\boldsymbol{R}\right)\int \mathrm{d}^2r\ \ \varphi_n^*(\boldsymbol{r}-\boldsymbol{R})V(\boldsymbol{r}-\boldsymbol{R})\ \varphi_n(\boldsymbol{r})=\sum_{\boldsymbol{R}\neq 0}\exp\left(-\mathrm{i}\boldsymbol{k}\cdot\boldsymbol{R}\right)J(\boldsymbol{R})\end{aligned} \tag{2.19}$$

forms the band structure and includes an effective hopping term J.

3) $\boldsymbol{R}_1 \neq \boldsymbol{R}_2 \neq \boldsymbol{R}_3 \neq \boldsymbol{R}_1$: 
All overlaps are small. Therefore, we can neglect this term.

In addition, from now on we consider only sums over nearest neighbor sites (such that $\boldsymbol{R}$ has the size of one lattice vector), as we assume that the wave functions decay rapidly outside their potential well. This is called the tight binding approximation. Then it follows that

$$\varepsilon_n(\boldsymbol{k}) = E_n + \frac{E_{\text{offs}} + \sum_{\boldsymbol{R}\neq 0}\exp\left(-\mathrm{i}\boldsymbol{k}\cdot\boldsymbol{R}\right)J(\boldsymbol{R})}{1+\sum_{\boldsymbol{R}\neq 0}\exp\left(-\mathrm{i}\boldsymbol{k}\cdot\boldsymbol{R}\right)\alpha(\boldsymbol{R})}. \tag{2.20}$$

The second term in the denominator does not vanish, as the constructed Bloch functions are not orthogonal (see also [71]). Instead, we can use the Wannier functions, that build an orthonormal basis, and are constructed of the Bloch functions

$$w_n(\boldsymbol{r}-\boldsymbol{R}) = \frac{1}{\sqrt{N}}\sum_{\boldsymbol{k}}\exp\left(-\mathrm{i}\boldsymbol{k}\cdot\boldsymbol{R}\right)\Psi_{n,\boldsymbol{k}}(\boldsymbol{r}). \tag{2.21}$$

As they are orthogonal, the denominator of Eq. (2.20) now is 1 and we obtain

$$\varepsilon_n(\boldsymbol{k}) = \tilde{E}_n + \sum_{\boldsymbol{R}\neq 0}\exp\left(-\mathrm{i}\boldsymbol{k}\cdot\boldsymbol{R}\right)\tilde{J}(\boldsymbol{r}), \tag{2.22}$$

where

$$\tilde{E}_n = \int \mathrm{d}^2r\ w_n^*(\boldsymbol{r})\left(\frac{p^2}{2m}+\sum_{\boldsymbol{R}}V(\boldsymbol{r}-\boldsymbol{R})\right)\ w_n(\boldsymbol{r}) \tag{2.23}$$

is the energy of the atom at site 0 including the offset by the neighboring potentials

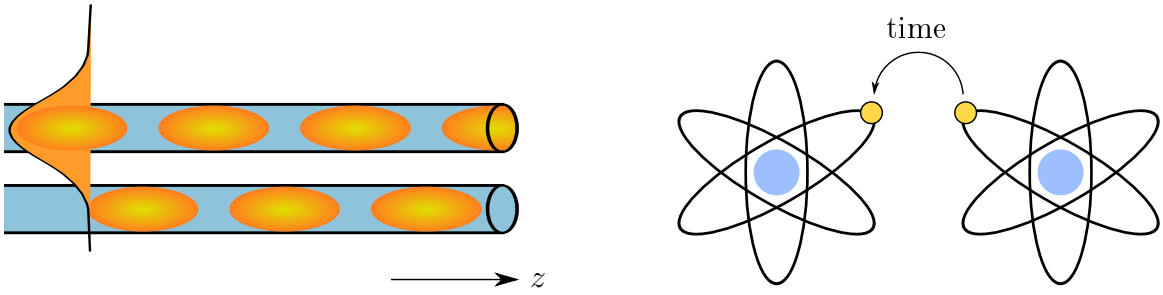

Figure 2.2: Light can couple evanescently between two closely spaced waveguides. Sketched is the intensity distribution. The coupling along z (left) models the hopping of electrons between atomic sites in time t (right).

and

$$\tilde{J} = \int \mathrm{d}^2 r \; w_n^*(\boldsymbol{r} - \boldsymbol{R}) V(\boldsymbol{r} - \boldsymbol{R}) \; w_n(\boldsymbol{r}) \tag{2.24}$$

is the hopping rate between neighboring lattice sites. We see that due to the hopping terms, we obtain a band structure that indicates the energies possible for a certain lattice wave vector $\boldsymbol{k}$.

We now have transformed the Schrödinger equation of coupled atoms into a tight binding form of the Schrödinger equation, where influences of neighboring sites are absorbed in the hopping. As we will only consider single-mode waveguides in the following, we drop the index n. Referring to second quantization for the wave functions we can write the Hamiltonian as

$$H = \sum_i \tilde{E} \hat{a}_i^\dagger \hat{a}_i + \sum_{i,j} \tilde{J}_{i,j} \hat{a}_i^\dagger \hat{a}_j + \text{h.c.}, \tag{2.25}$$

where the operator $\hat{a}_i^\dagger$ ($\hat{a}_i$) creates (annihilates) a particle at lattice site i that can be reached via $\boldsymbol{R}_i$, and the sum is only over nearest neighbors.

2.3 Analogy to the waveguide model system

We have seen in section 2.1 that the paraxial Helmholtz equation describes light propagation inside a waveguide, and that it is equivalent to the Schrödinger equation. In the previous section we derived an effective hopping rate for a lattice model. We now want to identify the corresponding variables in a lattice of coupled waveguides.

In a waveguide light is guided with a certain propagation constant $\gamma = \alpha + \mathrm{i}\beta$, where the attenuation constant α describes the damping of the light's amplitude along its

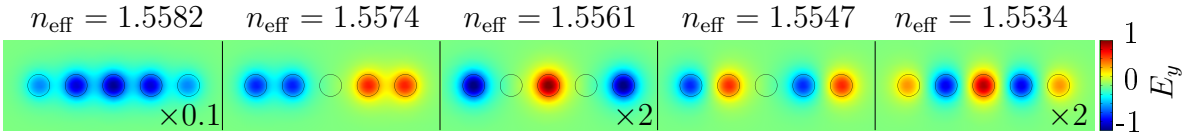

Figure 2.3: Supermodes in a linear array of five coupled waveguides. All waveguides are equal and equally spaced. Color codes the amplitude of the electric field component E_y. Where indicated, the field was scaled for better visibility. For a single waveguide with the same parameters the effective refractive index is $n_{\text{eff}} = 1.5561$. The calculation of the supermodes was done using *COMSOL*'s eigenmode solver in the package "electromagnetic waves, beam envelopes".

propagation and β is the phase constant. We will neglect α in the following and refer to β only, when we talk about the propagation constant[3].

The eigenmodes of a cylindrical waveguide are transverse electromagnetic modes, with a corresponding propagation constant β. The fundamental mode, i.e. the one with lowest β, has a Gaussian shape. For a single-mode fiber the phase constant can be written as $\beta_0 = \frac{2\pi}{\lambda} n_{\text{eff}}$, with the effective refractive index n_{eff} and the wavelength λ. The propagation constant β_0 thus describes in which length along z the phase of the wave changes by 2π. It is equivalent to the eigenenergy E_0 of an atomic wave function at its own lattice site (the term E_n in Eq. (2.20)).

Light can be guided inside the core region as long as $\frac{2\pi}{\lambda} n_0 < \beta_0 < \frac{2\pi}{\lambda} n_{\text{wg}}$. Outside the core material, the amplitude of the light is decaying exponentially. If a second waveguide is placed in close vicinity to the first one, it can pick up the decaying field, such that the light couples to this second waveguide (similar to frustrated total internal reflection; see Fig. 2.2). This is called evanescent coupling. In a system of two equal waveguides, two new supermodes form: one with symmetric and one with anti-symmetric amplitude distribution (see also Fig. 2.3 for supermodes in five waveguides).

We can describe the amplitudes $E_{1,2}(z)$ along z in waveguide 1 and 2 by two coupled differential equations [72, 73]

$$\mathrm{i}\frac{dE_1}{dz} = J_{21} E_2(z) + \beta_0 E_1(z), \tag{2.26a}$$

$$\mathrm{i}\frac{dE_2}{dz} = J_{12} E_1(z) + \beta_0 E_2(z), \tag{2.26b}$$

for equal waveguides, where β_0 is the single waveguide's propagation constant and

[3] We can neglect α either if it is very small, or if all the waveguides in an array are equal, such that the damping is an overall effect without influence on the intensity distribution between waveguides.

$J_{21} = J_{12}^* =: J$ is the coupling between the waveguides. In the notation of a Hamiltonian, we can write

$$\mathrm{i}\frac{d}{dz}\begin{pmatrix} E_1 \\ E_2 \end{pmatrix} = \begin{pmatrix} \beta_0 & J \\ J^* & \beta_0 \end{pmatrix}\begin{pmatrix} E_1 \\ E_2 \end{pmatrix}. \tag{2.27}$$

J measures the evanescent overlap between the fields in the two waveguides and the potential given by the refractive index contrast, similar to Eq. (2.24),

$$J = \iint E^*(x+d,y)V(x+d,y)E(x,y)\ \mathrm{d}x\ \mathrm{d}y. \tag{2.28}$$

In general this is an integral depending on the exact fields E and geometry of the waveguides (see, e.g. [72–74]). It decays exponentially with the distance d between the waveguides. Therefore, we can express J as

$$J = p_1 \exp\left(-p_2 d\right), \tag{2.29}$$

where p_1 and p_2 are two parameters that depend on the waveguide radii, the wavelength of light, and the refractive indices. Due to the exponential decay, in general we only consider coupling between nearest-neighboring waveguides.

The eigenvalues of the Hamiltonian in Eq. (2.27) $\beta_{\mathrm{s,as}} = \beta_0 \pm |J|$ are the propagation constants of the symmetric and anti-symmetric supermode[(4)]. Thus, we can determine the coupling constant J by calculating the propagation constant for the symmetric and anti-symmetric supermode of two coupled waveguides:

$$|J| = (\beta_{\mathrm{s}} - \beta_{\mathrm{as}})/2. \tag{2.30}$$

For a 1D lattice of infinitely many equal waveguides we obtain a cosine-shaped band of the propagation constants β of the supermodes. Usually, we set β_0 to zero for a lattice of equal waveguides, as it only amounts in a constant offset to all β. For unequal waveguides, we can not do so, as they do not share a common β_0. Then, the differences from β_0 for the single waveguides enter the Hamiltonian as on-site potentials on its diagonal.

For a 2D square lattice of equal waveguides the tight-binding Hamiltonian reads

$$H = \sum_{i,j} J_x \hat{a}_{i,j}^\dagger \hat{a}_{i+1,j} + J_y \hat{a}_{i,j}^\dagger \hat{a}_{i,j+1} + \mathrm{h.c.} \tag{2.31}$$

(4) β is bigger (smaller) than β_0 for the symmetric (anti-symmetric) mode. This is exactly opposite for symmetric and anti-symmetric wave functions in atomic lattices. However, note that we associate the propagation constant with negative energy (see also [61], chapter 3.1).

atomic lattice	waveguide lattice
potential	refractive index
time	propagation distance z
(negative) energy	propagation constant β
quasimomentum q	transversal wave vector k

Table 2.1: Quantities in the waveguide lattice corresponding to the quantities of an atomic lattice.

with the hopping $J_{x,y}$ between the waveguides in x- and y-direction. The eigenenergies of this Hamiltonian form a band structure, equivalent to that in solids, where now the energy is replaced by β and the lattice wave vector components are replaced by the transversal wave vector components of the light k_x, k_y at a fixed wavelength λ. Note that this means that the wavelength can also be used as a variable to tune through different sections of the band structure, see section 6.2 and [75].

The transversal wave vector component k_x (k_y) in a waveguide lattice corresponds to a phase difference between the light in neighboring waveguides in the x- (y)-direction. Thus, we can excite a certain wave vector component by coupling into several waveguides with the proper phase distribution. Note that we obtain a two-dimensional band structure for a three-dimensional waveguide structure, as the z-direction is taken to be time. It is a transversal band structure that only describes the transversal dynamics, i.e., the coupling of the light in the x- and y-direction. In z the light still propagates as usual.

Thus, the field evolution in the x-y-plane along the waveguides' propagation axis z models the temporal evolution of an electronic wave-function in a 2D lattice in solid states. As photons are (non-interacting) bosons, this only works for models where the electrons' interactions are disregarded. Including interactions into the photonic models, e.g. by using Kerr-nonlinear materials, is the scope of future work.

Nevertheless, lattices of evanescently coupled waveguides are ideally suited to observe a vast range of intriguing effects [45, 46, 60, 61]. To just name a few, implementations range from the observation of Bloch oscillations [76, 77] and modulation assisted tunneling [59] to Anderson localization [78], Rashba pseudo-spin-orbit coupling [48], photonic graphene [43], and all kinds of topological systems [3, 34, 41, 42, 44, 57, 75, 79–84]. As parameters can be tuned easily, they are highly controllable model systems. They allow for single-site control, and single defects can be included at will. Additionally, they provide optimal access to 'time', as it is mapped to a spatial axis. This allows to observe effects of temporal modulation, as we will do in chapter 6. An overview of corresponding quantities between waveguide and atomic lattices is given in Table 2.1.

In the course of this thesis, we will use the waveguide model system to look at topological effects. In the next sections, we want to briefly introduce the concepts of topology that will be important for the rest of the thesis.

2.4 Topology

The field of topology in physics emerged with the discovery of the Quantum Hall effect. 1980 von Klitzing observed a quantized Hall resistivity in a two-dimensional electron gas in the inversion layer of a MOSFET (silicon metal-oxide-semiconductor field-effect transistor) using a strong magnetic field and low temperatures [85, 86]. Laughlin [87] and Thouless [88] related this phenomenon to topological charge pumping, and showed that the Hall conductivity must be quantized. Coinciding with the plateaus of the quantized Hall resistance, the longitudinal resistance vanishes. This is a result from chiral edge channels. The key argument is that a strong magnetic field forces the electrons in the bulk to move in cyclotron orbits. The electrons at the edge, however, cannot complete a full orbit, but rather move by a half orbit [89]. This leads to a chiral current along the edges.

An extension of this Integer Quantum Hall effect is the Quantum Spin Hall effect (QSH). Predicted by Kane and Mele [90], Molenkamp *et al.* [91] proved experimental evidence of unidirectional spin currents along the edges of mercury telluride quantum wells. Depending on the thickness of the well, spin-orbit coupling can lead to band inversion and thus induce non-trivial topology. In fact, in solids states the term 'topological insulator' (TI) refers to systems in which opposite spins propagate in the opposite chiral direction. In that case, the surface states are protected by time-reversal (TR) symmetry. These systems are characterized by a $\mathbb{Z}_2$ invariant, meaning that the topological invariant can only take two different integer values (by convention often 0 and 1). In photonics we are a bit sloppy with the term TI and often refer to Quantum-Hall-like systems, that are characterized by an integer $\mathbb{Z}$ invariant. These systems should more correctly be called Chern insulators, as TR-symmetry needs to be broken to obtain them.

An overview of topological invariants for different dimensional systems are given in the periodic table for topological invariants [92]. There, the systems are grouped according to their symmetries. We will therefore give a very brief introduction into the relevant symmetries in the following section.

2.4.1 Symmetries

The relevant symmetries for the classification of topological systems in the periodic table [92] are time-reversal (TR) symmetry, particle-hole (P) symmetry, and chiral (C) symmetry. We will introduce these three symmetries below (see also [93] for a rigorous definition). In general, however, more symmetries can be present in a system. According to [94] "for every discrete symmetry, there must exist topological insulating phases with distinct physical properties and a topological number that classifies these phases and distinguishes them from the 'trivial' ones". We will see that this is, for example, the case for graphene in a perpendicular AC-field.
In addition to the symmetry of the system, also the square of the symmetry operator will discriminate between different topological phases.

Time-reversal symmetry

If a Hamilton operator $\hat{H}$ has TR symmetry, we can find an anti-unitary operator $\hat{\mathscr{T}}$, such that

$$\hat{\mathscr{T}}\hat{H}\hat{\mathscr{T}}^{-1} = \hat{H}. \tag{2.32}$$

The many-body Hamiltonian $\hat{H}$ can be written in terms of the single-particle Hamiltonian matrix H and the creation (and annihilation) operators $\hat{a}^\dagger$ ($\hat{a}$) as

$$\hat{H} = \sum_{ij} \hat{a}_i^\dagger H_{ij} \hat{a}_j. \tag{2.33}$$

We can then express the effect of time-reversal symmetry of the single-particle Hamiltonian in momentum space as

$$\mathscr{T} H^*(\boldsymbol{k}) \mathscr{T}^{-1} = H(-\boldsymbol{k}), \tag{2.34}$$

where $\mathscr{T}$ (without hat) is now a matrix, such that $\hat{\mathscr{T}}\hat{a}_i\hat{\mathscr{T}}^{-1} = \sum_j \mathscr{T}_{ij}\hat{a}_j$ [93]. In case of spinless particles we can denote $\mathscr{T}$ to be complex conjugation $\mathscr{T} = \mathscr{K}$. This means that the Hamiltonian must be real symmetric, as it follows from Eq. (2.34) that $\mathscr{K}H\Psi = H\mathscr{K}\Psi$ which leads to $H^*\Psi^* = H\Psi^*$ [95]. Furthermore, for every eigenstate $\Psi(\boldsymbol{k})$ of $H(\boldsymbol{k})$, there must be a time-reversed partner eigenstate $\mathscr{T}\Psi(\boldsymbol{k})$ of $H(-\boldsymbol{k})$ at the same energy. This implies inversion symmetry of the energies, $E(\boldsymbol{k}) = E(-\boldsymbol{k})$[5].

We discriminate between two distinct cases of TR symmetry: For fermions $\mathscr{T}\mathscr{T}^* = -1$ which leads to the QSH effect. A photonic implementation was done in [84], but most

[5] The reverse conclusion is not correct: inversion symmetry of the energies does not necessarily imply TR symmetry.

of the times fermionic TR symmetry is not possible for photonic systems. For them, as for all bosonic systems, $\mathscr{T}\mathscr{T}^* = 1$ applies.

We will see in section 2.4.2, why TR symmetry-breaking plays an important role to obtain non-trivial topology in photonic systems.

Particle-hole symmetry

Particle-hole symmetry is mainly relevant for superconducting systems. If a system exhibits particle-hole symmetry, we can find an anti-unitary operator $\hat{\mathscr{P}}$ which anti-commutes with the Hamiltonian. As is the case for TR symmetry, $\mathscr{P}$ can square to $+1$ and -1.

Chiral symmetry

If the system is chiral symmetric, there exists a unitary operator $\hat{\mathscr{C}}$ such that the Hamiltonian of the system obeys

$$\hat{\mathscr{C}}\hat{H}\hat{\mathscr{C}}^{-1} = -\hat{H}. \tag{2.35}$$

This means that the energy spectrum is mirror symmetric around $E = 0$, as every state with eigenenergy E has a chiral symmetric partner with $-E$. A state at $E = 0$ then is its own chiral symmetric partner. In a lattice with two sites per unit cell, this state can occupy only one sublattice, which is why this symmetry is also called sublattice symmetry [95]. Chiral symmetry must always be present if both particle-hole and and time-reversal symmetry are present, as $\hat{\mathscr{C}} = \hat{\mathscr{P}} \cdot \hat{\mathscr{T}}$. The matrix $\mathscr{C}$ always squares to one.

Chiral symmetry protects the topology of the one-dimensional SSH model, which will be introduced in section 6.2. In the two-dimensional systems, that we will look at in sections 5, 6.1 and 6.3, the breaking of time-reversal symmetry is required to obtain non-trivial topology. In the Quantum Hall effect, this was achieved by a magnetic field. Haldane later developed a simple model for a "zero-field quantum Hall effect" [96], nowadays called "quantum anomalous Hall effect" or Chern insulator [97]. The Haldane model will be described in the following chapter.

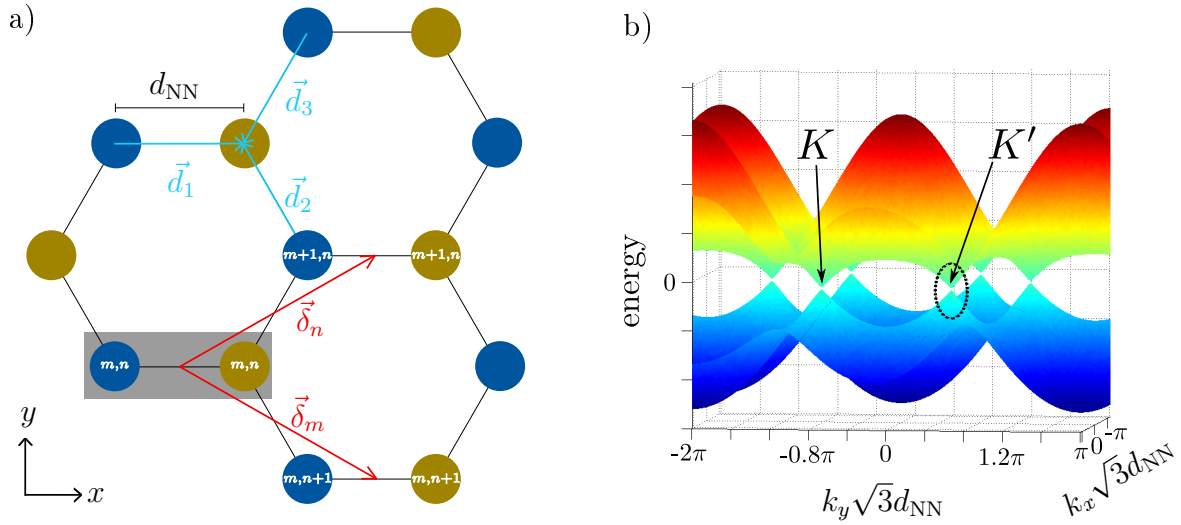

Figure 2.4: a) Sketch of the honeycomb lattice. blue: a-sites, yellow: b-sites. The lattice vectors are $\boldsymbol{\delta}_m$ and $\boldsymbol{\delta}_n$, and distances between nearest neighbors $\boldsymbol{d}_{1,2,3}$ with absolute value d_{NN}. The unit cell is highlighted in grey. b) Band structure of graphene, considering only nearest neighbor coupling. The dashed ellipse marks one of the Dirac cones (adapted from [60]).

2.4.2 The Haldane model

Haldane started from a model of graphene, which is a monolayer of carbon atoms, arranged on a honeycomb lattice. Fig. 2.4 shows the sketch of a honeycomb lattice. This lattice contains two sites, dubbed a and b, in one unit cell enumerated by the indexes m and n. The vectors

$$\boldsymbol{\delta}_n = \left(3, \sqrt{3}\right)\frac{d_{\mathrm{NN}}}{2}, \quad \text{and} \quad \boldsymbol{\delta}_m = \left(3, -\sqrt{3}\right)\frac{d_{\mathrm{NN}}}{2} \tag{2.36}$$

span the lattice in real-space, such that each site can be reached by

$$\boldsymbol{R} = n\boldsymbol{\delta}_n + m\boldsymbol{\delta}_m. \tag{2.37}$$

d_{NN} is the absolute value of the distance between nearest neighboring sites.

In a tight-binding approach we can describe the dynamics in the system by a set of equations

$$\mathrm{i}\partial_t a_{m,n} = J_1 b_{m,n} + J_2 b_{m+1,n} + J_3 b_{m,n-1} \tag{2.38a}$$

$$\mathrm{i}\partial_t b_{m,n} = J_1^* a_{m,n} + J_2^* a_{m-1,n} + J_3^* a_{m,n+1} \tag{2.38b}$$

where J_1, J_2 and J_3 are the nearest neighbor hopping terms from one site to its neighbor. For the moment, we will neglect the next-nearest neighbor hoppings. $a_{m,n}$ ($b_{m,n}$) measures the complex amplitude of the field at site $a_{m,n}$ ($b_{m,n}$).

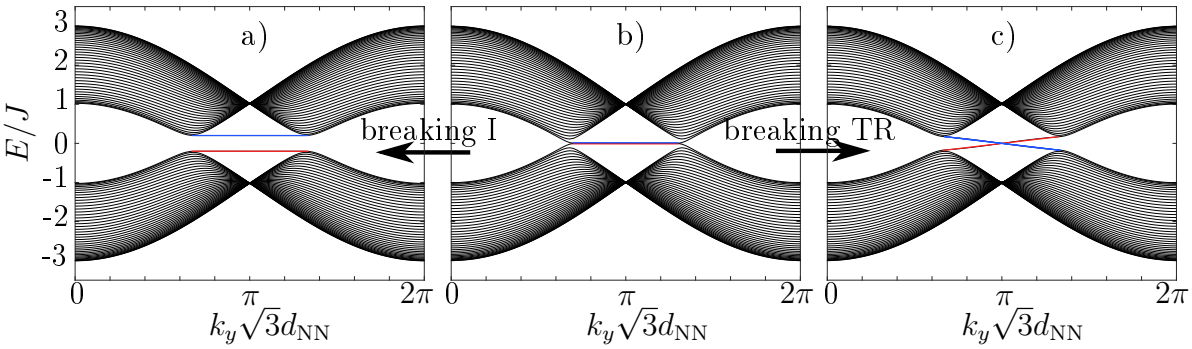

Figure 2.5: Projected band structure of the honeycomb lattice with broken inversion symmetry I (a) and broken time-reversal symmetry TR (c). In this example there are two edge states: one for the left zigzag edge of the sample (marked in red), and one for the right zigzag edge (blue).

To calculate the band structure from these equations, we go into k-space and write

$$a_{m,n} = \sum_{k_m,k_n} a_k \exp\left(\mathrm{i}k_m m + \mathrm{i}k_n n\right) \tag{2.39}$$

and analogous for $b_{m,n}$. Then Eq. (2.38) is simplified to

$$\mathrm{i}\partial_t \begin{pmatrix} a_k \\ b_k \end{pmatrix} = H \begin{pmatrix} a_k \\ b_k \end{pmatrix} \qquad \text{with} \qquad H = \begin{pmatrix} 0 & \Delta_{k_n,k_m} \\ \Delta^*_{k_n,k_m} & 0 \end{pmatrix} \tag{2.40}$$

and

$$\Delta_{k_n,k_m} = J_1 + J_2 \exp\left(\mathrm{i}k_m\right) + J_3 \exp\left(-\mathrm{i}k_n\right). \tag{2.41}$$

If $J := J_1 = J_2 = J_3$, then Δ_{k_n,k_m} takes the simple form

$$\Delta_{k_n,k_m} = J \sum_j \exp(\mathrm{i}\boldsymbol{k} \cdot \boldsymbol{d}_j) \tag{2.42}$$

with $\boldsymbol{k} = (k_x, k_y)$ and $\boldsymbol{d}_{1,2,3}$ from Fig. 2.4 a). The eigenvalues $E(\boldsymbol{k}) = \pm|\Delta_{k_n,k_m}|$ of H yield the band structure (see Fig. 2.4 b)) of graphene. Two in-equivalent Dirac cones are present in the band structure at the two high-symmetry points K and K'. For a finite system, zero energy edge states appear in the band structure (blue and red in Fig. 2.5 b)). Such edge states can be located at the bearded or zigzag edges of the structure in real-space (see Fig. 2.6 b)). At the armchair edge, no edge states exist for the simple honeycomb lattice.

Haldane realized, that there are two different ways to open a band gap in graphene (see Fig. 2.5). Breaking inversion symmetry opens a gap at the Dirac cones, but

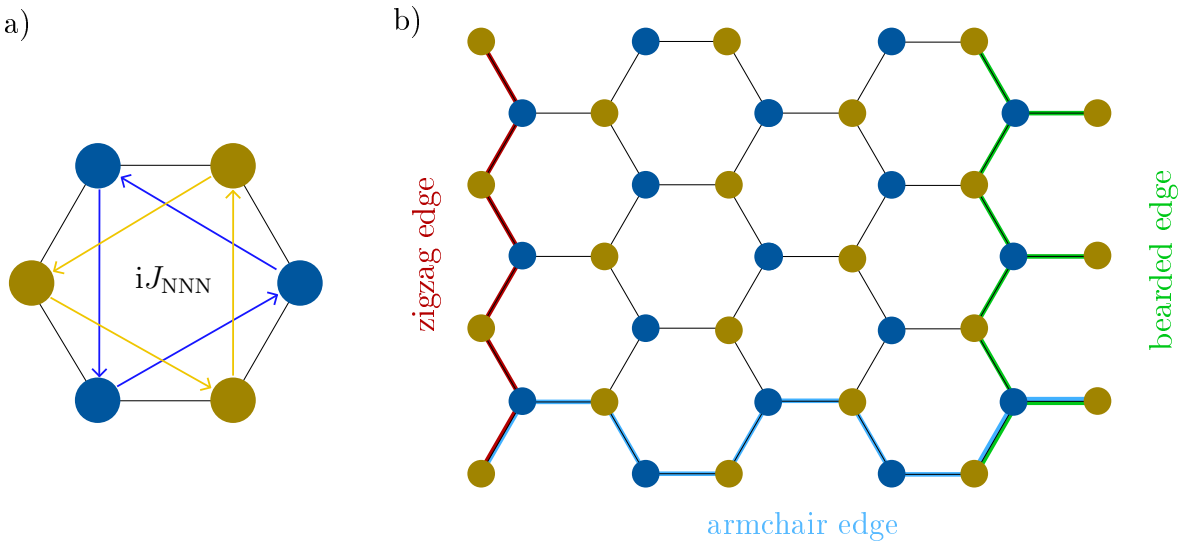

Figure 2.6: a) Complex next-nearest neighbor coupling iJ_{NNN} in a honeycomb cell. b) Possible edge configurations in a honeycomb lattice: zigzag, armchair and bearded edge. Adapted from [43].

does not induce non-trivial topology. The edge states do not traverse the band gap, but remain localized. Breaking TR symmetry instead, leads to a Chern insulator. Haldane incorporated the TR breaking in graphene by adding a complex next-nearest neighbor hopping (Fig. 2.6 a)). This adds a chiral term to the Hamiltonian, as now hopping forwards and backwards is not the same. For a next-nearest neighbor hopping exceeding a certain value the gap closes at one of the two Dirac points and re-opens again, yielding non-trivial topology and chiral[6] edge states (Fig. 2.5 c))[7].

To see why this makes the system topologically non-trivial, we first introduce a way to characterize topology, in form of topological invariants.

Berry phase, Berry connection and Berry potential

Consider an eigenstate $|\Psi\rangle$ of a quantum system without degeneracy. Now, we change an external parameter adiabatically in time. M. Berry [98] realized that this eigenstate would, after completing a closed loop in the space of the external parameter, pick up a phase [99], the so-called Berry phase γ (in addition to the usual dynamic phase ϕ_{dyn}), such that

$$|\Psi\rangle \to \exp(i\gamma)\exp(i\phi_{\text{dyn}})|\Psi\rangle. \tag{2.43}$$

[6] meaning that the edge states encircle the structure; not to be confused with chirally symmetric

[7] Now, in principle, we can have chiral edge states for all three edge types, including the armchair edge.

Zak transferred the concepts of the Berry phase to the dynamics of electrons in a periodic potential in solids [100]. He considered an eigenstate $|\Psi_n(\boldsymbol{k})\rangle$, belonging to the nth band of a Hamiltonian with non-degenerate eigenenergies. The external parameter is now the crystal momentum $\boldsymbol{k}$. Due to the periodicity of the Brillouin zone, sweeping $\boldsymbol{k}$ through the entire Brillouin zone corresponds to a closed loop. As noted in [99], this is the only way to realize a closed loop in a 1D parameter space. In such one-dimensional systems, the Berry phase in lattices is commonly called Zak phase. However, in other dimensional systems it is still named Berry phase, even when specifically referring to Zak's specification in periodic potentials, which we will follow in this section.

The Berry phase is a geometric phase and can be written as an integral over a closed curve $\mathcal{C}$ in k-space

$$\gamma_n(\mathcal{C}) = \oint_{\mathcal{C}} \mathrm{d}\boldsymbol{k} \cdot \boldsymbol{\mathcal{A}}_n(\boldsymbol{k}) \tag{2.44}$$

with a kind of vector potential $\boldsymbol{\mathcal{A}}$ in k-space. This vector potential is the Berry connection

$$\boldsymbol{\mathcal{A}}_n(\boldsymbol{k}) = -\mathrm{i}\langle\Psi_n(\boldsymbol{k})|\boldsymbol{\nabla}_{\boldsymbol{k}}\Psi_n(\boldsymbol{k})\rangle \tag{2.45}$$

and basically measures the change of the wave function, when we change $\boldsymbol{k}$ slightly, with respect to the original wave function. Here, we also see that we encounter a problem in the definition of the Berry connection when we come to a point where energies are degenerate, as we can not clearly define which band the state has to follow upon a slight change of $\boldsymbol{k}$ (see also [99]). Therefore, we can consider the Dirac points, at which the two bands of graphene become degenerate, as the sources of a 'Berry flux', similar to the concept of magnetic monopoles.

The curl of the Berry connection is the Berry curvature

$$\boldsymbol{\Omega}_n(\boldsymbol{k}) = \boldsymbol{\nabla} \times \boldsymbol{\mathcal{A}}_n(\boldsymbol{k}). \tag{2.46}$$

If we consider the Berry connection as a vector potential, the Berry curvature has the role of a magnetic field [101].

Now we can define the topological invariant of our system, the Chern number C, via the Berry phase or the surface integral of the Berry curvature over the Brillouin zone (BZ)

$$2\pi C_n = \iint_{\mathrm{BZ}} \boldsymbol{\Omega}_n(\boldsymbol{k}) \cdot \mathrm{d}\boldsymbol{k} = \gamma_n(2\pi) - \gamma_n(0). \tag{2.47}$$

The gap Chern number C then is the sum of the Chern numbers C_n of all bands below the band gap. As we only have one band below the gap in the Haldane model, it equals the Chern number of the lower band. For non-zero values of C our system exhibits

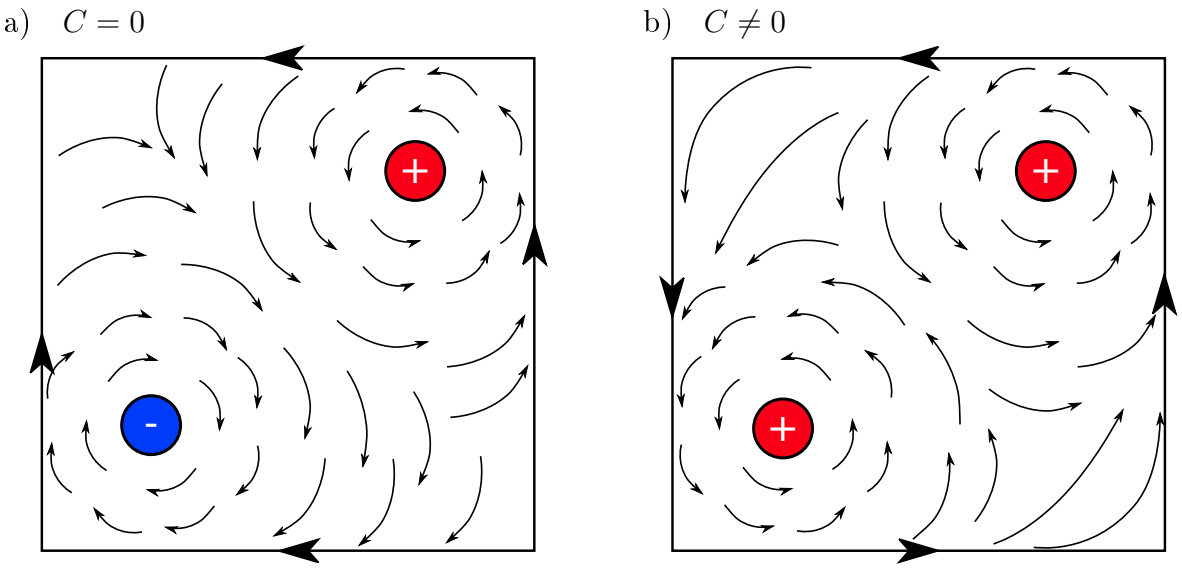

Figure 2.7: Sketch of the connection between Berry curvature and Chern number. Red (blue) circle represent positive (negative) Berry curvature, small arrows represent the Berry connection, and the sum of the large arrows at the circumference of the square (Brillouin zone) represents the Chern number. a) $C = 0$ for unequal Berry curvatures, b) $C \neq 0$ for equal Berry curvatures.

non-trivial topology. In the case of the Haldane model this happens for $C = \pm 1$. If $C = 0$, we have just a usual insulator.

As we can see in Fig. 2.7, the Chern number is non-zero when the Berry curvatures of both Dirac points K and K' are equal. However, applying the TR symmetry operator flips the sign of the Berry curvature (see Eq. (2.46)) and also that of $\boldsymbol{k}$. In case the system is TR symmetric, this means that the Berry curvatures at both Dirac cones must be un-equal and cannot lead to non-trivial topology. Thus Haldane correctly realized that the breaking of TR symmetry is a pre-requisite to obtain a topologically non-trivial system for the honeycomb lattice.

According to the bulk-edge correspondence [94, 95] the number of edge modes traversing the band gap (counted per chirality) is equal to the gap Chern number. This number of chiral edge states can only change with a change in the topological invariant, i.e., when the band gap closes and re-opens. Therefore, it is a 'protected' quantity. The topology of a system is a global quantity, and cannot be changed by local static perturbations that do not close the band gap. So is the number of edge states. Due to their unidirectionality, they are also protected from backscattering [1, 3], and thus immune to many defects. These robust edge states most of the times are the main reason of interest in topology. In photonics, they promise more robust optical devices [2, 4, 5, 7][(8)].

(8) Note that in photonics, topological edge states are not protected against general losses. While scattering into the bulk is mostly suppressed by a band gap, photons can still experience the intrinsic loss of the material, bending losses etc.

As we saw, we can obtain these chiral edge states by breaking TR symmetry. Haldane himself, however, stated in his paper that the complex hopping would be "unlikely to be directly physically realizable" [96]. In 2009 Oka and Aoki [55] proposed an alternative approach. They showed that the opening of a non-trivial gap in graphene can also be induced by irradiating graphene with circularly polarized light. The corresponding topological systems are called Floquet topological insulators. We will later see that this approach is actually closely connected to the Haldane model. But first, let us review the Floquet theorem.

2.5 Floquet theory

Floquet theory helps us to study systems with a time-periodic driving [102]. The Floquet theorem [102–106] is valid for a matrix — or in our case a Hamiltonian — that is periodic in time $H(t+T) = H(t)$ with a period $T = 2\pi/\omega$. Then, one can re-write the time-dependent states into a superposition of Floquet-states [104]

$$|\psi_\alpha(t)\rangle = \exp\left(-\mathrm{i}\varepsilon_\alpha t\right)|u_\alpha(t)\rangle, \tag{2.48}$$

that solves the time-dependent Schrödinger equation. ε_α is the quasienergy, that is only defined up to integer multiplies of the driving frequency ω due to the periodicity in time. $|u_\alpha(t+T)\rangle = |u_\alpha(t)\rangle$ is a T-periodic Floquet mode, which is an element of the extended Hilbert space $\mathbb{H} \otimes \mathbb{T}$, a direct product of the usual Hilbert space $\mathbb{H}$ and the space of time-periodic functions with period T, or "multi-photon-dressed states" [55].

Inserting Eq. (2.48) into the Schrödinger equation, yields

$$\left(H(t) - \mathrm{i}\frac{\partial}{\partial t}\right)|u_\alpha(t)\rangle = \varepsilon_\alpha|u_\alpha(t)\rangle. \tag{2.49}$$

Fourier-decomposition of the Hamiltonian as well as the Floquet modes

$$H(t) = \sum_{n=-\infty}^{\infty} \mathrm{e}^{-\mathrm{i}n\omega t}H^{(n)}, \tag{2.50a}$$

$$|u_\alpha(t)\rangle = \sum_{n=-\infty}^{\infty} \mathrm{e}^{-\mathrm{i}n\omega t}|u_\alpha^{(n)}\rangle, \tag{2.50b}$$

follows

$$\left(H^{(0)} - n\omega\right)|u_\alpha^{(n)}\rangle + \sum_{m\neq 0} H^{(m)}|u_\alpha^{(n-m)}\rangle = \varepsilon_\alpha|u_\alpha^{(n)}\rangle, \qquad \forall n, m \in \mathbb{Z}. \tag{2.51}$$

This means, that we have copies (replicas) of the original term $H^{(0)}$ shifted by integer

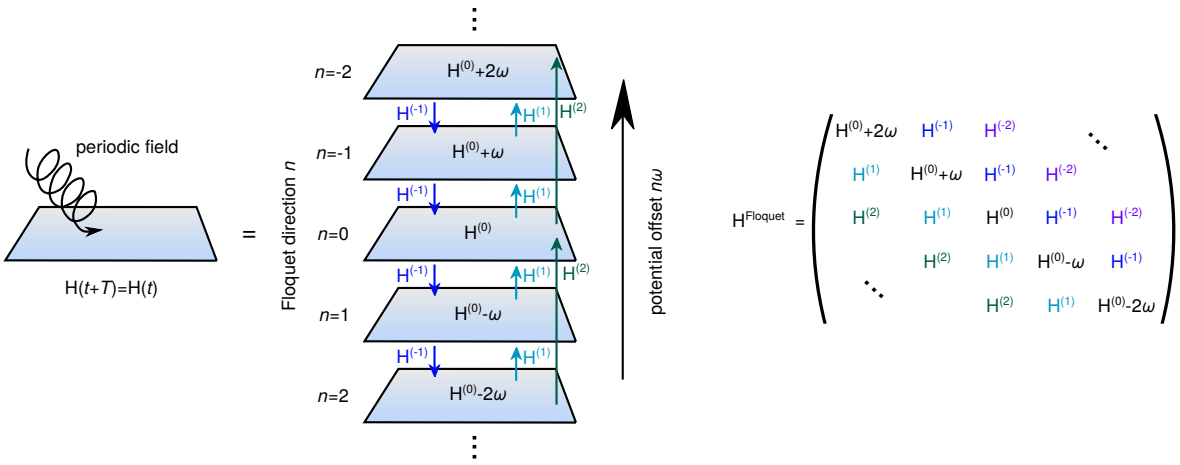

Figure 2.8: Graphical representation of Eq. (2.51), adapted from [107].

multiples of the frequency $n\omega$ in its on-site potential (n is the Floquet index). Additionally, we obtain a coupling term $H^{(m)}$ between different orders of replicas. This coupling can be responsible for opening additional band gaps in case that the energy between different replicas coincide. Eq. (2.51) is graphically represented in Fig. 2.8.

We see that Floquet theory allows us to transform a d-dimensional time-dependent equation into a $(d+1)$D time-independent one.

2.6 Floquet topological insulators

Floquet topological insulators make use of time-periodic driving to create non-trivial topology in a system. This happens as the Floquet drive 'reshuffles' the bands [53], as we now have to consider 'photon'-dressed states. In principle, the Hamiltonian of the Floquet TI is time-dependent. However, most of the times, we can then calculate an effective static Hamiltonian that captures the system's topology, and that yields a Chern number. In some cases, this Chern number is zero, but still edge states are present. Then we are in the regime of anomalous Floquet TIs [108, 109]. This can happen as the quasi-energy ε in Floquet systems is periodic, as we have seen in the previous section. Then an edge state can leave the energy range (the Floquet Brillouin zone) at the bottom and re-enter from above. Thus, we cannot really define a lower band in the Floquet picture, for which we calculate the Chern number. Instead, we have to use a different topological invariant, the winding number, that correctly captures the topology of the Floquet system. In contrast to the Chern number, the winding number depends on the full time evolution of the system during one driving period (see also [108] for its definition). Such an anomalous Floquet TI has, e.g., been implemented in a photonic system based on waveguides [44, 81].

For large enough frequency of the driving (the driving frequency is much larger than the energy scale of the system), however, we can, as said above, just use the effective static Hamiltonian. We obtain it by introducing a unitary time-evolution operator

$$U(t,0) = \mathcal{T} \exp\left(-\mathrm{i}\int_0^t H(t')\mathrm{d}t'\right) \tag{2.52}$$

with the time-ordering operator $\mathcal{T}$. $U(t,0)$ helps us solve for the eigenstates of the Schrödinger equation with

$$|\Psi(t)\rangle = U(t,0)|\Psi(0)\rangle. \tag{2.53}$$

Due to the time-ordering operator, $U(t,0)$ is not easy to calculate analytically. However, for large frequencies of the driving, we can just look for stationary states, i.e., eigenstates of the driven system after one period T

$$U(t+T,t)|\Psi\rangle = \exp(-\mathrm{i}\varepsilon T)|\Psi\rangle. \tag{2.54}$$

The effective stationary Hamiltonian H_{eff} is then defined via the Floquet operator

$$U(T,0) = \exp(-\mathrm{i}H_{\text{eff}}T). \tag{2.55}$$

This means that we content ourselves with evaluating the system stroboscopically once per driving cycle. Note that H_{eff} actually lives in the Hilbert space $\mathbb{H}$, not the extended Floquet Hilbert space $\mathbb{H} \otimes \mathbb{T}$ [110].

There exist several methods to obtain the effective Hamiltonian from the time-dependent one. Very often, the Floquet-Magnus expansion [111] is used. While it is suitable for many applications, higher order terms in $1/\omega$ are hard to compute. The same problem arises for the van Vleck degenerate perturbation theory. Therefore, we will follow the Brillouin-Wigner theory introduced by Mikami *et al.* [110]. It will also allow us to get a better picture of the physics behind the model of graphene irradiated by circularly polarized light.

In the Brillouin-Wigner (BW) theory, the Hamiltonian of the system is projected from $\mathbb{H} \otimes \mathbb{T}$ to an effective Hamiltonian in a subspace of $\mathbb{H}$. Following Floquet theory, it arrives at an effective Hamiltonian that depends on the eigenenergy self-consistently, but that can be expanded for high frequencies to remove this self-consistency. In particular, for a Hamiltonian in a non-interacting system

$$H(t) = \sum_{i,j} J_{i,j}(t)\hat{a}_i^\dagger \hat{a}_j \tag{2.56}$$

with a time-periodic hopping $J_{i,j}(t+T) = J_{i,j}(t)$, the BW theory yields [110]

$$H_{\mathrm{BW}} = \sum_{i,j} \left(J_{i,j}^{(0)} + J_{i,j}^{(1)} + J_{i,j}^{(2)} \right) \hat{a}_i^\dagger \hat{a}_j + J\mathcal{O}\left(\frac{J^3}{\omega^3}\right) \tag{2.57}$$

with

$$J_{i,j}^{(0)} = J_{i,j}^{0}, \tag{2.58a}$$

$$J_{i,j}^{(1)} = \sum_{n\neq 0} \sum_{k} \frac{J_{i,k}^{(-n)} J_{k,j}^{(n)}}{n\omega}, \tag{2.58b}$$

$$J_{i,j}^{(2)} = \sum_{n\neq 0} \sum_{k,l} \left(\sum_{m\neq 0} \frac{J_{i,k}^{(-m)} J_{k,l}^{(m-n)} J_{l,j}^{(n)}}{mn\omega^2} - \frac{J_{i,k}^{(-n)} J_{k,l}^{(n)} J_{l,j}^{(0)}}{n^2\omega^2} \right). \tag{2.58c}$$

Here,

$$J_{i,j}^{(m-n)} = \frac{1}{T} \int_0^T \mathrm{d}t J_{i,j}(t) \exp(\mathrm{i}(m-n)\omega t) \tag{2.59}$$

are the Floquet components of the hopping amplitude $J_{i,j}(t)$.

Before we can treat our actual problem of the Floquet-modulated honeycomb lattice in section 2.8, we still need to find out, how we can explicitly write down the time-dependent Hamiltonian. One way is to use the Peierls substitution.

2.7 Peierls substitution

We consider here a vector field $\boldsymbol{A}$. In the Hamiltonian it enters by minimal substitution

$$H = \frac{(\boldsymbol{p} + e\boldsymbol{A})^2}{2m} + V(\boldsymbol{r}) \tag{2.60}$$

with the electric charge e.

For a potential $V(\boldsymbol{r})$ at $\boldsymbol{r} = 0$ the eigenfunction of H is $\Psi_0(\boldsymbol{r})$, and regarded as independent of a magnetic field in the tight-binding limit. However, for a potential at a different site $V(\boldsymbol{r} - \boldsymbol{R})$, the eigenfunction can not just be $\Psi_0(\boldsymbol{r} - \boldsymbol{R})$, as the vector potential at that site may differ. Peierls [112] stated that we can apply a gauge transformation such that we obtain the same form of the Hamiltonian at all sites, if

we take

$$\boldsymbol{A} \to \boldsymbol{A} + \boldsymbol{\nabla}\Lambda(\boldsymbol{r}), \quad \text{and} \tag{2.61a}$$

$$\Psi \to \Psi \exp(\mathrm{i}\Lambda(\boldsymbol{r})). \tag{2.61b}$$

For a spatially homogeneous $\boldsymbol{A}$, i.e. vanishing magnetic field, we can choose

$$\Lambda(\boldsymbol{r}) := e\boldsymbol{A}(t) \cdot \boldsymbol{r}. \tag{2.62}$$

Note that in this thesis, we mainly deal with spatially homogeneous vector fields, such that Eq. (2.62) holds[(9)]. One can check that this eliminates the vector potential from the Hamiltonian by calculating

$$\exp\left(-\mathrm{i}\Lambda(\boldsymbol{r})\right)\left(\boldsymbol{p} + e\boldsymbol{A} - \boldsymbol{\nabla}\Lambda(\boldsymbol{r})\right)^2 \exp\left(\mathrm{i}\Lambda(\boldsymbol{r})\right)|\Psi\rangle = \left(\boldsymbol{p} + e\boldsymbol{A}\right)^2 |\Psi\rangle \tag{2.63}$$

with $\boldsymbol{p} = -i\boldsymbol{\nabla}$.

The transformation of Eq. (2.61b) changes the Wannier functions to

$$\tilde{w}(\boldsymbol{r} - \boldsymbol{R}, t) = \exp\left(\mathrm{i}\Lambda(\boldsymbol{r} - \boldsymbol{R})\right) w(\boldsymbol{r} - \boldsymbol{R}) \tag{2.64}$$

and thus the Bloch functions become (doing the inverse construction of Eq. (2.21))

$$\tilde{\Psi}_{\boldsymbol{k}}(\boldsymbol{r}, t) = \frac{1}{\sqrt{N}} \sum_{\boldsymbol{R}} \exp\left(\mathrm{i}\boldsymbol{k} \cdot \boldsymbol{R}\right) \tilde{w}(\boldsymbol{r} - \boldsymbol{R}, t). \tag{2.65}$$

The Wannier functions in Eq. (2.64) enter into the calculation of the hopping terms (compare Eq. (2.24))

$$\begin{aligned} \tilde{J} &= \int \mathrm{d}^2 r \; \tilde{w}^*(\boldsymbol{r} - \boldsymbol{R}) V(\boldsymbol{r} - \boldsymbol{R}) \; \tilde{w}(\boldsymbol{r}) \\ &= \int \mathrm{d}^2 r \; \Big[\exp\left(-\mathrm{i}\; e\boldsymbol{A}(t) \cdot (\boldsymbol{r} - \boldsymbol{R})\right) w^*(\boldsymbol{r} - \boldsymbol{R}) V(\boldsymbol{r} - \boldsymbol{R}) \\ &\qquad w(\boldsymbol{r}) \exp\left(\mathrm{i}\; e\boldsymbol{A}(t) \cdot \boldsymbol{r}\right) \Big] \end{aligned} \tag{2.66}$$

with a spatially independent vector field $\boldsymbol{A}$, and it follows that the hopping amplitude

(9) Some authors state that the Peierls substitution leads to wrong results in the presence of a strong magnetic field, as it neglects changes to the energy and to the amplitude of the hopping parameters [113, 114]. Reference [115] provides a rigorous derivation for a Peierls substitution for magnetic Bloch bands.

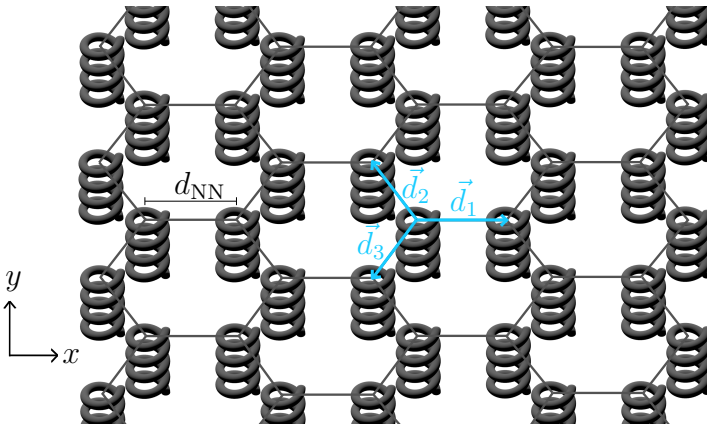

Figure 2.9: Helices arranged on a honeycomb lattice mimic the effect of circularly polarized light irradiated onto graphene. Shown in blue are the distances between nearest neighbors $\boldsymbol{d}_{1,2,3}$ with absolute value d_{NN}.

$J_{m,n}$ between site m and n changes to

$$\tilde{J}_{m,n} = J_{m,n} \exp\left(-\mathrm{i}\ e\boldsymbol{A}(t) \cdot (\boldsymbol{R}_m - \boldsymbol{R}_n)\right). \tag{2.67}$$

In the tight-binding limit $\boldsymbol{R}_m - \boldsymbol{R}_n$ is the vector connecting two nearest-neighbor lattice sites.

Thus, the presence of a non-vanishing vector field adds an additional phase to our hopping (see also [54, 116]).

2.8 Floquet-modulated honeycomb lattice

Using the relations introduced above, we want to go through the example of a Floquet-modulated honeycomb lattice. This model will be important for the results presented in section 6.1 and 6.3 and therefore will be explained in detail here. We will directly do this for our waveguide model, so that from now on we use z instead of the time t.

As explained before, we want to obtain topological edge states without the need of a magnetic field. In graphene, this can be achieved by applying an AC-electric field. Such a field of course has almost no effect on photons in waveguides. Instead, the effect of an AC-field is modeled by bending the waveguide axes helically [3] (see Fig. 2.9). Then, the new coordinates for a waveguide are

$$x' = x + R\cos(\omega z), \tag{2.68a}$$
$$y' = y + R\sin(\omega z), \tag{2.68b}$$
$$z' = z, \tag{2.68c}$$

with $\omega = \frac{2\pi}{Z}$, helix pitch Z and helix radius R.

We can do a global coordinate transformation to the co-rotating system by inserting the new derivatives

$$\partial_x = \partial_{x'}, \tag{2.69a}$$

$$\partial_y = \partial_{y'}, \tag{2.69b}$$

$$\partial_z = \frac{\partial x'}{\partial z}\partial_{x'} + \frac{\partial y'}{\partial z}\partial_{y'} + \partial_{z'} = -R\omega \begin{pmatrix} \sin(\omega z') \\ -\cos(\omega z') \end{pmatrix} \cdot \vec{\nabla}'_\perp + \partial_{z'} \tag{2.69c}$$

into the Schrödinger equation

$$\mathrm{i}\partial_z \Psi = -\frac{1}{2k_0}\nabla_\perp^2 \Psi - V(x,y)\Psi. \tag{2.70}$$

Thus, the Schrödinger equation in the new coordinates becomes

$$\mathrm{i}\partial_{z'}\Psi' = -\frac{1}{2k_0}\nabla_\perp'^2 \Psi' + V(x',y')\Psi' + \mathrm{i}R\omega \begin{pmatrix} \sin(\omega z') \\ -\cos(\omega z') \end{pmatrix} \cdot \vec{\nabla}'_\perp \Psi'. \tag{2.71}$$

If we define the vector potential as

$$\boldsymbol{A} = A_0 \begin{pmatrix} \sin(\omega z') \\ -\cos(\omega z') \end{pmatrix} \qquad \text{with} \qquad A_0 = -k_0 R\omega \tag{2.72}$$

we can rewrite Eq. (2.71) into

$$\mathrm{i}\partial_{z'}\Psi' = -\frac{1}{2k_0}\left(\boldsymbol{\nabla}'_\perp + \mathrm{i}\boldsymbol{A}(z')\right)^2 \Psi' + V(x',y')\Psi' - \frac{k_0}{2}R^2\omega^2\Psi'. \tag{2.73}$$

The last term gives an offset to the energy that is the same for all wave vector components. Thus, it can be neglected if we only look at the band structure for a lattice where all helices have the same parameters.

The vector potential $\boldsymbol{A}$ is connected to an AC-electric field

$$\boldsymbol{E} = -\frac{\partial \boldsymbol{A}}{\partial z'} = k_0 R\,\omega^2 \begin{pmatrix} \cos(\omega z') \\ \sin(\omega z') \end{pmatrix}, \tag{2.74}$$

with constant amplitude $k_0 R\,\omega^2$ and circular polarization.

Now that Eq. (2.73) equals Eq. (2.60), we can use Peierls substitution (see section 2.7). Note that $\boldsymbol{A}$ is not depending on spatial coordinates, such that the curl of it vanishes.

Peierls substitution with the nearest-neighbor distances

$$\boldsymbol{d_1} = d_{\mathrm{NN}} \begin{pmatrix} 1 \\ 0 \end{pmatrix}, \quad \boldsymbol{d_2} = \frac{d_{\mathrm{NN}}}{2} \begin{pmatrix} -1 \\ \sqrt{3} \end{pmatrix}, \quad \boldsymbol{d_3} = -\frac{d_{\mathrm{NN}}}{2} \begin{pmatrix} 1 \\ \sqrt{3} \end{pmatrix} \tag{2.75}$$

leads to

$$\tilde{J}_1 = J_1 \exp\left(-\mathrm{i}A_0 d_{\mathrm{NN}} \sin(\omega z)\right), \tag{2.76a}$$

$$\tilde{J}_2 = J_2 \exp\left(-\mathrm{i}A_0 d_{\mathrm{NN}}/2 \left(-\sin(\omega z) - \sqrt{3}\cos(\omega z)\right)\right), \tag{2.76b}$$

$$\tilde{J}_3 = J_3 \exp\left(-\mathrm{i}A_0 d_{\mathrm{NN}}/2 \left(-\sin(\omega z) + \sqrt{3}\cos(\omega z)\right)\right), \tag{2.76c}$$

and thus

$$\tilde{J}_{l+1} = J_{l+1} \exp\left(-\mathrm{i}A_0 d_{\mathrm{NN}} \sin\left(\omega z - \frac{2\pi}{3} l\right)\right) \tag{2.77}$$

with $l = 0,1,2$.

We can use the Jacobi-Anger expansion

$$\exp\left(\mathrm{i}A\sin(\theta)\right) = \sum_{n=-\infty}^{\infty} \mathscr{J}_n(A) \exp\left(\mathrm{i}n\theta\right) \tag{2.78}$$

to re-write the hoppings. Here, $\mathscr{J}_n$ is the n^{th} Bessel function of the first kind. With this, and $J := J_1 = J_2 = J_3$ we obtain the coefficients of Eq. (2.59)

$$J_{i,j}^{(m-n)} = J\,\mathscr{J}_{m-n}(-A_0 d_{\mathrm{NN}}) \exp\left(-\mathrm{i}\frac{2\pi}{3} l(m-n)\right). \tag{2.79}$$

Calculating H_{eff} by Brillouin-Wigner theory [110] yields

$$H_{\mathrm{BW}} = \sum_{i,j}^{\mathrm{NN}} J_{\mathrm{eff}} a_i^\dagger a_j + \sum_{i,j}^{\mathrm{NNN}} \mathrm{i}\tau_{i,j} K_{\mathrm{eff}} a_i^\dagger a_j + \sum_{i,j}^{\mathrm{L-path}} L_{\mathrm{eff}} a_i^\dagger a_j + \sum_{i,j}^{\mathrm{M-path}} M_{\mathrm{eff}} a_i^\dagger a_j + J\mathcal{O}\left(\frac{J^3}{\omega^3}\right). \tag{2.80}$$

With $\tau_{i,j} = \pm 1$ the chirality of the next-nearest neighbor hopping ('+' for clock-wise, '-' for anti-clockwise hopping) is included. H_{BW} has four components (for their exact calculation see [110]): J_{eff} is the nearest neighbor hopping term. It is real and mainly includes the time-averaged hopping. This means that the Bessel function that it contains re-scales the total bandwidth of the band structure, depending on the amplitude of the driving A_0. The next-nearest neighbor hopping $\mathrm{i}\tau_{i,j}K_{\mathrm{eff}}$ is imaginary, as in the Haldane model, and leads to non-trivial topology in the first place. The sign of K_{eff}

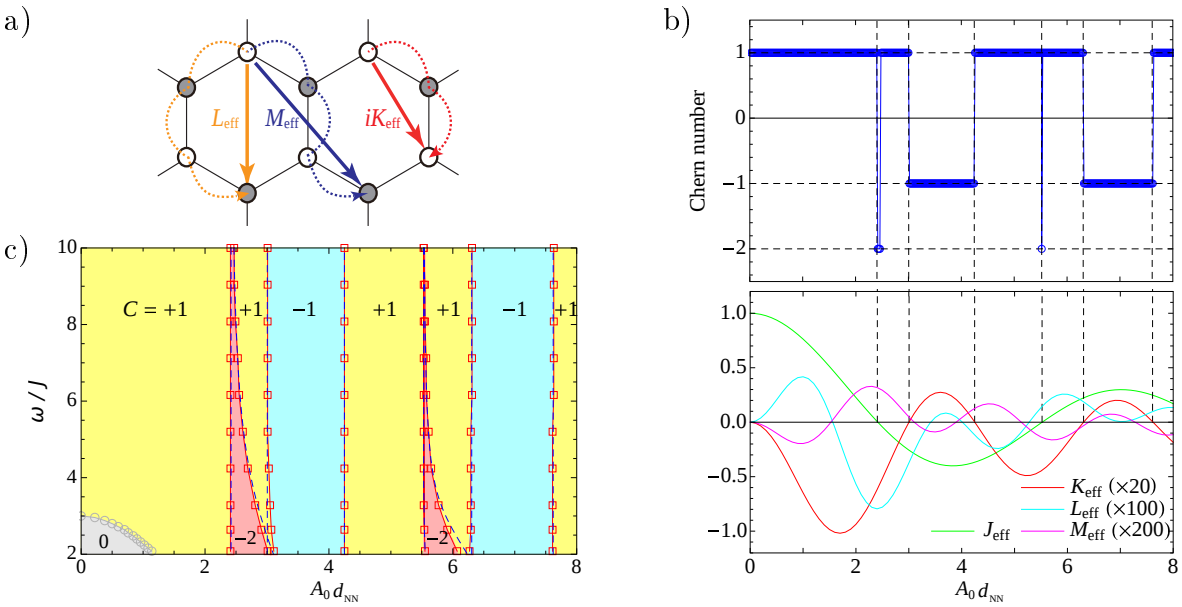

Figure 2.10: a) Sketch of the next-nearest hopping iK_{eff} and the third-neighbor hoppings M_{eff} and L_{eff}. b) The Chern number (obtained via summation over all bands below $E = 0$) in dependence on the amplitude of the driving A_0. The lower plot shows the influence of the respective hoppings. Note that the next-nearest and third-neighbor hoppings are scaled. c) Topological phase diagram showing the Chern number in dependence on $A_0 d_{\text{NN}}$ and ω/J. In the grey region, different Floquet replicas start to overlap and the effective Hamiltonian is no longer valid. All images taken from [110], with variable names adapted to fit the text.

equals the Chern number of the system, except when J_{eff} is close to zero. In the BW theory K_{eff} also includes multi-photon absorption/emission processes from/to higher Floquet orders. It scales with $1/\omega$ in the frequency. There are two additional terms M_{eff} and L_{eff} that represent third-neighbor hoppings (see Fig. 2.10 a)). Those are also real and scale with $1/\omega^2$. They induce additional gap openings near $J_{\text{eff}} \approx 0$ by connecting the a and b sublattices, and lead to a Chern number of -2. The effects of the corresponding terms are represented in Fig. 2.10 b). A phase diagramm with the Chern numbers C in dependence on the driving amplitude A_0 and frequency ω is shown in Fig. 2.10 c).

For small frequencies ω the effective Hamiltonian is no longer valid, as different Floquet replicas ('photon sectors') start to overlap. There, numerically, a very rich topological phase diagram with high absolute values of the Chern numbers was found in [110].

To see the chiral edge states that arise from the non-trivial topology of the system, we have to look at a (semi-)finite system. Then, only the k-component in the infinite direction is well defined, which means that we transform only this component in Eq. (2.39). Thus, we get a projected band structure that shows edge states in the finite direction (see Fig. 2.11). Most of the time when we show projected band structures in this thesis, they are obtained using Eq. (2.55), where we calculate $U(T,0)$ by numerically solving

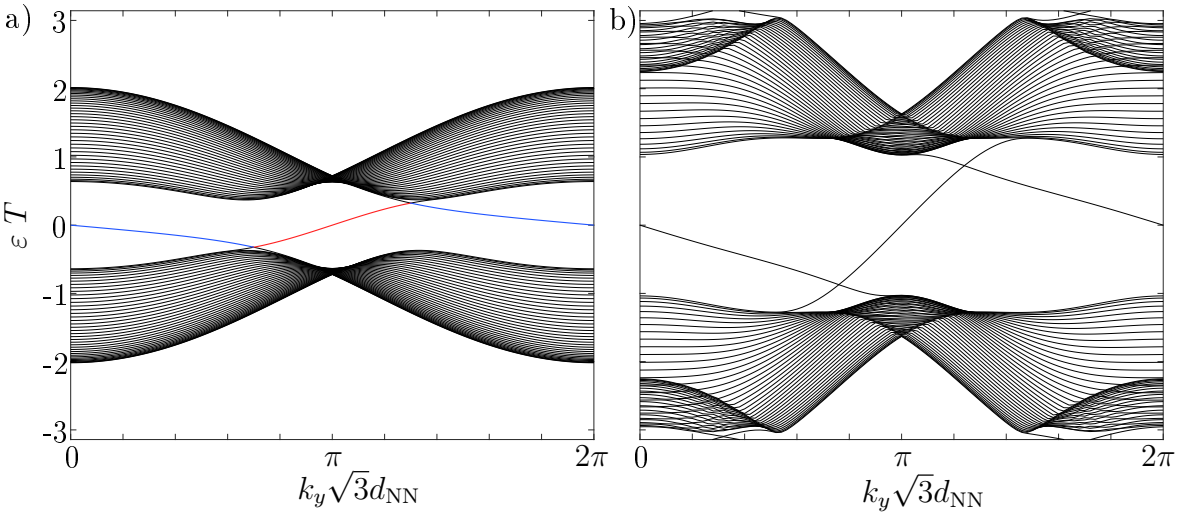

Figure 2.11: Projected quasi band structures of the honeycomb lattice with one zigzag edge on the left side of the array (red band) and one bearded edge on the right side (blue band). The quasi-energies ε were calculated by using Eq. (2.55) and numerically solving Eq. (2.52). a) $A_0 d_{\mathrm{NN}} = 1.3$ and $\omega = 6J$, b) $A_0 d_{\mathrm{NN}} = 1.3$ and $\omega = 3J$. In b) different Floquet replicas already start to overlap, such that band gaps open at the edges of the Floquet Brillouin zone at $\varepsilon\, T = \pm\pi$.

Eq. (2.52) with the time-dependent tight-binding Hamiltonian.

As we see in Fig. 2.11 the edge states of the bearded and zigzag edges (compare Fig. 2.6) live in different sections of the k-space. Armchair edges are not present here, as the lattice is infinite in this direction. In the presented band structure we have used a system with one zigzag edge on the left side and one bearded edge on the right side. We can see that the slopes for these two different edge modes have opposite sign. The slope of the energy dispersion corresponds to the edge state's group velocity. Opposite sign thus means, that the edge state travels upwards (in the positive y-direction) on the left edge and downwards (negative y-direction) on the right edge, i.e., it moves around the edges of the structure clockwise.

These unidirectional edge states will be of interest in chapters 5 and 6. But before we come to that, we need to introduce the experimental methods in the next chapter.

3 Methods

In the previous chapter we introduced arrays of evanescently coupled waveguides as lattice model systems. The methods used to fabricate these coupled waveguide arrays are explained in the following section. To conduct the experiments on the fabricated structure, a measurement setup was built. A description of its basic setup is given in section 3.2. Furthermore, the principles of the beam propagation method, on which the optical numerical calculations rely, are explained in section 3.3.

3.1 Sample fabrication

For the fabrication of the waveguide arrays multiple steps are necessary. Figure 3.1 shows the work-flow of the sample fabrication. First, the inverse structure is fabricated via 3D lithography (direct laser writing, see sections 3.1.1 and 3.1.2) onto a pretreated substrate. The sample is then developed for approximately 45 min in PGMEA (propylene glycol methyl ether acetate) and subsequently for 15 min in isopropyl alcohol. After letting it dry, its parameters are characterized using a scanning electron microscope (SEM). In the last step it is infiltrated by a second photoresist (see section 3.1.4). Baking it to solidify the liquid photoresist results in the ready-to-use sample.

3.1.1 Direct laser writing

Direct laser writing (DLW), also known as 3D lithography, is a method to fabricate three-dimensional structures on the micrometer scale [60–62, 64, 117–121]. In contrast to conventional 2D or 2.5D lithography, no masks have to be used. Direct laser writing makes use of two-photon absorption. As this is a non-linear process, it will predominantly take place in a small volume of the laser focus where the intensity is high enough to start polymerization. The resulting polymerized volume is roughly of the size of the laser focus and is called voxel, short for volume pixel. Thus, almost arbitrary three-dimensional structures can be built out of multiple voxels by moving the laser focus with respect to the resist.

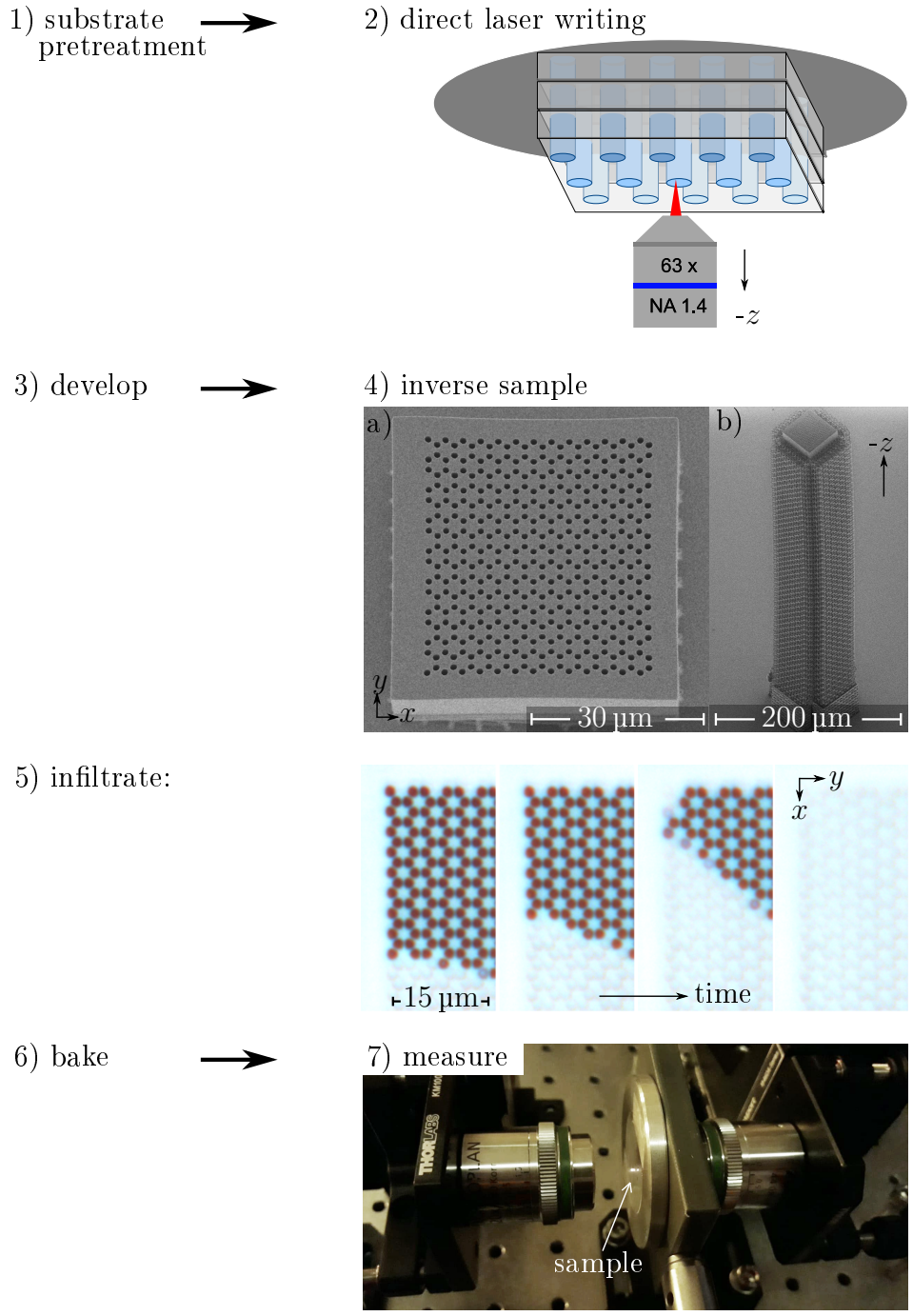

Figure 3.1: The work-flow of the sample fabrication typically consists of seven steps: 1) Pretreatment of substrates, 2) fabrication of the inverse structure by direct laser writing. After development (3), this results in the inverse waveguide sample with empty channels (4). 5) Infiltration of the sample with another photoresist. The unfilled waveguides (dark) are infiltrated with the photoresist *SU8* by capillary forces. After baking the sample (6) to solidify the resist, the sample can be used for measurements. 4a) and b): Scanning electron microscopy images of inverse waveguide samples: a) top view of a honeycomb lattice, b) view tilted by 42° (structure with supporting framework). 5) Microscope images taken during the infiltration process at intervals of a few seconds. 7) Photo of the sample in the measurement setup. 4 a), b) and 5) adapted from [57], licensed under [38].

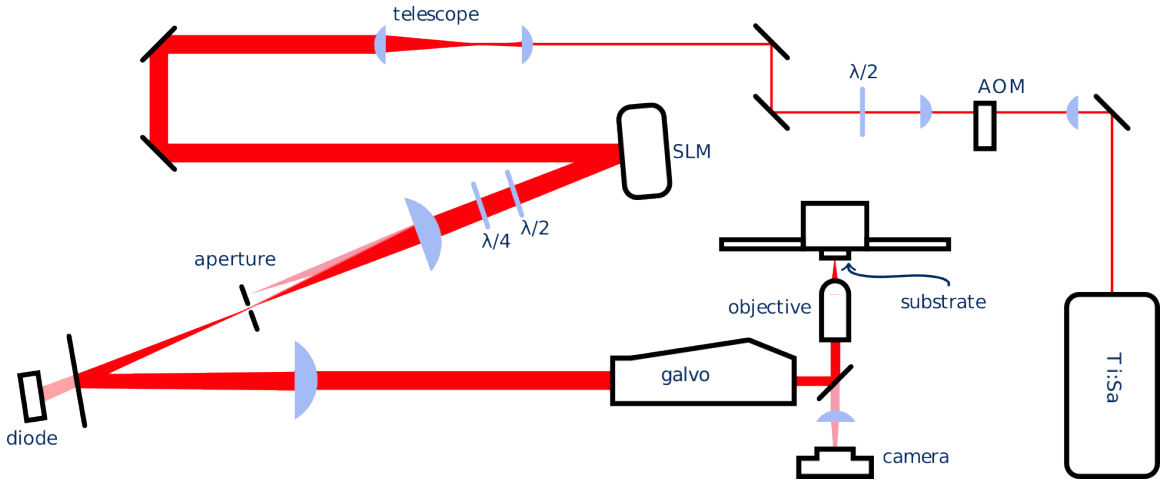

Figure 3.2: Sketch of the DLW setup. Adapted from [120] to include optical elements that were added after the publication of the reference.

The liquid *IP* photoresists used in this thesis consist of at least one monomer and a photoinitiator. The photoresist is transparent for the used near infrared light. The chemical process is the following (for more details see [120]): By two-photon absorption the photoinitiator decomposes into radicals. These radicals start a chain reaction, linking the acrylate groups of the monomers, thus forming a polymer network. The reaction terminates when the radicalized chain combines with another radical or oxygen. Below a certain threshold of the intensity, the polymerization reaction is not started[(1)]. The amount of cross-linking, among other things, depends on the number of radicals created by two-photon absorption. This number is dependent on the dose of laser power deposited into the material, i.e., on the writing speed and laser power and also on the point-spread function of the laser focus, which can be shaped by aberration compensation.

The setup used to fabricate the structures in our lab is described in the following (Fig. 3.2): We start with light from a femto-second pulsed titanium-sapphire laser (Ti:Sa) at a wavelength of 780 nm. fs-pulses are necessary to achieve high peak intensities, that guarantee large cross-sections for two-photon absorption, and to minimize thermal input into the resist. The laser beam is focused onto an acousto-optic modulator (AOM). The AOM generates an optical lattice for the laser beam using ultrasonic waves. The intensity of the light diffracted into the first diffraction order is dependent on the voltage applied to the AOM. By selecting this order using apertures, the laser power in the focus can be controlled via the software. After the AOM, the beam is collimated again by another lens. A $\lambda/2$ plate rotates the polarization axis, as the following spatial light modulator (SLM) needs a certain direction of linear polarization for optimal phase modulation.
After the $\lambda/2$ plate the beam is expanded by a telescope and sent onto the SLM for

(1) This is due to both fast combinations of few created radicals with other molecules (as mentioned above), and energy transfer from the photoinitiator to other molecules.

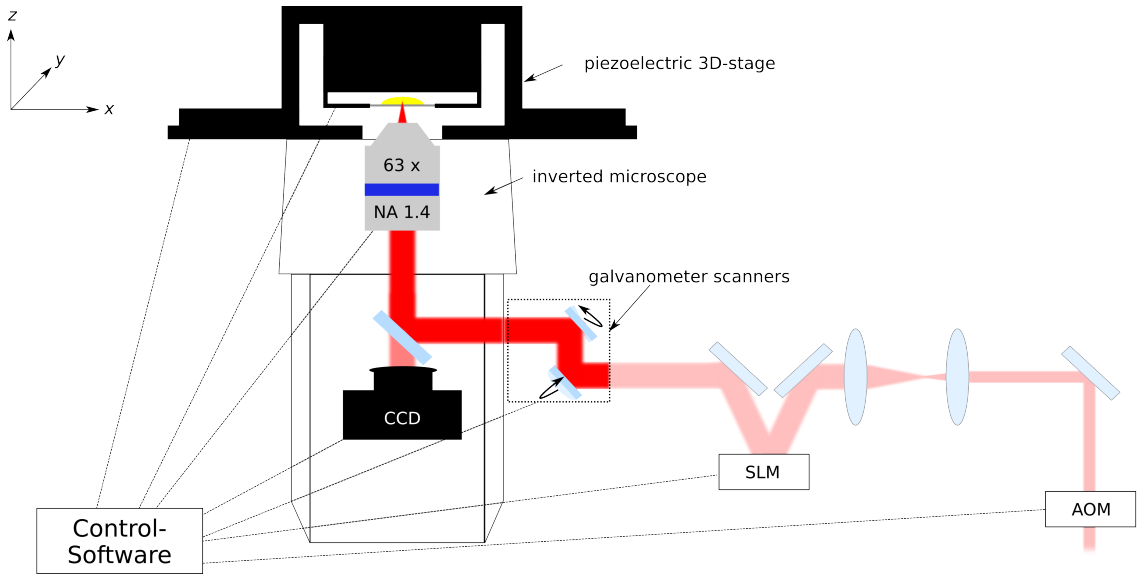

Figure 3.3: Setup used for direct laser writing. Shown are the parts incorporated into the inverted microscope, as an addition to Fig. 3.2.

aberration compensation. The SLM is a phase-only reflective SLM using liquid crystals on silicon. These crystals can be rotated pixel-wise by applying electric fields. Thus, a pixel-wise phase-shift can be 'imprinted' onto a beam reflected from the SLM. References [120–123] developed a method to generate a hologram for the SLM, that shapes the laser focus used for DLW and thus applies a compensation for the aberrations induced in the focus due to the optical setup. An additional blazed grating on the hologram shifts the reflected pattern into the 1st diffraction order, which allows to block unmodulated light. All diffraction orders except for the 1st one are blocked by an aperture in front of the galvanometer scanners.

Almost perfect circular polarization is crucial to achieve a circular cross-section of the voxel in the x-y-plane. The better circular the polarization, the larger the cross-section of two-photon absorption [124]. This is achieved by the combination of a $\lambda/2$ and $\lambda/4$ plate after the SLM[(2)]. Two lenses in 4f-configuration then image the beam onto the galvanometer scanner, which consists of two fast rotating mirrors that tilt the beam and thus lead to translation of the laser focus in the focal plane. The resulting translation is restricted due to vignetting at the objective [125], that is used to focus the beam into the resist. We used a 63x *Leica* objective (HC PL APO, number 11506349), with a numerical aperture (NA) of 1.4, resulting in a field size of about 200 µm × 200 µm in the x-y-plane. The writing process is imaged via a beam-splitter onto a camera (*Zeiss AxioCam MRm*, see Fig. 3.3), using light from a red-filtered halogen lamp. As the refractive index of the resist changes at polymerization, the structure that is built can be seen. Also, one can see the moving laser focus due to the fluorescence of the used

(2) The galvanometer scanner slightly changes the polarization, as the light is impinging in a small angle. By using a $\lambda/2$ and a $\lambda/4$ plate before the scanner, we polarize the light elliptically, such that it will be circularly polarized in the focus of the objective.

IP-resists. Galvanometer scanners, objective, camera and stage including the sample holder are attached to an inverted microscope (*Zeiss Axio Observer.Z1*; see Fig. 3.3). The writing process is managed by the software *NanoWrite*. It controls the AOM, SLM, the positioning of the sample relative to the laser focus and the synchronization of all components.

To prepare the sample fabrication, a pretreated (for details see [60] and section 3.1.3) glass substrate is fixed onto a holder and inserted into the microscope stage. During the writing process, the sample position can be moved relative to the laser focus via three different mechanisms (see [120] for details): First, by mechanically moving the stage in the x- and y-direction, with a positioning accuracy of 3 µm [126]. It is a slow method and more inaccurate than the other methods, but the only one usable to cover larger distances. The second way is to move the sample holder via piezo-electric elements [127] in the x-, y-, or z-direction. The movement range is here limited to 300 µm in each direction, but has a high positioning accuracy in the range of 10 nm [125]. Also, it is rather slow, as usable scan speeds do not exceed 300 µm/s [125]. The third way is to move the laser focus via galvanometer scanners in x and y, thus building the structure layer by layer. This results in lower but sufficient accuracy compared to the piezos. The *Nanoscribe* User Manual [125] states the minimal step size to be approximately 14 nm when working with a 63x objective. Using the galvanometer scanners is the fastest way, with scan speeds up to 20 000 µm/s (in combination with the 63x objective), but, as explained before, results in a limited field of view due to vignetting, which is about 200 µm × 200 µm in our setup. In the z-direction, one can also move the objective by using the microscope z-drive (step size of 10 nm according to [128]).

To cover larger areas, 'stitching' (see also [125]) is necessary: This means using the galvanometer scanners to write one segment and than moving the stage to write the second segment next to it. However, this results in errors due to the limited accuracy in the stage positioning. Also, ridges between different segments form, as the laser beam is deflected by already polymerized blocks. Therefore, this method was not used for the fabrication of our samples.

The dose that is deposited into the resist roughly depends on the square of the laser power divided by the scan speed of the laser focus [125]. For the effect of the laser power on the sample quality see Fig. 3.4. The amount of cross-linking, however, also depends on the point-spread function of the laser focus and complex polymerization chemistry. For example, the proximity effect is accountable for a larger effective dose on the interior of a structure than on its edges. It also leads to clogging of empty (i.e. intentionally unpolymerized) channels due to photon scattering, radical diffusion etc. (see Fig. 3.4 c)). I have also experienced that the fabrication of single waveguides proved to be more difficult than to fabricate arrays of closely spaced waveguides, due to clogging caused by the proximity effect.

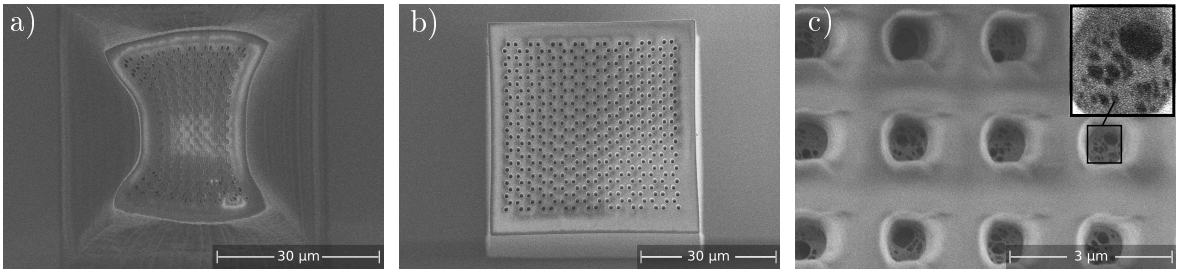

Figure 3.4: SEM images of inverse structures, fabricated by DLW using different laser power at a fixed scan speed: a) if the laser power is too low, the structure is strongly deformed; b) at intermediate laser power we achieve good quality of the sample; c) a laser power that is too high results in clogging of the channels. Taken from [60].

3.1.2 Requirements of the waveguide samples and specifics of the fabrication

The fabrication method of the waveguide samples was chosen to fulfill several criteria:
- We want to use single-mode waveguides, as we only consider band structures for the fundamental mode (see also chapter 2). To achieve single-mode waveguides, the waveguide diameter should be small.
- Uniform and isotropic coupling between the waveguides is assumed in all calculations and should thus be implemented in the samples.
- The temporal dynamics of our model system scales with the number of 'hops' per sample length. In the measurements, we want to capture the wave function after a certain time, e.g., to see that the edge mode has moved along the edge of the sample. Therefore, we need both large coupling and long samples in z.

In the following, we will explain how to meet these requirements.

Waveguides with a circular cross-section are needed to ensure uniform coupling between neighboring waveguides. However, the laser focus used in the direct laser writing is elongated along z. Therefore, waveguides are fabricated such that their propagation axis lies along z. Thus, the elongation of the laser focus only has a large impact on the shape of waveguides that are modulated in the z-direction with a very small pitch in the range of a few micrometers. However, we commonly do not use such small modulation ranges.

To see enough of the dynamics during the measurement, the coupling has to be large with respect to the sample length. The coupling constants depend on the refractive index contrast among other things (see sections 2.1 to 2.3). Fabricating the inverse sample and infiltrating it afterwards, allows to choose appropriate materials and to tune the refractive index contrast. This also has the advantage that different materials can be used for infiltration.

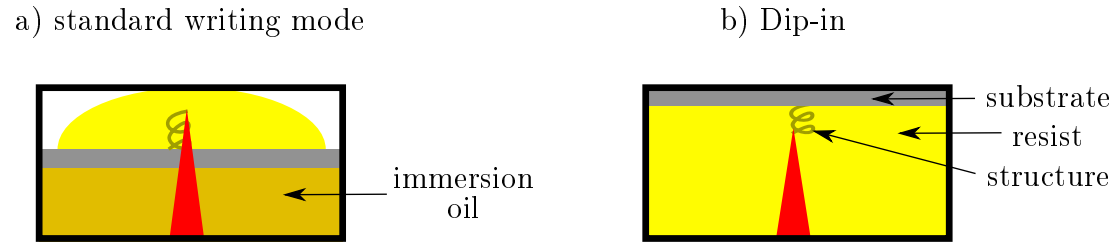

Figure 3.5: a) Standard writing mode using immersion oil between substrate and objective. b) Dip-in lithography, where the resist acts both as photoresist and immersion medium.

The samples need to be large in height ($z > 300\,\mu m$), in order to see enough of the propagation for a given hopping length in the experiment. However, the working distance of the used objective was 310 µm, while the glass cover sheet had a thickness of 170 µm. This leaves only 140 µm of free range for the structure when using the setup in normal configuration, i.e., applying immersion oil onto the objective and resist on top of the glass sheet (see Fig. 3.5). Luckily, two-photon absorption allows to use the setup in Dip-in configuration [129]. This means that the resist is applied directly onto the objective, acting both as photoresist and immersion medium. As polymerization only takes place in the focal spot, the objective is not affected. However, additional aberrations result if the refractive index of the resist does not match that of the objective's lens. This is why *IP-Dip* [125], a negative-tone photoresist developed especially for this purpose by the company *Nanoscribe*, was used. However, the index matching of *IP-Dip* to the lens, and thus also to the glass sheet, has a negative side-effect on the automatic interface finder (*Zeiss Definite Focus* [125, 130]). The interface finder determines the z-position of the interface between the glass cover sheet and the resist, using the reflection of light from the interface. For a small refractive index contrast between resist and sheet, the reflectivity is low, and the detection of the interface does not work properly anymore. Precise positioning, however, is important to make sure that the DLW printed structures are properly attached to the cover sheet. Therefore, either special glass sheets have to be used, or the conventional cover slips (by *Menzel*, Ø30 mm, selected thickness of (170 ± 10) nm) have to be pretreated to create sufficient refractive index contrast (see section 3.1.3). Using the Dip-in configuration and the microscope's z-drive, now the height of the structure is only limited by the size of the drop of resist, and could in principle reach several millimeters[(3)]. To move the laser focus in the x-y-direction the galvanometer scanners were used. As they allow for the highest scan speed, compared to the other methods, the fabrication times were significantly lower. Depending on the structure's specifics and size, about 8 layers per minute with a layer thickness of 250 nm in the z-direction were printed. Usually, the maximum scan speed of 20 000 µm/s and the continuous mode was used. Also, a hatching distance between neighboring lines of 100 nm was chosen. The microscope's z-drive was used to print the samples from the substrate on in the negative z-direction with a slicing distance between the layers of 250 nm. The vignetting at the galvanometer

(3) The limitation by the microscope's z-drive is in the range of 1.2 cm [120].

scanners and objective leads to an inhomogeneous distribution of the laser intensity along the field of view. As the lateral size (x-y-plane) for most of the structures was very large, also care had to be taken to find the lateral area with the most homogeneous dose deposition. Therefore, test structures were printed with different galvanometer offsets.

During development, the samples fabricated with *IP-Dip* tend to shrink. This means that the developed structures only result in approximately 85% of their programmed size in the axial and about 90% in the lateral direction. This has to be considered and precompensated (e.g. in the distance between waveguides) when designing the structure. Post-curing the sample after the first development step with additional photoinitiator and UV light reduces the shrinking by increasing the cross-linking [131]. However, it also proved to increase the clogging of the intended channels, and thus could not be used. The shrinking during development leads to forces on the structure, which can result in deformation of the structure (see Fig. 3.4 a)) or even detachment from the substrate. Therefore, a 20 µm high grid is always direct laser written between substrate and structure. This grid is fabricated with high laser power to maximize its strength. It allows the structure to shrink freely, while deforming the grid slightly. It also lifts the structure from the substrate, which has the additional advantage of helping with the infiltration process later on.
With increasing height of the structures they tend to bend to one side. Therefore, stabilizing frames (walls or grids, see Fig. 3.1 b)) are fabricated, surrounding high structures ($h > 500\,\mu m$). The surrounding frame also needs to either compensate for the shrinking or allow isotropic shrinking of the structures.
The shrinking is due to only partial cross-linking of the resist, which depends on the deposited dose into the resist during the writing process. Therefore, the laser power used for writing is a critical parameter. Too little power results in poor cross-linking, such that the structures deform a lot (see Fig. 3.4 a)). Using too high power clogs the waveguide channels (see Fig. 3.4 c)), which means that infiltration does not work properly (see also [60]). As a compromise, a relative power value approximately 2% above the polymerization threshold was chosen (see appendix A.1 for details). The clogging is also a result of radical diffusion, photon scattering and chain growth. Here, proper aberration compensation of the laser focus helped tremendously to achieve usable samples, as comparison with samples fabricated at a standard *Nanoscribe* without aberration compensation, showed. Nevertheless, the diameter of the waveguides is limited, if clogging should be prevented. To ensure reproducibility, the diameter was chosen to be 1.2 µm in the designed structure (i.e. before shrinking).

3.1.3 Pretreatment of the substrates

In order for the automatic interface finder of the *Nanoscribe* to work, the glass substrates have to be pretreated (see also [60]). First, the substrates are cleaned for 10 min

each in acetone, isopropyl alcohol and deionized water, respectively, using an ultrasonic bath heated to 35°C. Afterwards, the samples are blow-dried using a nitrogen gun. In the next step, the samples are coated with approximately 21 nm of Al_2O_3 by atomic layer deposition. This results in a thin layer of higher index material that increases the reflectivity of the substrate. Thus, it enables the interface finder to localize the interface between *IP-Dip* resist and substrate. In the last step, an adhesion promoter [132] is applied to the substrates: First, the surfaces are cleaned and activated by a plasma ashing treatment with oxygen for 10 min. Subsequently, the substrates are put into a solution of 150 ml toluene and 50 µl 3-Methacryloxypropyltrimethoxysilane, for 1 hour, rinsed well with deionized water for 10 min and then blow-dried with a nitrogen gun.

3.1.4 Infiltration

After the DLW printing of the inverse waveguide sample and its development, the sample is infiltrated with the second photoresist. Where not noted otherwise in this thesis, the photoresist *SU8-2* was used for that. A drop of the photoresist is put onto the substrate well away from the structure. The drop is then pushed by the use of a fine tip (patch clamp, with a tip radius between 15 µm and 50 µm) towards the structure. The shrinking grid allows the photoresist to infiltrate the structure from the bottom, while capillary forces help to fill up the entire empty waveguides to the top (see Fig. 3.1 c)). For high structures this takes some time, which is why the structure is let to rest for a night to allow the photoresist to infiltrate the structure. Some deformations, due to shrinking during and after the development, are fixed automatically by infiltration, as the sample swells again. For *SU8*, the sample is then baked on a hotplate to solidify the material. The temperature is ramped from room temperature to 150°C at 10 K per minute, held at 150°C for three minutes and let cool down to room-temperature at the switched-off hotplate. The resulting refractive index contrast between the surrounding *IP-Dip* ($n_{\mathrm{IP-Dip}} = 1.54$) and the waveguides ($n_{\mathrm{SU8}} = 1.59$) was 0.05. The sample then is ready to be measured.

3.2 Measurement

The details of the measurement setup vary for the different experiments and are given in the respective chapters. The common principle shall be given here (see Fig. 3.6): In general, laser light is focused through objective 1 into the waveguides' input facet. The light propagates along z, while 'hopping' in the transverse direction. At the output facet the transverse intensity distribution in the waveguides is observed, using objective 2 and CMOS camera 1 (*Thorlabs* [133]). To observe the input and output

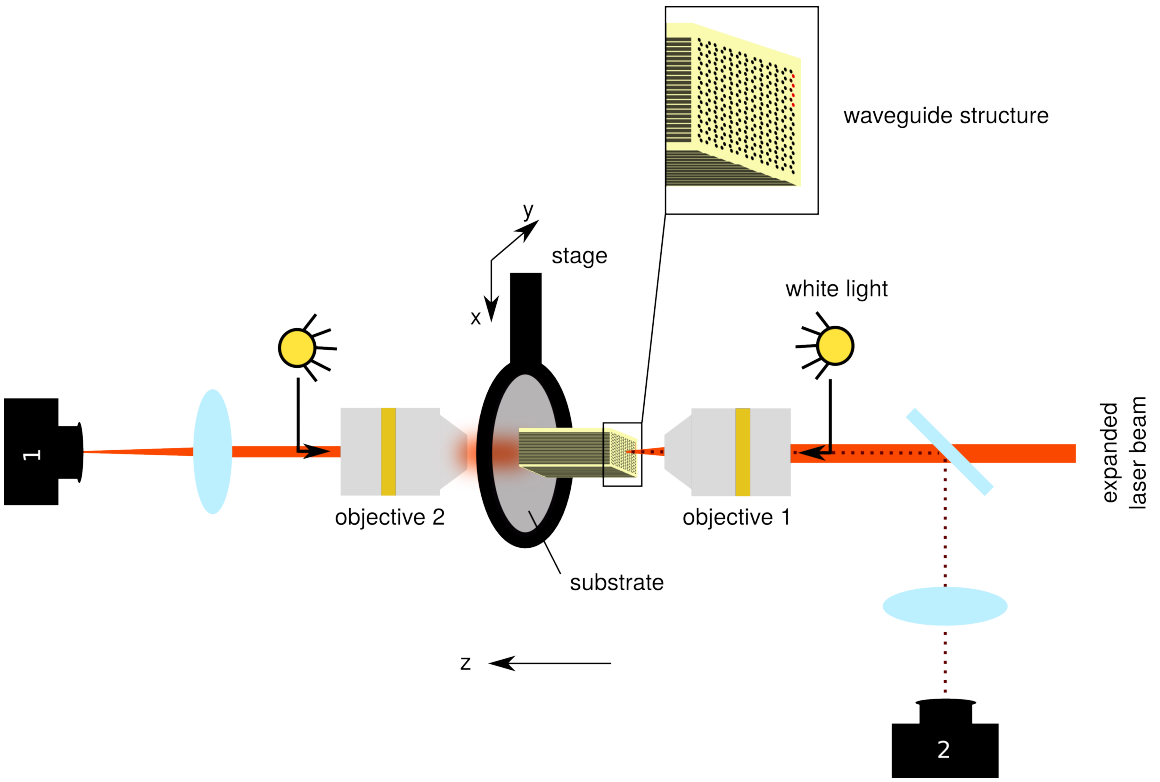

Figure 3.6: Sketch of the measurement setup (size of the sample is exaggerated). For details see main text.

facet of the sample a common light-emitting diode is put into the beam path. Using its white light and a beam-splitter, we can image the facets subsequently for orientation on the sample and easier adjustment. Mounting the sample with the glass substrate pointing towards the output side, the reflection of the input laser focus at the top of the structure (dotted line in Fig. 3.6) can be imaged onto camera 2. This allows to localize the input spot with respect to the waveguide positions. As the sample is mounted on a stage, it can be moved in all three dimensions. Laterally (x-y) this is done by two linear actuators (*Zaber* [134]) with a smallest usable step size of approximately 0.1 µm. In the z-direction a micrometer screw is used. The objectives are also mounted on stages for easier alignment and to adjust the focal plane.

3.3 Beam propagation method

Before doing the respective experiments, numerical calculations were performed to find the best parameters regarding waveguide radius, distances, overall length of sample etc. These were done using the commercially available software OptiBPM by *Optiwave* [135]. OptiBPM can calculate the real-space propagation of light in a given setup of dielectric materials. The software relies on the finite difference beam propagating

method (BPM). BPM works best if there is a main propagation direction of the light (paraxial approximation), which in our case is the propagation direction along the elongated axis of the waveguide, the z-direction. The part of the wavefunction that is oscillating quickly in the z-direction is substituted by a slowly varying term (slowly varying envelope approximation). This is done by using an initial approximation for the effective refractive index. With these approximations the Maxwell equations are solved for a given distribution of refractive indices, while partial derivatives are approximated by finite differences. For more details see [60, 61, 135].

One disadvantage of the software is, that it is mostly designed for planar structures. Wanting to model helical waveguide arrays in 3D, we had to use a trick: Helices in OptiBPM were created by stacking cylinders on top of each other. These cylinders shared the waveguide diameter and had a length of 1.5 µm in the z-direction. Allowing an overlap of 0.5 µm in z between cylinders, their center position was slightly shifted along z to create smooth enough helices. This modeled the fabricated waveguides — that were also built layer by layer — as realistically as possible. As this increased the computational costs, calculations for long structures had to be chopped. For long structures, multiple runs were done using the output field of one run as the input field of the next. Despite these workarounds, OptiBPM mainly gave results agreeing very well with the experimental measurements.

With the necessary theoretical and methodological background now set, we proceed to the results obtained during the thesis in the next chapters.

4 Refraction and reflection by artificial gauge fields

As mentioned in the introduction, we use evanescently coupled waveguides as model systems to mimic electronic effects in solids. These effects in solids often arise from externally applied or internal electric or magnetic fields. As photons do scarcely react to electric or magnetic fields, we need to introduce the concept of artificial gauge fields (AGF), as a way to achieve the same effect on photons as the corresponding field has on electrons. The concept of artificial gauge fields has been widely used in all kinds of model systems [30, 106, 136, 137]. In photonics, AGF were exploited to create effective electric DC and AC fields for dynamic localization [59], to make use of Floquet effects [3], or to mimic magnetic fields [138]. In this chapter of the thesis, we are interested in effects arising from boundaries between two systems with different AGFs.

In this chapter, we start with a very simple way of introducing an interface between two systems with different AGFs, implementing an idea of Moshe-Ishay Cohen [139] and Yaakov Lumer [49] (both Technion, Haifa). Here, an artificial gauge field is created by a linear tilt of a waveguide array along its propagation direction. In itself, this is a trivial gauge field, as we can annihilate its effects by changing the frame of reference to the co-moving frame. In fact, going to the co-moving system is often used to mathematically derive non-trivial fields from more complicated trajectories of the waveguides (see also section 2.8 and [3, 106]). However, the effect of the tilt cannot be gauged away when we combine two of such fields with different directions of the tilt. Then, we can find no coordinate system in which both arrays would be un-tilted. We will see that an interface between two of such regions with trivial fields has a large effect on a wave packet propagating across it. This effect is very interesting, as it can be achieved between two regions with identical material parameters (e.g. (effective) refractive index of the waveguides and the surrounding), by just changing the waveguide trajectories.

In very similar setups, it has been shown that the same principle can be used to create wave-guiding [49] or to model the Rashba pseudo-spin-orbit coupling [48]. Numerically, also propagation effects similar to those in meta-surfaces as, e.g., negative refraction and off-axis focusing have been demonstrated [140]. We contribute a general law for the change of the transverse wave vector components of a wave crossing the interface, and prove its validity in experiments.

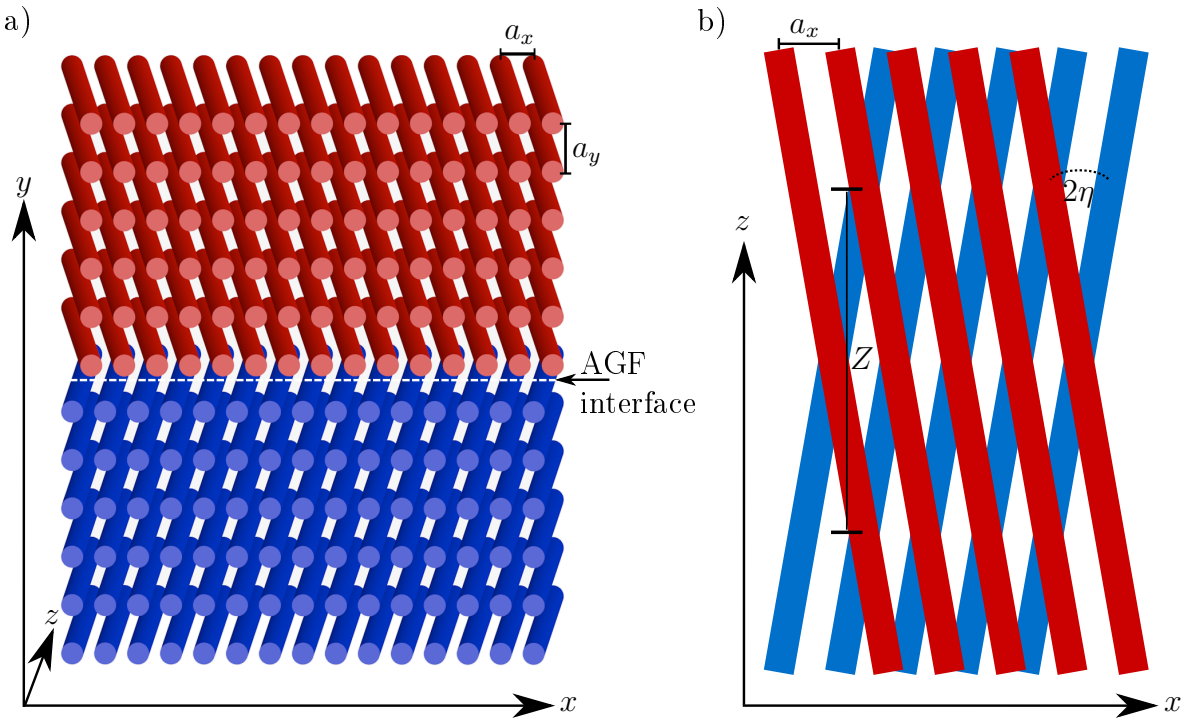

Figure 4.1: Sketch of the setup. Two rectangular arrays of waveguides (red: upper array, blue: lower array) are stacked on top of each other, creating an AGF interface in the y-direction. The waveguide arrays are tilted by 2η with respect to each other. Otherwise, the parameters for the two arrays are identical. The periodicity in the z-direction is given by Z (but is $Z/2$ in the coordinates moving with one of the arrays). a) Front view, b) top view.

We will first start with a description of the system. From the model system, we will derive an analytic formula to describe the effects on a wave packet traveling across the interface between the two AGFs. Then, we will introduce the results obtained by full numerical calculations and the experimental results. The work described in this chapter has been done in collaboration with Moshe-Ishay Cohen, who contributed the theoretical analysis (see also [139]). The publication is in preparation [141].

4.1 Setup and derivation of the analytic formula

The setup consists of two arrays of waveguides, forming two rectangular lattices, with a lattice constant of a_x between two waveguides in the x-direction and a_y in the y-direction. The arrays are stacked on top of each other, with a spacing of a_y between them, creating an AGF interface in the y-direction. Each of the arrays is tilted

linearly with respect to its propagation direction with tilt η, such that

$$x_{\text{upperarray}} = la_x - \eta z \quad \text{for the upper array and} \tag{4.1a}$$

$$x_{\text{lowerarray}} = la_x + \eta z \quad \text{for the lower one,} \tag{4.1b}$$

with $l \in \mathbb{Z}$, i.e., the arrays are rotated against each other by 2η (see Fig. 4.1). Otherwise, the arrays are identical, regarding the waveguide radius r, or their material parameters n_{wg} and n_0 for the refractive index of a waveguide and the surrounding material, respectively.

Due to the periodicity of the lattice in x, the wave vector component along this direction, k_x, is a conserved quantity, as is the propagation constant β . However, the band structure is changed between the lower and the upper array due to the tilt. Therefore, a wave packet crossing the AGF interface between the arrays in the y-direction, experiences a change in the k_y component, dependent on k_x.

To give an analytic formula for the dependency of the change in k_y on k_x, we first calculate the band structure of each of the arrays separately, following [48]. In terms of waveguides, the band structure is given by the propagation constant β_{tilted} in dependence of k_x and k_y. Detailed calculations can be found in the supplemental material of [48].

We start from the slightly reshaped Schrödinger equation of Eq. (2.8)

$$\mathrm{i}\frac{\partial \Psi}{\partial z} = \frac{1}{2k_0}\left(\mathrm{i}\hat{\boldsymbol{e}}_x\partial_x + \mathrm{i}\hat{\boldsymbol{e}}_y\partial_y\right)^2\Psi - k_0\frac{\Delta n(x,y,z)}{n_0}\Psi, \tag{4.2}$$

where we have used $n(x,y,z) = n_0 + \Delta n(x,y,z)$ and neglected $(\Delta n)^2$.
In the upper rectangular lattice of waveguides, tilted by η, the new coordinates are

$$\begin{aligned} x' &= x - \eta z, \\ y' &= y, \\ z' &= z, \end{aligned} \tag{4.3}$$

and the corresponding derivatives are

$$\begin{aligned} \partial_x &= \partial_{x'}, \\ \partial_y &= \partial_{y'}, \\ \partial_z &= -\eta\partial_{x'} + \partial_{z'}. \end{aligned} \tag{4.4}$$

Doing a coordinate transformation with Eq. (4.3) and (4.4), we obtain the Schrödinger

equation in the new coordinates

$$\mathrm{i}\partial_{z'}\Psi' = \frac{1}{2k_0}\left(\mathrm{i}\hat{\boldsymbol{e}}_{x'}\partial_{x'} + \mathrm{i}\hat{\boldsymbol{e}}_{y'}\partial_{y'} + \hat{\boldsymbol{e}}_{x'}k_0\eta\right)^2\Psi' - \left(\frac{k_0}{n_0}\Delta n'(x',y') + \frac{k_0}{2}\eta^2\right)\Psi'. \tag{4.5}$$

With a Bloch-ansatz for the wave function

$$\Psi' = u'(x',y')\exp(\mathrm{i}k_x'x' - \mathrm{i}\beta'z') \quad \text{and} \quad u'(x',y') = u'(x'+a_x,y') \tag{4.6}$$

it follows for the Schrödinger equation (4.5)

$$\beta'u' = \frac{1}{2k_0}\left(\mathrm{i}\hat{\boldsymbol{e}}_{x'}\partial_{x'} + \mathrm{i}\hat{\boldsymbol{e}}_{y'}\partial_{y'} - \hat{\boldsymbol{e}}_{x'}(k_x' - k_0\eta)\right)^2 u' - \left(\frac{k_0}{n_0}\Delta n'(x',y') + \frac{k_0}{2}\eta^2\right)u'. \tag{4.7}$$

Upon comparison with the untransformed version

$$\beta u = \frac{1}{2k_0}\left(\mathrm{i}\hat{\boldsymbol{e}}_x\partial_x + \mathrm{i}\hat{\boldsymbol{e}}_y\partial_y - \hat{\boldsymbol{e}}_x k_x\right)^2 u - \frac{k_0}{n_0}\Delta n(x,y)u \tag{4.8}$$

we see that the wave-vector component k_x is shifted by $k_x = k_x' - k_0\eta$, and that the offset to β now is $\frac{k_0}{n_0}\Delta n = \frac{k_0}{n_0}\Delta n' + \frac{k_0}{2}\eta^2$.

Using tight binding constraints one can calculate the dispersion relation from the Schrödinger equation (see section 2.2). In the case of untilted waveguides on a rectangular lattice this yields the following relation for the propagation constant β:

$$\beta = \beta_0 + 2J_x\cos(k_x a_x) + 2J_y\cos(k_y a_y), \tag{4.9}$$

where β_0 is the propagation constant of a single waveguide and J_x and J_y are the coupling constants in the x- and y-direction, respectively. For a tilted lattice this changes to:

$$\beta_{\text{tilted}} = \beta' + \eta k_x' = \beta_0 + 2J_x\cos((k_x - k_0\eta)a_x) + 2J_y\cos(k_y a_y) - \frac{k_0}{2}\eta^2 + \eta k_x. \tag{4.10}$$

The first equality follows from the fact that

$$\Psi' = u'\exp(\mathrm{i}k_x'x' - \mathrm{i}\beta'z') = u'\exp(\mathrm{i}k_x'(x-\eta z) - \mathrm{i}\beta'z) = u'\exp\left(\mathrm{i}k_x'x - \mathrm{i}(\beta' + k_x'\eta)z\right). \tag{4.11}$$

Eq. (4.10) is only valid inside one tilted array. To calculate, e.g., the Fresnel coefficients at the AGF interface, one has to consider also the coupling between waveguides of the lower and upper array (see supplemental of [48]). However, to obtain the change in the light's k_y component, it is enough to just compare the dispersion relations inside each of the arrays, neglecting any effects happening only locally at the interface.

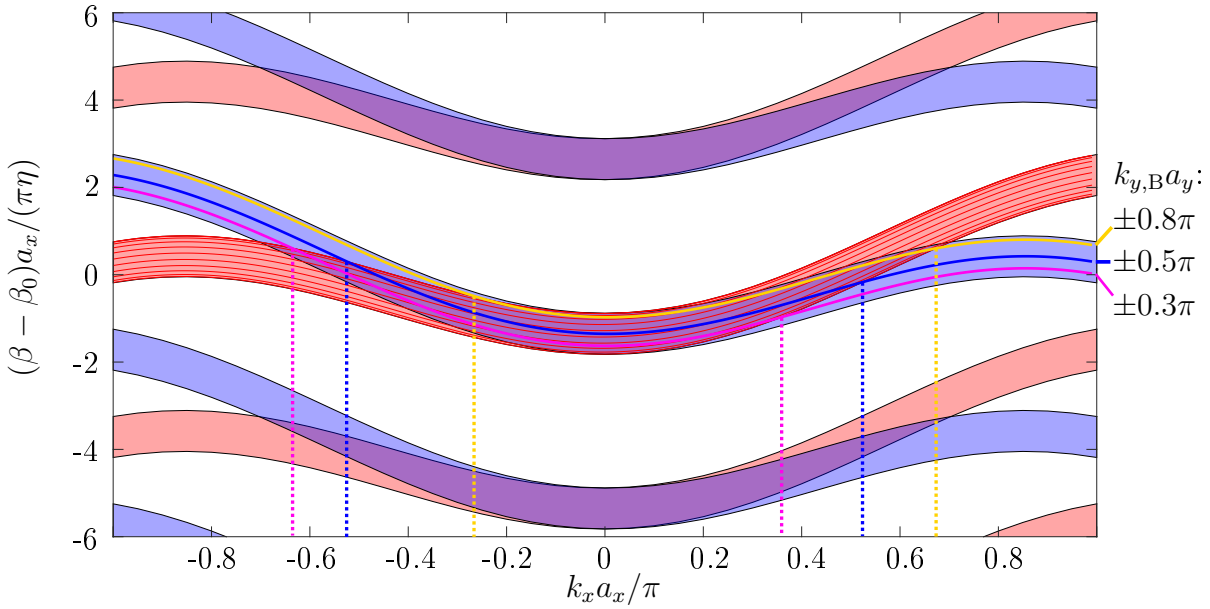

Figure 4.2: Projected dispersion relation for the upper (red, A) and lower (blue, B) array. The solid lines mark different values of $k_y a_y$. In the k_x range where the two bands overlap, refraction takes place for a wave packet traveling across the AGF interface. Outside this range, total reflection occurs. The colored dashed lines mark the k_x-values for the overlap of the bands for the upper and lower array with respect to their corresponding k_y-components in the B array. The repetition of the bands along β is due to the periodicity in z (Floquet effect). Floquet coupling could occur if the red band would intersect with a blue band of next higher or lower β. Parameters are chosen as in the experiment: $r = 0.52\,\mu\mathrm{m}$, $a_x = 1.69\,\mu\mathrm{m}$, $a_y = 2.15\,\mu\mathrm{m}$, $\eta = 0.0093$, $\lambda = 700\,\mathrm{nm}$.

The shift of k_y upon propagation through the AGF interface can now be obtained from the dispersion relation inside a tilted array:

$$\beta_\eta(k_x, k_y) = \beta_0 + 2J_x \cos((k_x - k_0\eta)a_x) + 2J_y \cos(k_y a_y) - \frac{k_0}{2}\eta^2 + \eta k_x - \frac{4\pi\eta}{a_x}m, m \in \mathbb{Z}. \tag{4.12}$$

The last term $(-4\pi\eta m/a_x)$ is a Floquet term that results from the periodicity of the lattice in the z-direction with $Z/2$, where $Z = a_x/\eta$[1]. Due to this, β is only conserved as a 'quasi-energy' and defined up to integer multiples of the frequency $m2\pi/(Z/2)$.

Fig. 4.2 shows the projected band structures of the two tilted arrays onto $k_x a_x$. The red (blue) bands give the dispersion relation for the upper (lower) array. Depicted in three dimensions we would be able to see the sinusoidal shape of the dispersion along $k_x a_x$ as well as along $k_y a_y$. The projection onto one k-component, however, helps us to display the k_y-conversion between the two arrays more easily. In the projected band structure, one band represents the 'energy' values of β for all values of $k_y a_y$. Energies

[1] Remember that in the waveguide model system z corresponds to time and thus β to the energy.

belonging to a certain $k_y a_y$ inside one band are indicated by solid lines in Fig. 4.2. Due to the Floquet term, we see multiple bands with different β for each array.

When a wave packet crosses the AGF interface between the lower array B and the upper array A, the energy is conserved $\beta_\eta(k_{x,\mathrm{A}}, k_{y,\mathrm{A}}) = \beta_{-\eta}(k_{x,\mathrm{B}}, k_{y,\mathrm{B}})$, as well as the wave vector component $k_{x,\mathrm{A}} = k_{x,\mathrm{B}} = k_x$. Graphically, this means that at this β the red and the blue band in Fig. 4.2 overlap. Then, the quasi-energy β of the red band may belong to a different k_y than that of the blue band $k_{y,\mathrm{A}} \neq k_{y,\mathrm{B}}$ (see solid colored lines in Fig. 4.2). Therefore, when the light crosses the AGF interface, $k_{y,\mathrm{A}}$ has to change according to:

$$\cos(k_{y,\mathrm{A}} a_y) - \cos(k_{y,\mathrm{B}} a_y) = \frac{J_x}{J_y}\left[\cos((k_x + k_0\eta)a_x) - \cos((k_x - k_0\eta)a_x)\right] - \eta\frac{k_x}{J_y} - \frac{2\pi\eta}{a_x J_y}\tilde{m}. \tag{4.13}$$

The last term ($-2\pi\eta/(a_x J_y)\tilde{m}$, where again $\tilde{m} \in \mathbb{Z}$) reflects coupling to higher Floquet orders. This could occur, if a red band would intersect with a blue band of next higher or lower order. However, this coupling has not been observed for the parameters used in our experiments, as Fig. 4.2 shows.

We want to obtain an equation for the k_y-component in the upper lattice $k_{y,\mathrm{A}}$, when starting the propagation with a wave packet with $k_{y,\mathrm{B}}$ in the lower lattice. Thus, we rearrange Eq. (4.13) to yield the output component $k_{y,\mathrm{out}} = k_{y,\mathrm{A}}$. We see that we obtain imaginary values of $k_{y,\mathrm{A}}$ for certain k_x. This is the case for large absolute values of k_x where the red and blue band do not intersect in Fig. 4.2. Here, total reflection at the AGF interface occurs. For the analytical curve, we thus set $k_{y,\mathrm{out}} = -k_{y,\mathrm{B}}$ for these values of k_x. Note that this k_x-range is not necessarily mirror symmetric around $k_x a_x = 0$ (see also dashed lines in Fig. 4.2).

We now have obtained an analytic formula to describe the change in k_y that light experiences upon crossing the interface between our two different AGFs. In the following, we want to compare this formula to numerical calculations and probe it in experiments.

4.2 Comparison of the analytic formula to beam propagation calculations

Numerical calculations are performed using the beam propagation method (see section 3.3). These calculations serve two purposes: First, we want to check the validity of the obtained analytic formula, while excluding any fabricational and experimental inaccuracies. Second, they allow for a fast and easy parameter sweep. This helps to

identify the best experimentally obtainable parameters for the sample fabrication, that will show the largest effect of refraction in the experiments. Within the fabricational restrictions we identify the following parameter set: waveguide radius $r = 0.445\,\mu\text{m}$, $a_x = 1.6\,\mu\text{m}$, $a_y = 2.15\,\mu\text{m}$, $\eta = 0.01$, overall propagation distance $h \geq 800\,\mu\text{m}$ and used wavelength $\lambda = 700\,\text{nm}$. These parameters ensure good coupling in the x-, and intermediate coupling in the y-direction, while maximizing, together with a large η, the effect of refraction. At the same time, the distances between waveguides are kept small enough to enable a large number of waveguides to be fabricated within the addressable area, that is limited by vignetting (see section 3.1.1). A large enough number of waveguides is necessary, because the light should not reach the outer edges of the structure during propagation, as this would result in unwanted reflection and scrambling of the k-components.

For the OptiBPM calculations, five neighboring waveguides along the y-direction are illuminated with a Gaussian mode each, at the input facet. In the y-direction a phase difference between the modes is applied, which allows to choose $k_{y,\text{B}}$. The enveloped amplitude of the five modes also follows a Gaussian shape, with full width at half maximum $\sigma = 5a_y$, ensuring a smooth amplitude drop towards the edges of the wave packet. Due to focusing in x into just one column of waveguides, all k_x-values within one Brillouin zone are excited.

The wave packet travels towards the AGF interface with a group velocity $v_{\text{g},y}$ that can be obtained by taking the derivative with respect to $k_y a_y$ from the dispersion relation in Eq. (4.12). As one easily sees, it has a sinusoidal shape, meaning that the wave packet travels the furthest across the AGF interface for $k_{y,\text{B}} a_y = 0.5\,\pi$ for a fixed propagation distance z. For values of $-\pi < k_{y,\text{B}} a_y < 0$ the group velocity is such that the wave packet moves away from the AGF interface in the negative y-direction. Thus, it does not experience refraction nor reflection, except for portions of light that travel across the AGF interface due to dispersion at small group velocities. To yield $k_{y,\text{out}}$ over k_x, the field in the x-y-plane is extracted for certain propagation distances z and 2D-Fourier transformed. The results are plotted in the right column of Fig. 4.3 and 4.4. Comparison of the numerical calculations with the analytical formula (dots) shows a good agreement for the refracted part. The k-distribution obtained by numerics is, as expected, broader than the analytic curve. This is due to the finite width of the inserted $k_{y,\text{B}}$-component. The more waveguides are excited in real-space, the smaller is the width of the k-component in Fourier-space. However, we do not want the input pattern to excite waveguides in the other array across the AGF interface. Also the center position of the input pattern needs to be close enough to the AGF interface, such that the wave packet can travel across the AGF interface in the given propagation distance. Therefore we need to limit the number of excited waveguides. For an excitation of five waveguides the width is $\Delta_{k_y} \approx 0.2\,\pi/a_y$ (see Fig. 4.3 and 4.4). As the same number of illumination spots was chosen in the experiments, the numerical calculation reflects the experimental conditions very well.

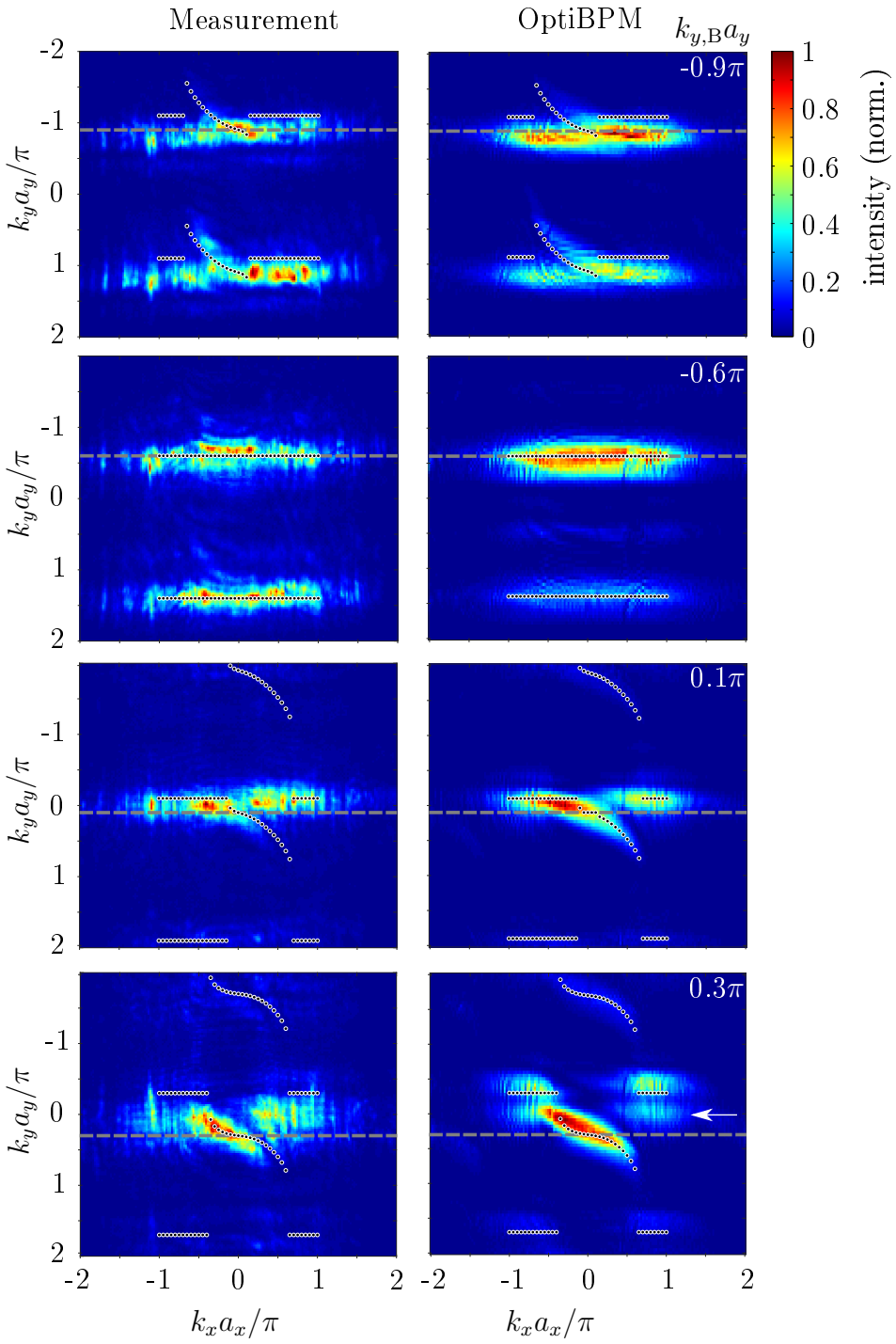

Figure 4.3: Output k-distribution for different input values of $k_{y,\mathrm{B}}$. Left column: measurement. For each image it was averaged over 10 different input positions along k_x. Right column: OptiBPM calculations (without noise). The grey dashed line indicates the value of the input $k_{y,\mathrm{B}}$. The dotted lines represent the analytic values for $k_{y,\mathrm{out}}$, obtained by Eq. (4.13). The white arrow in the lowest right image marks the position of values of $k_{y,\mathrm{out}}$ that neither correspond to reflected, nor refracted light, and whose origin is yet unexplained.

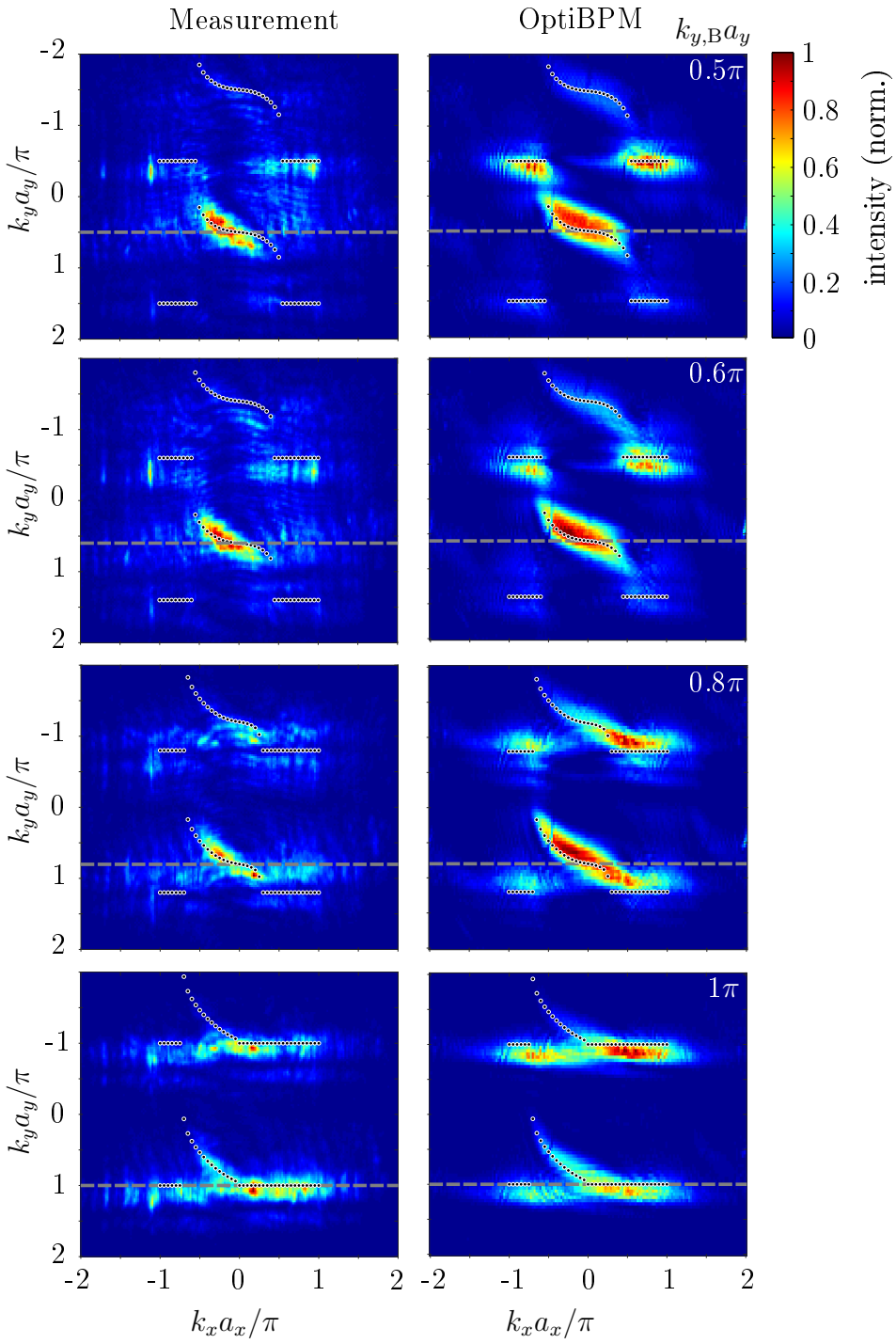

Figure 4.4: Same as Fig. 4.3 for more values of $k_{y,\mathrm{B}}$. The complete measurements can be found in [142].

Both, analytical curve and numerical calculations are now compared to measurements. To do so, a corresponding waveguide sample was fabricated. We used direct laser writing and subsequent infiltration as described in section 3. In the next section, the specifics of the sample fabrication will be addressed briefly.

4.3 Specifics of the sample fabrication

The fabrication of the actual sample proved to be a challenging task because of multiple things: As mentioned before, sufficiently many waveguides were needed. This ensured that in the later experiments the light did not reach the outer edges of the sample for the given propagation length and hopping constants. However, the printable area in the x- and y- direction was restricted due to vignetting. The tilt 2η of the waveguide arrays against one another furthermore enlarged the area to be printed. To keep this area as small as possible, while implementing the maximum number of waveguides, a configuration was chosen in which the two arrays formed an 'X'-shape (when viewed in the x-z-plane, see Fig. 4.1 b)). Thus, the input and output facet were only enlarged by ηh, where h is the total length of the structure in z-direction. Also, care was taken to work in an area where the intensity varied the least, i.e., the vignetting was least pronounced. With these precautions, the number of waveguides fabricated was 64 in the x-direction and 17 (18) in the y-direction for the upper (lower) array.

On the side of the fabrication software, it is favorable to have small data files (gwl-files), speeding up computation[(2)]. Therefore, instead of slicing the whole structure, only two gwl-files — one for the upper and one for the lower array — were used, embedded in a for-loop. Thus, in each z-layer the two (differently tilted) waveguide arrays were shifted in the x-direction by the amount of $2\eta z$ against each other, forming the 'X'-shape (see also Fig. 4.5). However, now the waveguides at the outer edges near the AGF interface between the lower and upper array did not encounter other waveguides, but just solid polymer. This resulted in distortions at the edges due to the different effective dose and radical diffusion, which induced a non-uniform shrinking. Luckily, these distortions canceled during later infiltration with *SU8*, such that they did not pose a problem for the measurements.

At the same time, the propagation distance was needed to be as long as possible, to maximize the number of hops in the y-direction. Thus, long samples were needed, that came along with certain stabilization issues. To stabilize the structure a frame — written with higher power — was built around the structure in each layer. This prevented distortions due to shrinking during development. It also fixed the structure at the sides while allowing it to shrink freely in the middle. Unfortunately, this lead to the formation of a sink in the center, which caused an unwanted lensing effect after

(2) see appendix A.2 on how to further decrease NanoWrite's writing times

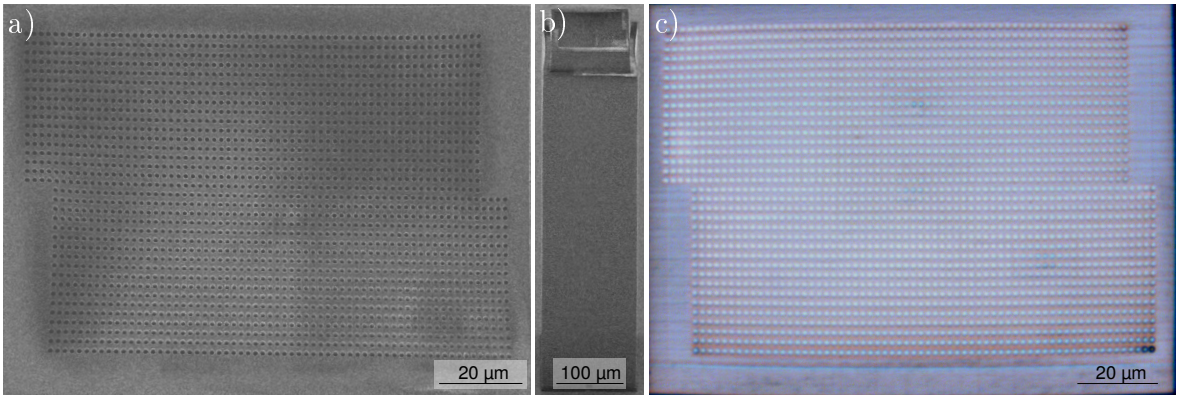

Figure 4.5: a) SEM image of the fabricated inverse waveguide array from the top, b) from the side. c) Microscope image of the infiltrated sample.

infiltration with *SU8*. To prevent this, the last 50 µm in z were fabricated without frame. As mentioned in section 3.1.2, the structure was placed on a 20 µm high grid to raise it from the substrate. This grid allowed the structure to shrink freely and helped with the infiltration later on. SEM images of the inverse sample before infiltration and a microscope image of the infiltrated sample are shown in Fig. 4.5.

Examination with a scanning electron microscope yielded the following parameters for the fabricated inverse waveguide structure:
Radius of waveguides $r = (0.52 \pm 0.07)$ µm, center-to-center distance between waveguides $a_x = (1.69 \pm 0.02)$ µm, $a_y = (2.15 \pm 0.02)$ µm, tilt $\eta = 0.0093 \pm 0.0004$, and maximum propagation length corresponding to the height of the sample $h = (725 \pm 3)$ µm.

The fabricated sample was then placed in the measurement setup, described in the following.

4.4 Experiment

4.4.1 Measurement setup

To conduct the experiments, we needed to excite a specific k_y-distribution in the waveguides. For this, the use of a spatial light modulator (SLM) was necessary. Therefore the measurement setup differed from the one sketched in section 3.2 in some aspects that will be described briefly in the following section.

A schematic drawing of the measurement setup is shown in Fig. 4.6. Light with a wavelength of $\lambda = 700$ nm from a tunable laser (*NKT photonics* [143]) is polarized linearly, expanded by a telescope and sent onto an SLM (*Hamamatsu*). The pattern

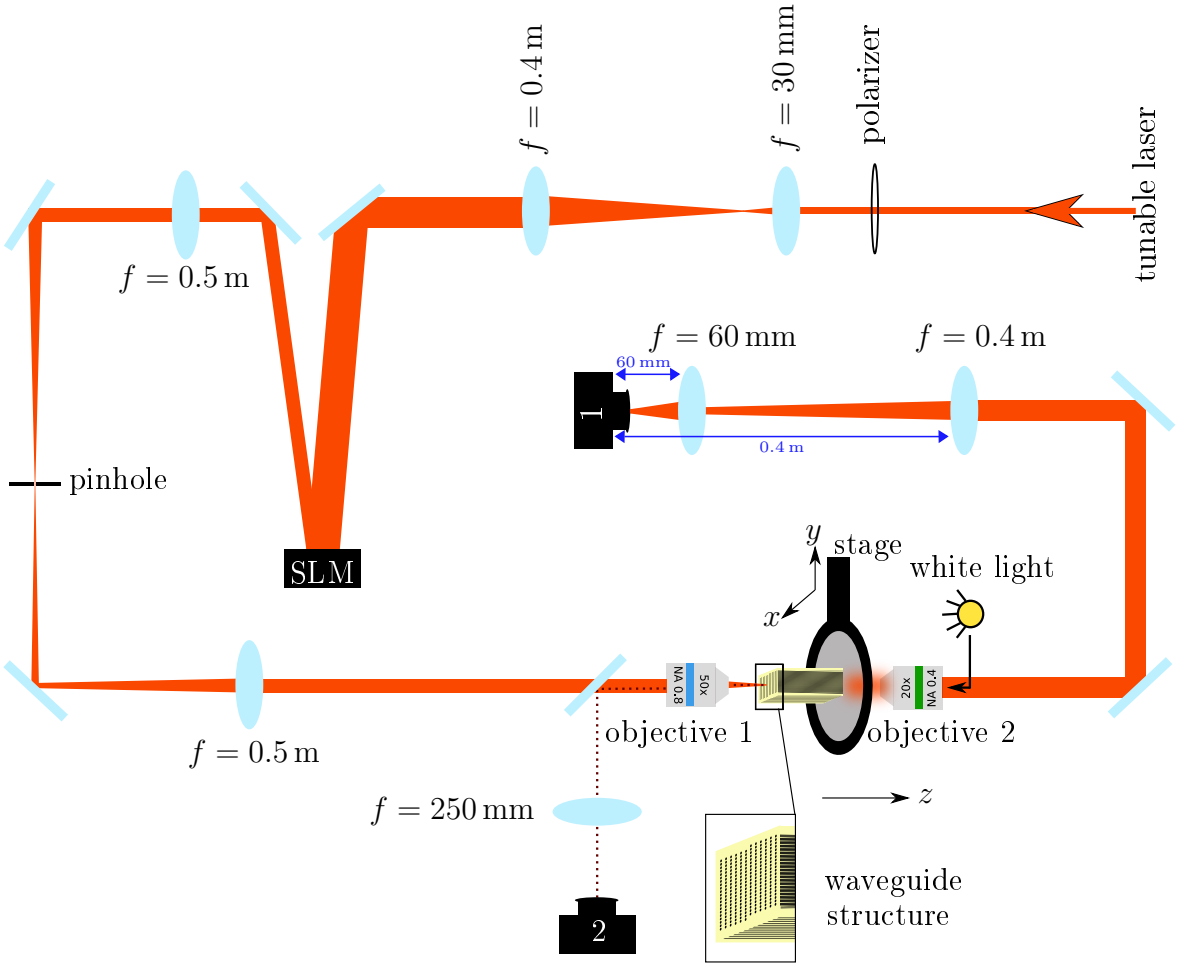

Figure 4.6: Sketch of the measurement setup. See main text for details.

loaded onto the SLM is then imaged by two lenses with a focal length of $f = 0.5\,\mathrm{m}$ in 4-f-configuration onto objective 1 (*Olympus*, 50x, NA 0.8). The objective Fourier transforms the pattern onto the sample's input facet. The location of the pattern relative to the waveguide positions can be controlled via the reflection of the pattern at the sample's facet and imaged via a beam-splitter and a lens onto camera 2. To shift the sample relative to the pattern, linear actuators allow moving it in the x-y-direction. After propagating through the sample, the light emerging from the sample output facet is collected by objective 2 (*Zeiss*, 20x, NA 0.4). It is then imaged by a tube lens ($f = 400\,\mathrm{mm}$) onto camera 1 for real-space measurements, or via the tube lens and a second lens (Bertrand lens [144], $f = 60\,\mathrm{mm}$) onto the camera for measurement of the Fourier-space (the k_x-k_y-plane).

The input-pattern consists of spots on a lattice used to address the waveguides. It is composed such that the diameter of each spot matches the diameter of a waveguide in the focus of objective 1, and the distances in x and y correspond to a_x and a_y respectively. The phase difference between the spots in x (y) is given by the desired

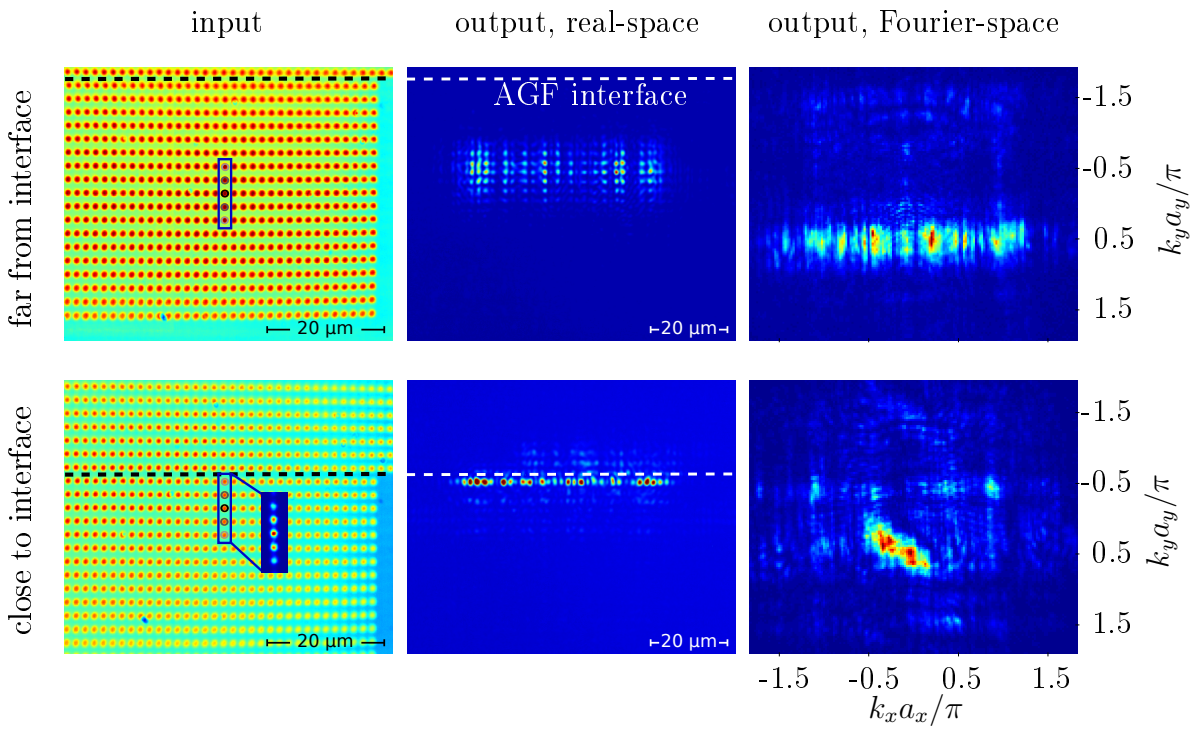

Figure 4.7: Comparison of the output in real-space (middle column) and k-space (right column) for light insertion far away from the AGF interface (upper row), or close to the AGF interface (lower row). Dashed lines mark the location of the AGF interface. The input position of the light is indicated by the blue frame. The inset to the left lowest image shows the five input spots. The image of the input facet is taken using white light illumination (left column). The wave vector component for the inserted beam was $k_y a_y = 0.5\pi$.

k_x (k_y). The pattern is enveloped with a Gaussian with full width at half maximum $\sigma_x = 5a_x$ and $\sigma_y = 5a_y$ for smooth amplitude drop towards its edges. An overlaid blazed grating causes the pattern to be reflected in the direction of the first maximum of the grating. This allows to exclude the directly reflected light that is not modulated by the SLM using an iris aperture.

4.4.2 Measurements

For the measurements, we choose an SLM pattern consisting of 5×1 spots in a column, aligned along the y-direction (see inset to Fig. 4.7), spaced with a_y with a defined k_y. By that, the in-coupling light contains all possible k_x but only a well-defined k_y. The spots are coupled into the waveguides below the AGF interface, as indicated by the blue frame in Fig. 4.7. This method allows recording the complete refraction and reflection properties of the beam crossing the AGF interface in one Fourier image for all k_x at once.

To conduct quantitative measurements we need to calibrate the axes of the Fourier-space images. To do so, we loaded onto the SLM patterns with defined k_y (or with defined k_x). These spots were coupled into waveguides well away from the waveguide arrays' AGF interface (see upper row in Fig. 4.7). The Fourier-space image of the output facet was recorded (see e.g. upper right image in Fig. 4.7). The intensity was summed over the k_x-axis (k_y-axis), to determine the position of maximum intensity along the axis to be calibrated. This pixel position was then mapped to the corresponding k_x (k_y) set in the SLM pattern.

Any tiny tilt due to misalignment of the beam results in a shift of k_x or k_y with respect to the input value we aimed at, which is determined by the SLM pattern. Therefore, also the real-space images were taken during the calibration procedure. From them, we determined the movement of the center of the wave packet. As this depends on the group-velocity $v_{g,x,y} = \partial\beta/(\partial k_{x,y})$ it shows a sinusoidal dependence on the k_x (k_y) value. Therefore, we fitted the measured wave packet's center of mass $COM_{x,y}$ along x (y) with

$$COM_{x,y} = \sin\left((k_{x,y} + \phi_{x,y})a_{x,y}\right) \tag{4.14}$$

to obtain the shift $\phi_{x,y}$ in the respective k-component. We then take this shift into account when plotting the Fourier images along the calibrated axes[(3)].

Fig. 4.7 shows the real-space and Fourier-space output for two different input positions. When we excite waveguides far away from the AGF interface, the light can not reach the AGF interface in the given propagation distance. In the Fourier image we then only see the k_y-values of the inserted light. However, moving the input pattern closer to the AGF interface, the output Fourier image undergoes a drastic change. The k_y-distribution around the input value of $k_{y,\mathrm{B}}a_y = 0.5\pi$ is changed and for large absolute values of k_x light is reflected into $k_{y,\mathrm{B}}a_y = -0.5\pi$. In the real-space image we see that also a large part of the intensity is concentrated at the AGF interface between the two arrays.

The Fourier images in the measurements look 'stripy'. This is due to inaccuracies in the position of the waveguides due to the fabrication. These inaccuracies cause noise in form of stripes in our data. Even small errors in the waveguides' positions cause noise in the Fourier image, as the intensity now sits at the wrong k-values. The maximum waveguide position error was estimated by SEM measurements to be about 20 nm in the x- and y-direction. Fig. 4.8 shows the influence of these position errors. In the OptiBPM calculations shown here, the real-space position of the waveguides in the x- and y-direction is shifted according to a random normally distributed number from the interval $[-20\,\mathrm{nm}, 20\,\mathrm{nm}]$.

(3) Due to the tilt of the waveguides with η, the group velocity in x is $v_{g,x} = 2J_x \sin(k_x a_x \pm k_0 \eta a_x) + \eta/a_x$, i.e., has an extra offset in k_x by about $\pm 0.07\pi$, where the sign depends on whether we do the calibration in the upper or lower array.

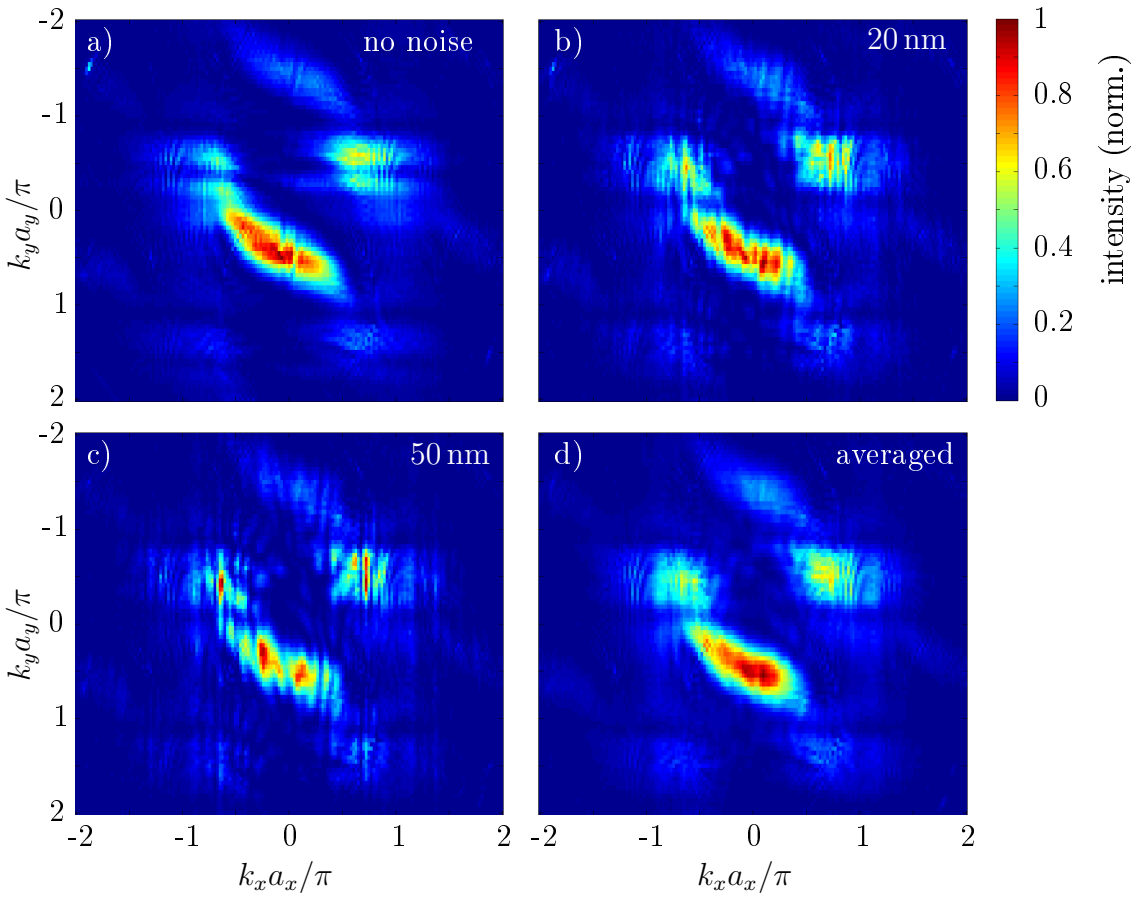

Figure 4.8: Influence of position noise on the Fourier image, OptiBPM calculations. a) Fourier image without noise. In b) the waveguides' positions are shifted by maximum 20 nm in the x- and y-direction, c) maximum 50 nm. d) Average over 6 Fourier images with position error of maximum 50 nm.

For the measurements, therefore, 10 images were taken for each fixed k_y at different positions along x. Then, the median over these images was taken to get rid of the noise. The results are shown in Fig. 4.3 and 4.4 for different $k_{y,\mathrm{B}}$. The dotted line shows the analytic curve according to Eq. (4.13). Note, that the analytic curve was calculated using the parameters measured by SEM on the inverse sample. The parameters measured at the sample's output facet in SEM might be slightly different from the parameters in the inner of the sample — either due to shrinking or due to the vacuum in the SEM. Also, the sample might swell again during infiltration. Furthermore, refractive indices are only known up to an uncertainty of 0.01 [145].

The comparison of the measurements (left column in Fig. 4.3 and 4.4) with OptiBPM calculations (right column) and the analytic curve therefore shows surprisingly good agreement with the expected k_y-distribution. As we can see, increased population of the k_y-component coincides well with the expected k_y-location of the refracted light. The reflected components are also visible. A video showing the complete measurements can be found in [142].

Despite the nice match between the experimental, numerical and analytic data, one open question remains: In the OptiBPM calculations we see increased intensity for values of $k_{y,\mathrm{out}}$ that neither correspond to reflected, nor refracted light at the AGF interface. Compare, e.g., for the part marked by the white arrow in the image with $k_{y,\mathrm{B}} = 0.3\pi/a_y$ in Fig. 4.3. OptiBPM calculations for k_y-values in this range showed, that the $k_{y,\mathrm{out}}$-position of this additional effect changes with $k_{y,\mathrm{B}}$. There seems to be an additional unexplained phenomenon causing this change in k_y. It might be due to some proportion of light that does not reach the AGF interface in the given propagation distance. Maybe this light interferes with the reflected and refracted part, leading to the seen discrepancies. Also, the finite width of the wave packet leads to unwanted (side-lobe) values of $k_{y,\mathrm{B}}$ being excited. As we used an input pattern with a rectangular shape in real-space, this resulted in a sinc-function in Fourier-space with side-lobes. These might also interfere with the other parts to disturb the expected behavior. Furthermore, edge modes living at the AGF interface between the two arrays could exist. Further investigation into this effect could lead to interesting results.

In this chapter, we have looked at the effect of an interface between two artificial gauge fields, created by a simple tilt of the waveguides. We deduced an analytic formula, similar to Snell's law, for the change in the wave vector of light traveling across the AGF interface. Our experimental measurements confirm the analytic model. The concept of artificial gauge fields is universal and applicable to many different kinds of systems. The ability to not only use the effect of an artificial gauge field itself, but also that of interfaces between multiple AGF, opens new possibility for gauge field engineering.

In the following chapter we will now move on to interfaces between more complex artificial gauge fields.

5 Interfaces in photonic Floquet topological insulators

In the previous chapter we have seen that an interface between two trivial artificial gauge fields (AGF) can have a profound impact on a wave traveling across it. In this chapter we look at interfaces between more sophisticated AGF. The AGF here are created by a Floquet drive (see also section 2.8). They model the effect of a magnetic field on electrons in a Quantum Hall system. As described in section 2.8 such a Floquet drive can induce non-trivial topology in a honeycomb lattice. The system is then characterized by a topological invariant, in this case the Chern number C. In a finite Floquet system, chiral edge states exist that encircle the edge of the structure unidirectionally. The bulk-boundary correspondence says that such edge states also exist at the interface between two topologically distinct systems. The number of edge states equals the difference between their topological invariants. Therefore, $2C$ edge modes should exist at the interface between a field with C and $-C$. In the following we will see that further interesting effects arise at the interfaces between Floquet topological insulators based on waveguides.

While there has been a lot of work published on interfaces between two topologically distinct areas in static systems, e.g. [5, 39, 146], interfaces between two different Floquet topological insulators have not seen much attention[(1)]. There are two conference abstracts that theoretically investigate interface modes at the boundary between two FTIs with identical topological invariants [147, 148]. We will place our findings in the context of these two works and discuss similarities and differences at the end of this chapter.

The work described in this chapter has initially been done in collaboration with Fabian Letscher and continued with Julian Schulz (both TU Kaiserslautern). At this point, it is a purely theoretical and numerical investigation, as the sample heights needed to do the corresponding experiments are not obtainable yet. However, experience has shown that OptiBPM calculations reflect the experimental results very well. Therefore we would expect to find the same effects in a waveguide experiment. The observations in this chapter motivated us to look at time-dependent defects in chapter 6, as we will see in the end.

(1) There are of course many publications on edge states at interfaces between an FTI and vacuum, but we are talking about interfaces between two FTIs here.

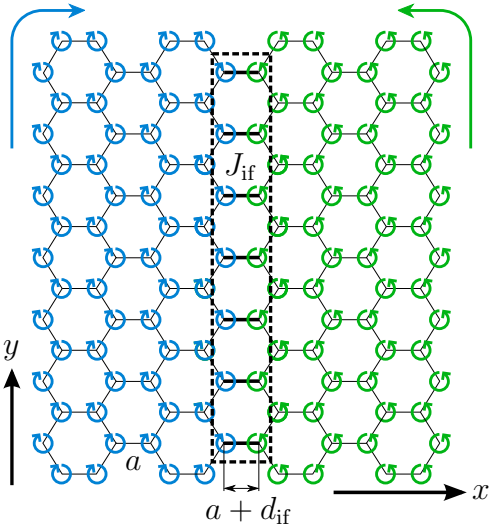

Figure 5.1: Scheme of the model system: Two neighboring fields of helical waveguides with different helicity. The field of blue helices has a Chern number of C, while it is $-C$ for the field of green helices. Expected direction of edge currents is indicated by the colored arrows. The coupling between waveguides of the same field is $J_{\text{lattice}} = 1$ (light bonds) and between the fields is J_{if} (dark bonds). The part with inter-field-coupling (dashed box) can be seen as an extra system, which leaves the rest terminated on bearded edges. The spacing a is the same as d_{NN} in sections 2.4.2 and 2.8. The additional distance d_{if} between the inner edge waveguides allows to tune J_{if}.

5.1 Setup

We couple two photonic Floquet topological insulators that consist of helically curved waveguides on honeycomb lattices. The waveguides in the two lattices have different helicity (see Fig. 5.1), corresponding to topological invariants of $C = 1$ and $C = -1$ respectively. Otherwise they are identical in terms of refractive indices, spacing, helix period Z etc. We interface these two lattices at their zigzag edges, such that the right and left outer waveguides of the left and right lattice, respectively, couple with each other.

Due to the bulk-edge correspondence we expect to find two unidirectional edge states at the interface between the two lattices [95], traveling in the same direction. OptiBPM calculations, however, showed that a state, excited at the interface with $k_y\sqrt{3}a = \pi$ can not leave the interface, but is trapped at that boundary between the two lattices (see video for $d_{\text{if}} = 0$ titled 'k = pi_excited_at_interface_d = 0.avi' in [142], and also next section). It moves up and down at the interface and, when reaching the upper or lower armchair edge, it is reflected. As this strikes us as a peculiar behavior, we want to look at this phenomenon in more detail.

5.2 Numerical results

Let us look at the results of the numerical calculations using OptiBPM. Videos of the propagation dynamics can be found in [142]. The parameters of the sample are: waveguide radius $r = 0.455\,\mu\text{m}$, waveguide spacing $a := d_{\text{NN}} = 1.45\,\mu\text{m}$, wavelength of light $\lambda = 633\,\text{nm}$, helix radius $R = 0.91\,\mu\text{m}$ and helix pitch $Z = 124\,\mu\text{m}$, corresponding to an amplitude of $A_0 a = 1.06$ and frequency $\omega = 3.3 J_{\text{lattice}}$ of the driving. In the first

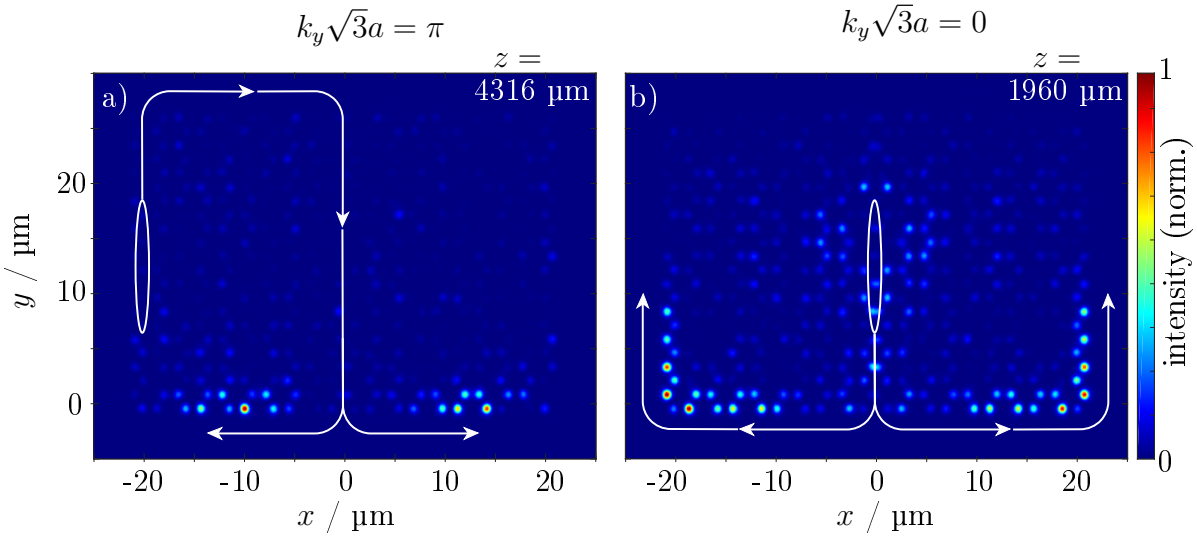

Figure 5.2: OptiBPM calculations of the intensity in the two arrays at different propagation distances z. Every image is scaled to maximum intensity separately. The white ellipse indicates the area where five neighboring waveguides were excited at $z = 0$. White arrows depict the flow of the excited light. The spacing between the two arrays is a (i.e. $d_{\mathrm{if}} = 0$, see text), such that they comprise a usual honeycomb lattice.

step, the two lattices with different helicity are spaced such that the center positions of the waveguides comprise a usual honeycomb lattice, i.e., the distance between the right outer waveguide of the left array to the left outer waveguide of the right array is a (see Fig. 5.1 with $d_{\mathrm{if}} = 0$). Note that for the chosen parameters, these waveguides overlap at certain points along z (in 'time'), as their distance varies with $d_x = a - 2R\cos(2\pi z/Z)$. However, we were not able to use a smaller helix radius R or larger distance a such that the waveguides did not overlap, as the resulting group velocity of the edge mode was too small then.

We excite an edge mode with $k_y\sqrt{3}a = \pi$ at the outer zigzag edge of the left lattice (see Fig. 5.2 a)). This edge mode travels along the zigzag edge unidirectionally, as usual, along the armchair edge into the interface. It moves on unidirectionally along the interface and finally splits into two packets at the lower edge of the interface. After that, one of the packets moves to the left and encircles the left lattice clockwise, while the other encircles the right lattice anti-clockwise. This is quite in accordance with what we expect for an interface between two photonic topological insulators with opposite Chern numbers. However, when we excite the interface with $k_y\sqrt{3}a = \pi$ (Fig. 5.3) the mode stays trapped inside the interface. It travels up and down and is always reflected at the top and bottom row of the interface waveguides.

We also excite the interface with $k_y\sqrt{3}a = 0$ (Fig. 5.2 b)). For a usual zigzag edge, no edge states are present in the band structure at $k_y\sqrt{3}a = 0$, such that any light usually spreads into the bulk. However, in our case we observe that the light is moving along the interface unidirectionally and escapes the interface at its lower edge to encircle the

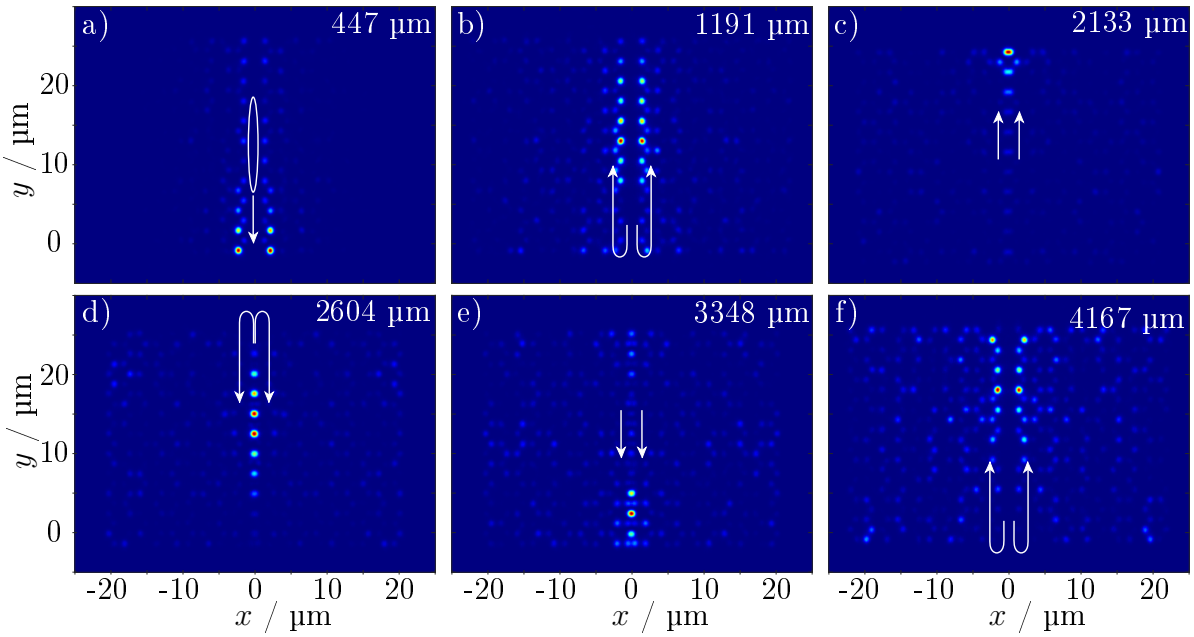

Figure 5.3: OptiBPM calculations of the intensity in the two arrays for $d_{\mathrm{if}} = 0$ and excitation at the interface with $k_y\sqrt{3}a = \pi$ at different propagation distances z. Every image is scaled to maximum intensity separately. The colorbar is the same as in Fig. 5.2. Initially, the interface mode travels downwards (in the negative y-direction), but is reflected at the lower edge, and thus bounces up and down in the interface.

structure as two chiral modes.

The behavior of the mode excited at the interface is quite interesting. It indicates that additional modes are present that do not arise in the band structure of two separated arrays.

In the next step, we move the two arrays farther apart, by introducing an additional distance between the inner edge waveguides (black bonds in Fig. 5.1) of $d_{\mathrm{if}} = 1.3\,\mu\mathrm{m}$, such that their total center-to-center distance is $a + d_{\mathrm{if}}$. For these parameters, the waveguides do not overlap anymore.

If we excite the waveguides at the left outer edge with $k_y\sqrt{3}a = \pi$ (Fig. 5.4 a)), we see the same behavior as before: The light moves along the edge into the interface and splits at the bottom into two packets. We however note that at the lower armchair edge more light moves into the right array than the left one. For an excitation of the interface with $k_y\sqrt{3}a = 0$ (Fig. 5.4 b)), the light very slowly moves towards the lower edge of the interface, but also a lot of intensity is spread into the bulk. Upon excitation of the interface with $k_y\sqrt{3}a = \pi$ (Fig. 5.4 c)), now part of the light moves upwards, and part moves downwards the interface. The downwards part couples out of the interface and splits, such that two modes encircle the edges of the two arrays. The upwards part is trapped in the interface.

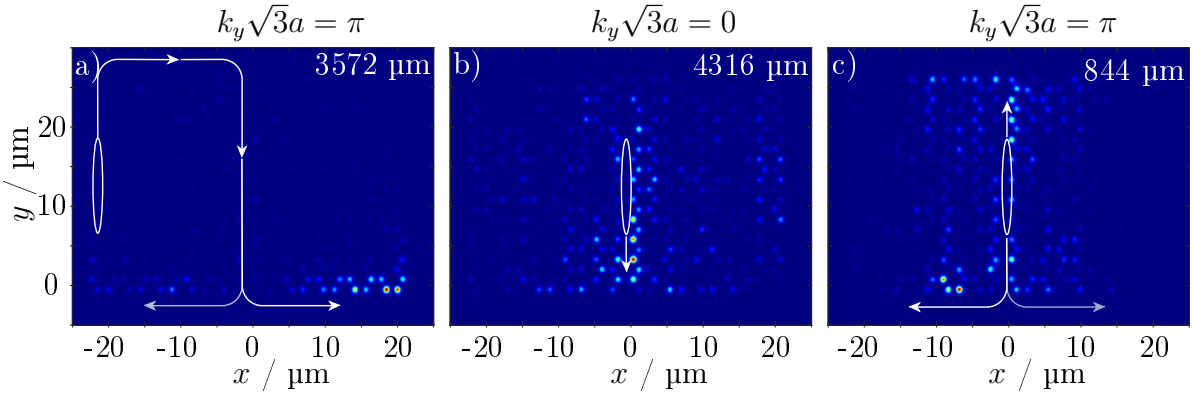

Figure 5.4: OptiBPM calculations of the intensity in the two arrays for $d_{\text{if}} = 1.3\,\mu\text{m}$ at different propagation distances z. The colorbar is the same as in Fig. 5.2. Every image is scaled to maximum intensity separately.

There are some similarities with what has been observed by [147]. The authors of this conference abstract look at an interface between two identical FTIs, where one is phase-shifted with respect to the other. They find interface modes at the boundary between the two FTIs, that they claim to be topological, although the topological invariants of the two arrays are identical. If the interface mode is excited, it moves along the boundary, and hybridizes with a topological edge mode at the armchair edge outside the boundary. In another recent work, Piccioli *et al.* proposed switching of a trivial interface mode via a topological edge mode at a boundary between two anomalous Floquet photonic TIs [148]. Again, the invariants of the two subsystems are the same. Here, the authors only observe trivial interface modes that can couple to topological ones for matching quasi-energy.

While both works observe a coupling between interface modes and edge states, none reports on trapped light in the interface, that bounces up and down between the armchair edges. In our case, it depends on the excitation, whether this trapping occurs, or if the structure works as a kind of beamsplitter for the topological edge mode.

We try to illuminate why this happens by looking at the band structure of the system. Our first approach is to retrieve the complex electric fields at certain propagation distances of the OptiBPM calculations and Fourier transform them along x, y and z. This yields the population in the bands. However, the resolution of the images is restricted by the limited number of waveguides that we can simulate and the limited propagation distance, due to simulation time and losses. Nevertheless, we can perceive additional population at the location of the bearded states in the band structure and on top of the bulk bands. Let's find a Hamiltonian that reflects the behavior of the system.

5.3 Band structure

We look into the system in more detail by calculating its band structure and eigenstates from its Hamiltonian. The different helicity of waveguides in the left and right lattice does not allow us to choose a common reference frame in which all the waveguides are stationary. Nevertheless we use the Peierls substitution to introduce complex coupling between waveguides in each individual lattice, induced by the lattice's vector field

$$\boldsymbol{A}_\mathbf{l} = A_0 \begin{pmatrix} \sin(\omega z) \\ -\cos(\omega z) \end{pmatrix} \qquad \text{and} \qquad \boldsymbol{A}_\mathbf{r} = -A_0 \begin{pmatrix} \sin(\omega z) \\ \cos(\omega z) \end{pmatrix} \tag{5.1}$$

in the left and right lattice, respectively. As in section 2.8, $A_0 = -\frac{2\pi}{\lambda} n_0 R\omega$ is the amplitude of the modulation, with the radius of the helices R and the frequency $\omega = 2\pi/Z$. In the limit where the two lattices are far apart from each other, it seems justified to treat each subsystem individually. We keep in mind that, using the Peierls substitution, any vector field enters the Hamiltonian in form of an additional phase to the hopping parameters. In terms of photonics, we can understand that by looking at the phase fronts of an in-coupling plane wave in a lattice of curved waveguides. In such a lattice, the phase fronts do not stay horizontal along z. Therefore, at each position in z the field between neighboring waveguides exhibits a phase difference. However, we argue that the phase difference at the interface between two oppositely curved lattices should be zero due to continuity conditions. Therefore, we only add the Peierls phases to the hoppings inside each lattice and assume a real coupling between the two arrays. We can also see that the coupling between the two arrays must be real, by looking at the symmetry of the complete system. As the complete system is invariant under taking x to $-x$ (but not each individual array), no additional phase can occur in the coupling between the two subsystems.

We normalize the amplitude of all couplings to the hopping inside one lattice $J_\text{lattice} = 1$. To obtain the band structure, we have to solve the Schrödinger equation to get the eigenenergies of the Hamiltonian. The Hamiltonian for each individual lattice is

$$H_\text{l/r} = \sum_{m,n} \left[J_{1,\text{l/r}} \hat{a}^\dagger_{m,n} \hat{b}_{m,n} + J_{2,\text{l/r}} \hat{a}^\dagger_{m,n+1} \hat{b}_{m,n} + J_{3,\text{l/r}} \hat{a}^\dagger_{m,n} \hat{b}_{m-1,n} \right] + \text{h.c.}, \tag{5.2}$$

with the couplings $J_{1-3,\text{l/r}}$ in the left/right lattice (see also section 2.8).

We consider a system that is infinite in y, but finite in the x-direction with $2L_x$ lattice sites. Then, we can Fourier transform our operators $\hat{a}_{m,n}$ and $\hat{b}_{m,n}$ in the y-component, such that

$$\hat{a}_{m,n} = \sum_{k_y} \hat{a}_{m,k_y} \exp\left(-\mathrm{i} k_y n\right) \tag{5.3}$$

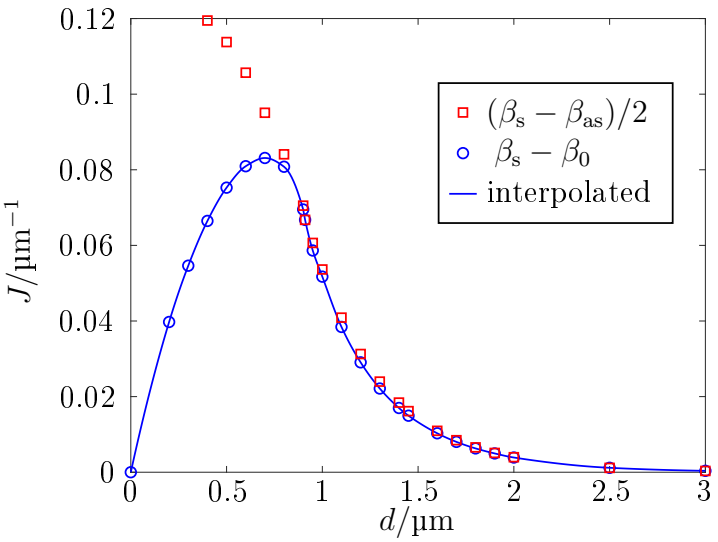

Figure 5.5: Coupling constants J in dependence on the center-to-center distance d. Blue circles are calculated from the difference between β_s for the symmetric supermode and β_0 of a single waveguide, while red squares give the difference between the propagation constants of the symmetric and anti-symmetric supermode. The values for the respective propagation constants were determined using *COMSOL*'s eigenmode solver in the package "electromagnetic waves, beam envelopes". The blue line interpolates data points for the blue circles.

and likewise for $\hat{b}_{m,n}$. Thus, the Hamiltonian now reads

$$H_{\mathrm{l/r}}(k_y) = \sum_m \left[\left(J_{1,\mathrm{l/r}} + J_{2,\mathrm{l/r}} \exp\left(\mathrm{i}k_y\right) \right) \hat{a}^\dagger_{m,k_y} \hat{b}_{m,k_y} + J_{3,\mathrm{l/r}} \hat{a}^\dagger_{m,k_y} \hat{b}_{m-1,k_y} \right] + \mathrm{h.c.} \tag{5.4}$$

with the complex hoppings obtained by Peierls substitution

$$J_{p,\mathrm{l/r}} = J_{\mathrm{lattice}} \exp\left(\mp \mathrm{i} A_0 a \sin\left(\omega z \mp \frac{2\pi}{3} p \right) \right) \quad \text{with} \quad p = 1,2,3. \tag{5.5}$$

We can now solve the Schrödinger equation for each specific k_y to obtain the L_x eigenenergies and eigenmodes of the system along x. The Hamiltonian for the complete system is now built of the Hamiltonians for each subsystem that are coupled via a different coupling at the interface J_if

$$\begin{aligned} H_{\mathrm{complete}}(k_y) = & \sum_{m=1}^{L_x} \left(J_{1,\mathrm{l}} + J_{2,\mathrm{l}} \exp\left(\mathrm{i}k_y\right) \right) \hat{a}^\dagger_{m,k_y} \hat{b}_{m,k_y} + J_{3,\mathrm{l}} \hat{a}^\dagger_{m,k_y} \hat{b}_{m-1,k_y} \\ & + \sum_{m=L_x+1}^{2L_x} \left(J_{1,\mathrm{r}} + J_{2,\mathrm{r}} \exp\left(\mathrm{i}k_y\right) \right) \hat{a}^\dagger_{m,k_y} \hat{b}_{m,k_y} + J_{3,\mathrm{r}} \hat{a}^\dagger_{m,k_y} \hat{b}_{m-1,k_y} \\ & + J_\mathrm{if} \hat{a}^\dagger_{L_x+1,k_y} \hat{b}_{L_x,k_y} + \mathrm{h.c.} \end{aligned} \tag{5.6}$$

The coupling J_if approximately decays exponentially with the spacing between waveguides from the two lattices, which changes periodically along z, as two interfacing

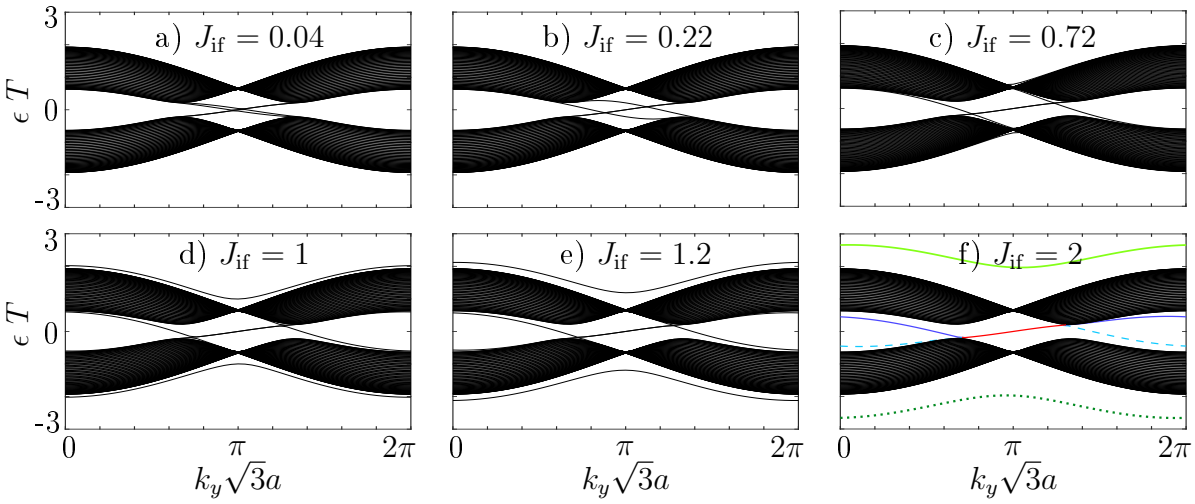

Figure 5.6: Band structures of the two coupled lattices with $\omega = 10J_{\mathrm{lattice}}$ and $A_0 a = 1.3$: For increasing coupling J_{if} between the lattices, the zigzag modes on the edge between the fields split and transform into bearded-like edge states. Additionally, new bands above and below the bulk bands arise at the boundary. For $J_{\mathrm{if}} = 2$: bulk bands black, outer zigzag-edge red, inner bearded-like edges blue, interface modes green.

waveguides have different helicity. The distance d_x in the x-direction between helices with opposite helicity varies along z according to $d_x = a + d_{\mathrm{if}} - 2R\cos(2\pi z/Z))$. For values of d_x where the waveguides overlap, i.e. $d_x < 2r$, the coupling deviates from the exponential decay. Fig. 5.5 shows the coupling between two waveguides over their distance. To extract the red squares, we calculated the effective refractive indices of the anti-symmetric and symmetric supermodes for two waveguides at varying distances d, and deduced the coupling according to Eq. (2.30). For decreasing values of d the anti-symmetric supermode becomes less localized and more and more radiative. Therefore we calculate the hopping from the difference between β_{s} of the symmetric supermode and β_0 of a single waveguide (blue circles in Fig. 5.5). We see that both approaches yield the same values only for distances $d > 2r$. From the extracted values of the blue circles, we interpolate all values of J_{if} (blue curve) that we need to calculate the band structure.

Introducing an additional distance d_{if} between the two lattices, such that the total distance between the interface waveguides becomes $a + d_{\mathrm{if}}$, allows us to tune J_{if} via d_{if}. The projected band structures of the complete system are shown in Fig. 5.6 for different values of J_{if}. Here, the parameters of the helical driving are $\omega = 10J_{\mathrm{lattice}}$ and $A_0 a = 1.3$.

We start with two uncoupled lattices, such that $J_{\mathrm{if}} = 0$, i.e., the two lattices are infinitely far apart from each other, $d_{\mathrm{if}} = \infty$. Then, the individual band structures for the left and right lattice are degenerate, but the one for the left lattice is mirrored along k_y with respect to the one for the right lattice. With increasing J_{if} (i.e. decreasing d_{if})

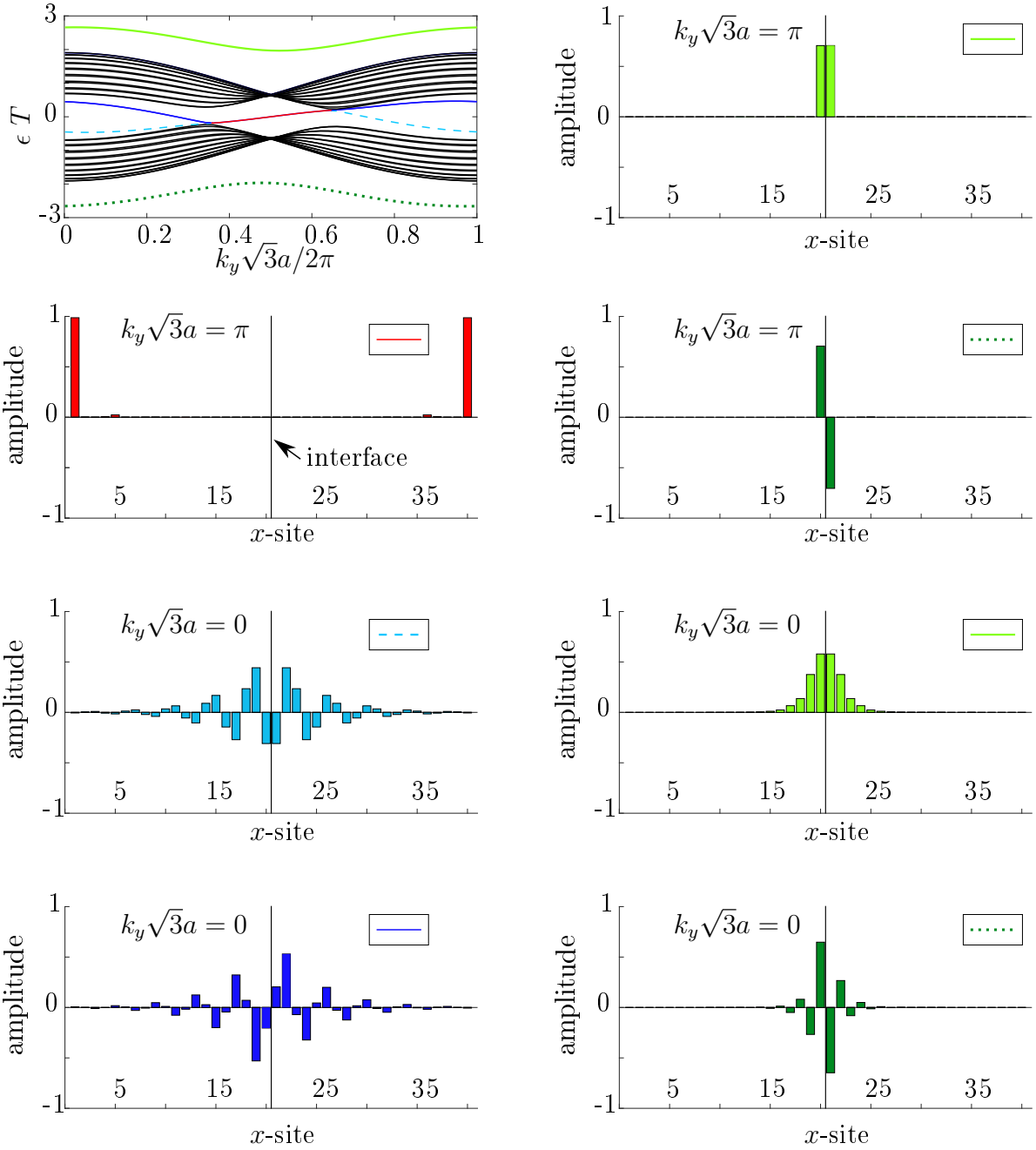

Figure 5.7: Projected wave functions in real-space for the bands marked in color. Parameters are as in Fig. 5.6 with $J_{\text{if}} = 2$. Shown are the weights of the real parts of the wave functions on the sites along x (the absolute square of the wave functions is normalized to 1). The black line marks the location of the interface. For $k_y\sqrt{3}a = \pi$ the green wave functions only have weight at the two interface sites, while they are exponentially localized around the interface for other values of $k_y\sqrt{3}a = 0$. The two degenerate red modes live at the outer zigzag edges. The blue states are bearded-like edge states near the interface, with also some weight at the interface sites (site 20 and 21). The wave functions of the dark blue (solid line) and dark green (dotted line) bands have anti-symmetric amplitudes on the interface sites.

the two energy bands for the zigzag edges between the lattices (black dashed box in Fig. 5.1) split (see Fig. 5.6 b) and c)), and shift their position in k-space until they resemble bearded edge states (marked blue in Fig. 5.6 f)). Additionally, for $J_{\mathrm{if}} \geq 1$ new cosine-shaped bands (green in Fig. 5.6 f)) appear above and below the bulk bands.

In the range $J_{\mathrm{if}} > 1$ the coupling between the waveguides at the inner edge between the lattices is stronger than to the other waveguides. Therefore, we can basically consider the lattice to be split into three parts: the left lattice with a bearded edge termination to its right, dimer pairs of waveguides in the middle, and the right lattice with a bearded edge termination to its left. We now look at the shape of the eigenfunctions in real-space (Fig. 5.7). We see that the wave functions corresponding to the green bands are localized around the interface in real-space (Fig. 5.7 green bars). We will call these states the interface states. The states corresponding to the blue bands are bearded-like states — bearded states near the interface between the two lattices, with some amplitude also on the interface sites (Fig. 5.7 blue bars).

We now keep J_{if} fixed at $J_{\mathrm{if}} = 2$ and change the helix radius. By tuning the helix radius

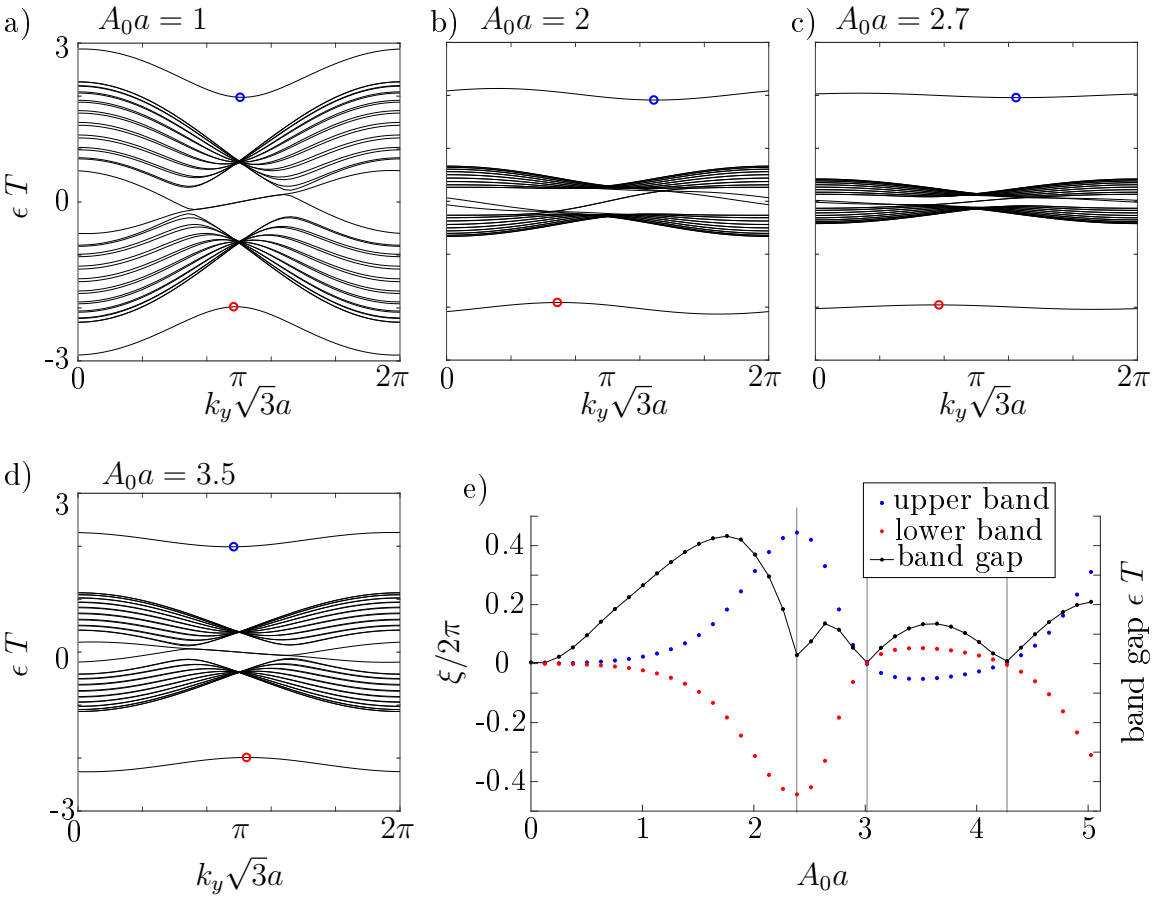

Figure 5.8: a)-d) Band structures for $\omega = 10J_{\mathrm{lattice}}$, $J_{\mathrm{if}} = 2$ and different values of A_0a. e) The shift of the interface band ξ in dependence on the amplitude A_0a (compare also Fig. 2.10).

we tune the driving amplitude A_0 and can thus go through the topological phase space (see section 2.8 and e.g. [83]). Fig. 5.8 shows the band structures for certain values of A_0. We see that the two cosine-shaped interface bands are not mirror symmetric with respect to $\epsilon T = 0$ for all values of A_0. We fit the cosine-band of an interface mode with $\cos\left(k_x\sqrt{3}a + \xi\right)$ to retrieve the shift ξ of the band in dependence on the amplitude A_0 of the helical driving. The phase-shift ξ is plotted along A_0 in Fig. 5.8 e) for the upper (blue) and lower (red) cosine-band, together with the size of the bulk band gap (black). The origin of this shift remains a puzzle, and we can only guess that it is attributed to a non-matching Peierls phase between the left and right lattice.

We now want to compare the band structures to the population in k-space obtained by the Fourier transformation of the OptiBPM calculations (Fig. 5.9). To retrieve the population in k-space, we summed up the Fourier transforms of the three simulations with different initial excitation conditions ($k_y\sqrt{3}a = 0$ and $k_y\sqrt{3}a = \pi$ excited at the interface, and $k_y\sqrt{3}a = \pi$ excited at the outer zigzag edge) for each of the two values of d_{if}. This way, we can of course not populate the complete k-space, but only patches of it that match the initial conditions. Nevertheless, it allows us to get an idea about the shape of the band structure of the system.

We first note that the driving amplitude and frequency corresponding to the OptiBPM calculations are $A_0 a = 1.06$ and $\omega = 3.31 J_{\text{lattice}}$. For such small values of ω things become a little more complicated, as different orders of Floquet replicas already start to overlap. From the Hamiltonian in Eq. (5.6), we numerically calculate the band structures that correspond to the two cases of additional distance $d_{\text{if}} = 0$ and $d_{\text{if}} = 1.3\,\mu\text{m}$ by using the correct coupling for J_{if} in every timestep, obtained by the interpolated values in Fig. 5.5. The results are shown in Fig. 5.9. Note that here, we plot two Brillouin zones along k_y from $k_y\sqrt{3}a = -2\pi$ to 2π and three Floquet Brillouin zones along ω (the yellow boxes mark one).

We see that the band structure for $d_{\text{if}} = 1.3\,\mu\text{m}$ (lines in Fig. 5.9 a)) agrees quite well with the sum of the k-space population (grey pixels) of the three OptiBPM calculations. For $d_{\text{if}} = 1.3\,\mu\text{m}$, we seem to be in the regime $J_{\text{if}} < 1$. We can see the edge state of the outer zigzag edge and two bearded-like edge states in the band gap. There are also interface states, but they are very close to the bulk bands (as in Fig. 5.6 for $J_{\text{if}} = 1$). The band structure also explains why we can not trap a lot of light in the interface in Fig. 5.4 c), as we excite the bearded-like edge states at the interface along with the interface mode at $k_y\sqrt{3}a = \pi$. On the other hand, upon excitation with $k_y\sqrt{3}a = 0$ at the interface, we only excite those bearded-like edge states. However, they have a very low group velocity here, as the slope of their bands is very small in this regime of k_y.

Looking at the band structure for the case $d_{\text{if}} = 0$ (Fig. 5.9 b), we see that it does not fit to the k-space population of OptiBPM so well. We can only see the outer zigzag band (marked red) and one of the bearded-like bands (dashed light blue) in the Fourier

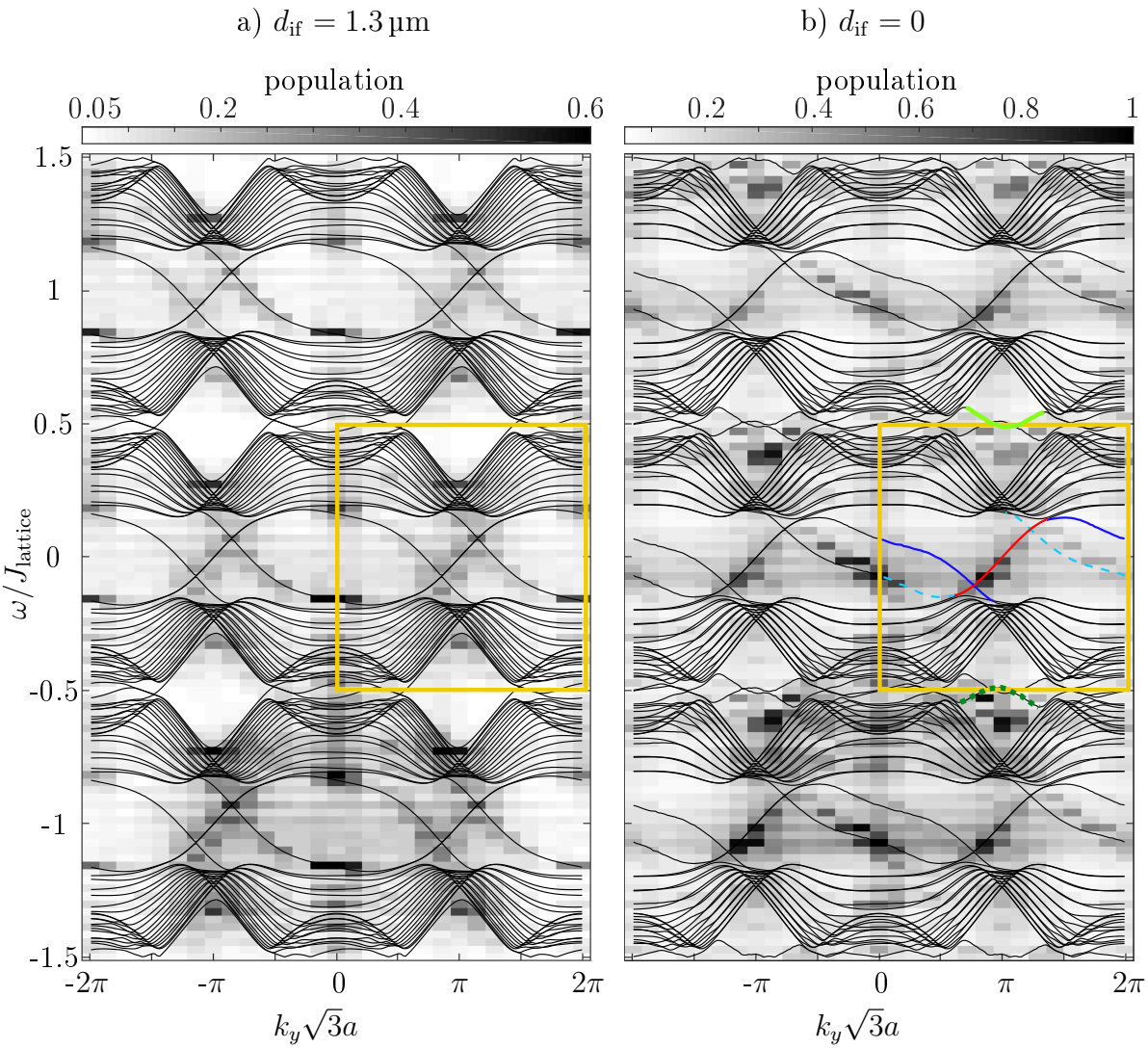

Figure 5.9: Numerically calculated band structures using the tight-binding Hamiltonian (lines), in comparison with the population in k-space obtained by the Fourier transformation of the OptiBPM calculations (grey pixel). The yellow boxes mark one Brillouin zone. For $d_{\mathrm{if}} = 0$ the bands in the first Brillouin zone are colored as in Fig. 5.7. We see that the dark blue (solid line) and the dark green (dotted line) bands are not present in the OptiBPM calculation.

transform. Also, the interface mode does not fit, but seems to be lower in energy and have a larger slope in the OptiBPM calculations than the band structure predicts. A possible explanation is that this is due to the overlapping between the waveguides. Eigenmode calculations in *COMSOL* showed that for overlapping waveguides the anti-symmetric supermode becomes radiative. This means that only modes that have a symmetric amplitude distribution at the interface are left. Looking again at Fig. 5.7, we see that the dark blue (solid line) bearded-like band and the dark green (dotted line) interface band have an anti-symmetric amplitude at the interface sites. Therefore, they must vanish from the band structure for overlapping waveguides. Still, the light

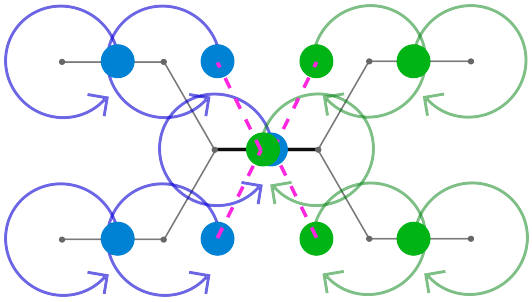

Figure 5.10: Sketch of the setup for the case $d_{\mathrm{if}} = 0$. When the interface waveguides overlap, we can not neglect the coupling from the left blue interface waveguide to the green lattice and vice versa (pink dashed line).

green interface mode (solid line) should sit at lower energies according to the k-space population obtained from OptiBPM in Fig. 5.9 b). The origin of that remains an open question. It might be due to next-nearest neighbor coupling. In the Hamiltonian, we did not consider the next-nearest neighbor coupling of the interface waveguides in one array to the near-interface waveguides in the other array (sketched in Fig. 5.10). When the waveguides strongly overlap, however, this effect is probably not negligible.

We want to give a possible explanation for the 'bouncing' of the interface mode for $d_{\mathrm{if}} = 0$. As stated before, there is a slight shift of the cosine-shaped interface band in k-space. Therefore, upon excitation with $k_y\sqrt{3}a = \pi$, the trivial interface mode is initially excited at a monotone slope with a finite group velocity [(2)]. Due to this it moves down until it encounters the lower edge of the interface. Here, it cannot couple to the armchair edge mode, as the energies of the two modes do not match (remember that the armchair mode lives in the band gap). Thus, the interface mode has to change in k_y, presumably such that the encountered group velocity has the opposite sign, while the quasi-energy is preserved.

In summary we see that we can trap light at the interface between two FTIs for certain distances between the two arrays. For overlapping waveguides, one of the interface modes is destroyed, and light bounces up and down when excited in the remaining interface mode. We can change the behavior of the interface mode via the distance between the two arrays. It would be interesting to see, if such an initially trapped interface mode can be coupled to a topological edge mode upon a fast increase in the distance between the lattices d_{if}. This way, one could 'store' a topological edge mode until needed. Also, the possibility to alter the band structure by making waveguides overlap, opens new prospects for band structure engineering.

Following the observations of this chapter, we now want to shrink one of the arrays with respect to the number of waveguides. In the ultimate limit, this corresponds to having just one single waveguide with opposite helicity than the rest of the lattice. In the next chapter, we examine the influence of such a defect on the robustness of a topological edge mode.

(2) Of course, at $k_y\sqrt{3}a = \pi$ another edge mode exists in the band gap (red one in Fig. 5.6). However, spatially it only lives at the outer zigzag edges, and can not be populated when only exciting the interface.

6 Dynamic defects

We have seen in chapter 4 that an interface between two arrays with different artificial gauge fields has a pronounced effect on a wave traveling across that interface. In the previous chapter we have explored the influence of such an interface between two FTIs on a topological edge mode. We now take the model from chapter 5 and shrink one of the fields into just one waveguide. This results in a defect with a 'different AGF'. We will call this a dynamic defect, as the coordinates of the defect are time-dependent in the frame of reference, in contrast to the main lattice.

For a topological insulator it is known that the topological edge mode is robust against spatial disorder and static defects [1, 3, 95]. The role of time-dependent defects however remained unsolved, although there has been some theoretical work on time-dependent coupling between sites [149, 150] and time-dependent potential variations [151, 152].

In this chapter we explore the effect of both coupling and on-site potential variation of such a time-dependent defect on a topological edge mode. We start with a single defect in a modulated honeycomb lattice.

6.1 Dynamic defects in a Floquet topological insulator — same periodicity

The work presented in this section was done in collaboration with Fabian Letscher (TU Kaiserslautern) and published in [57].

The question we want to answer is: Do time-dependent defects lead to scattering of a topological edge state into the bulk[(1)]? To do so, we introduce single defects into the zigzag edge of a photonic Floquet topological insulator, that consists of helically curved waveguides on a honeycomb lattice. Again, note that time is mapped to the spatial z-axis in our waveguide system. Therefore, the term 'time-dependent' is equivalent to 'z-dependent' here.

(1) Backscattering can, however, not be induced by the defect, as the edge mode with the opposite sign of the group velocity lives on the edge on the other side of the sample.

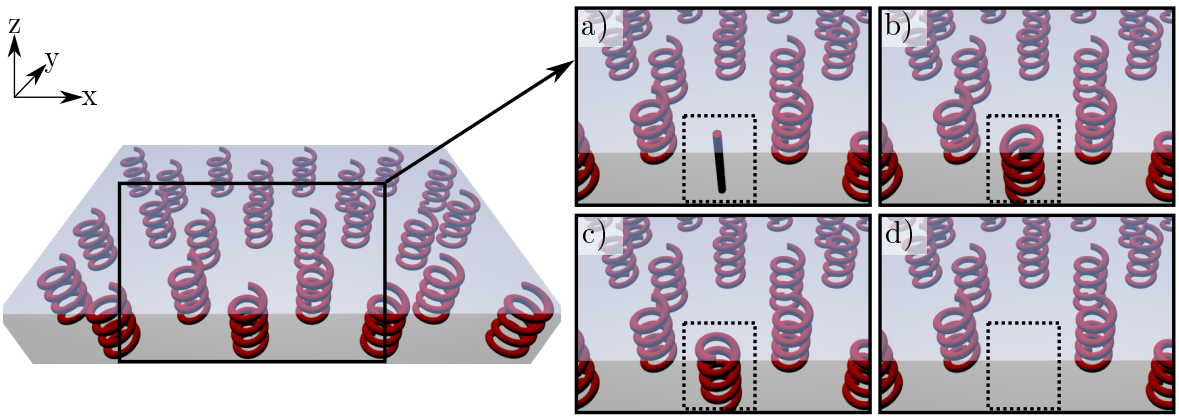

Figure 6.1: Sketch of the waveguide samples with time-dependent defects: a) straight defect, b) defect with opposite helicity, c) defect with the same helicity but shifted by half a helix pitch. For comparison a missing waveguide (i.e. a static defect) is shown in d). Each of the defect waveguides substitutes an outer waveguide at the zigzag edge of the honeycomb lattice. Taken from [57] licensed under [38].

We look at three different kinds of time-dependent defects (depicted schematically in Fig. 6.1): 1) a straight waveguide, 2) a waveguide with opposite helicity, and 3) a waveguide with the same helicity, but phase-shifted by π, i.e., half a helix pitch in the z-direction. All of them share the same periodicity Z with the original lattice. Defects with different periodicity will be addressed in section 6.2 and 6.3.

Analytically, we treat this system similarly to the 'clean' Floquet topological insulator (see chapter 2). We change into a frame of reference that moves with the helical bulk waveguides, which means that these waveguides are now static in the new coordinate system. In this frame of reference, however, the defects are not static, but their position changes in time, i.e., along z. Therefore we call these defects 'dynamic', or time-dependent defects. In the new reference frame, the system without defect is now described by a time-independent Hamiltonian and an additional global vector field $\boldsymbol{A}(t)$. Using Peierls substitution the static hoppings obtain a time-dependent phase (see sections 2.7 and 2.8), inducing the system's non-trivial topological behavior.

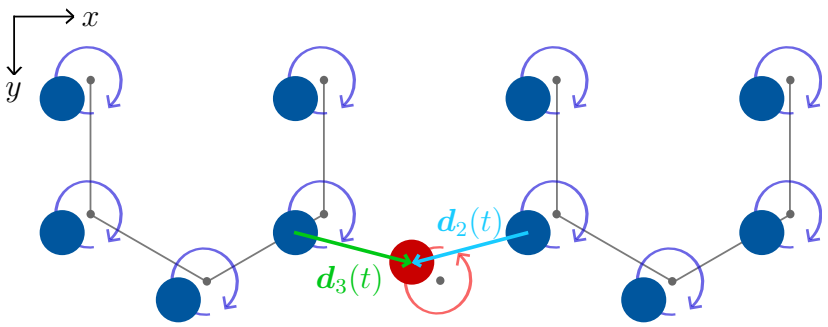

Figure 6.2: Sketch of the time-dependent vectors $\boldsymbol{d}_2$ and $\boldsymbol{d}_3$ from the defect to its neighbors in the case of the defect with opposite helicity.

For the case of the three considered kinds of defects we have now a distance $\boldsymbol{d}(t)$ between the defect and its neighbors that changes with time (see Fig. 6.2). This has two effects on the hopping: First, it makes the amplitude of the hopping J time-dependent: $\tilde{J}(t)$, as the hopping amplitude depends on the distance between the waveguides. Second, the phase also gains an additional term, as the Peierls phase is given by $\boldsymbol{A}\cdot\boldsymbol{d}$, where $\boldsymbol{d}$ is now $\boldsymbol{d}(t)$. Note, that the defect still falls under the global coordinate transformation and thus under a global vector field $\boldsymbol{A}$. Let us calculate the hoppings from the defect to its neighbors for the three cases (see also Fig. 6.2).

For the straight waveguide:

$$\boldsymbol{d}_{2,\text{straight}} = \boldsymbol{d}_2 - (R\cos(\omega t), R\sin(\omega t))\,, \tag{6.1a}$$
$$\boldsymbol{d}_{3,\text{straight}} = \boldsymbol{d}_3 - (R\cos(\omega t), R\sin(\omega t))\,, \tag{6.1b}$$

and

$$J_{2,\text{straight}} = \tilde{J}_2(t)\exp\left(-\mathrm{i}A_0 a\sin\left(\omega t - \frac{2\pi}{3}\right)\right), \tag{6.2a}$$
$$J_{3,\text{straight}} = \tilde{J}_3(t)\exp\left(-\mathrm{i}A_0 a\sin\left(\omega t - \frac{4\pi}{3}\right)\right). \tag{6.2b}$$

Here, only the amplitude of the hopping changes, as $\boldsymbol{A}\cdot(R\cos(\omega t), R\sin(\omega t)) = 0$. The same is valid for the waveguide with same helicity, but phase-shifted:

$$\boldsymbol{d}_{2,\text{phasesh}} = \boldsymbol{d}_2 - 2\,(R\cos(\omega t), R\sin(\omega t))\,, \tag{6.3a}$$
$$\boldsymbol{d}_{3,\text{phasesh}} = \boldsymbol{d}_3 - 2\,(R\cos(\omega t), R\sin(\omega t))\,. \tag{6.3b}$$

For the defect with opposite helicity we obtain both a change in the hopping amplitude and an additional phase, as

$$\boldsymbol{d}_{2,\text{opp}} = \boldsymbol{d}_2 - (0,\ 2R\sin(\omega t))\,, \tag{6.4a}$$
$$\boldsymbol{d}_{3,\text{opp}} = \boldsymbol{d}_3 - (0,\ 2R\sin(\omega t))\,, \tag{6.4b}$$

and thus

$$J_{2,\text{opp}} = \tilde{J}_2(t)\exp\left(-\mathrm{i}A_0 a\sin\left(\omega t - \frac{2\pi}{3}\right)\right)\exp\left(\mathrm{i}RA_0\sin(2\omega t)\right), \tag{6.5a}$$
$$J_{3,\text{opp}} = \tilde{J}_3(t)\exp\left(-\mathrm{i}A_0 a\sin\left(\omega t - \frac{4\pi}{3}\right)\right)\exp\left(\mathrm{i}RA_0\sin(2\omega t)\right). \tag{6.5b}$$

In the experiment, we have chosen two different regimes: For the first one, the new coupling of the defect to its neighbors only changes slightly with respect to the coupling

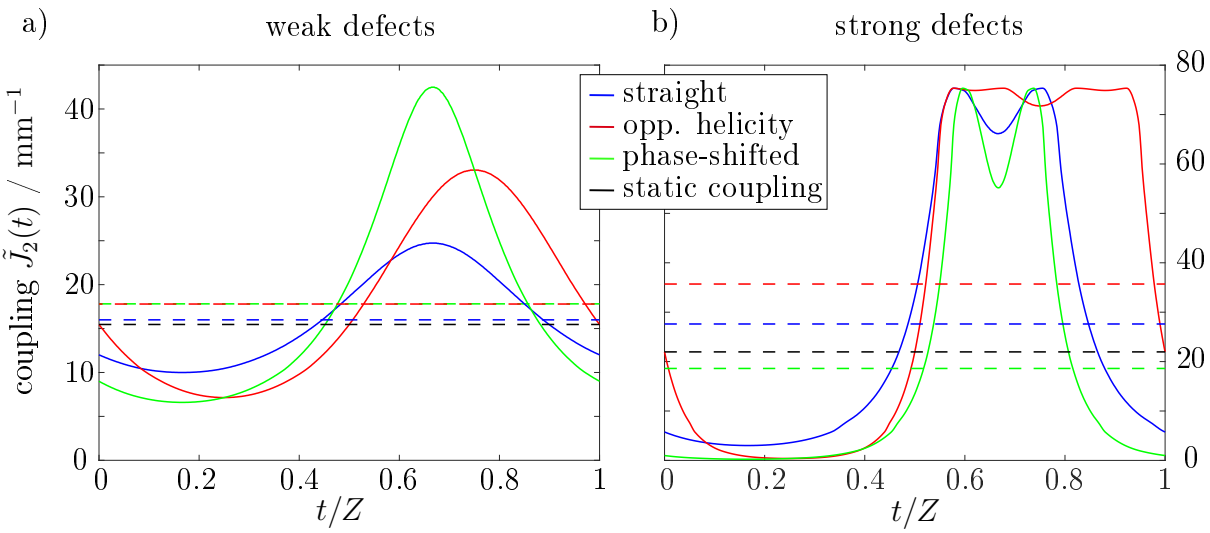

Figure 6.3: Time-dependent hopping amplitudes of the defect to its neighbors for the parameter set of a) weak defects and b) strong defects. The dashed lines represent the time-averaged coupling constants. The hopping amplitudes were interpolated as described in the caption of Fig. 5.5.

for the rest of the lattice. We call these defects 'weak' defects. In the second regime, the coupling changes strongly, and the defects are therefore dubbed 'strong' defects. The time-dependent hopping amplitudes for both cases are plotted in Fig. 6.3 for the three different defects, along with their time-averaged value. Note that the straight and the phase-shifted strong defect waveguide spatially overlap with their neighboring waveguides at certain times. This is the case whenever the distance is smaller than the waveguide diameter $|\boldsymbol{d}_{2,\text{straight}}| < 2r$ or $|\boldsymbol{d}_{2,\text{phasesh}}| < 2r$.

In addition to that, the straight defect has a different on-site potential, due to its missing curvature (see chapter 2, Eq. (2.73))

$$\Delta V = \frac{k_0}{2} R^2 \omega^2. \tag{6.6}$$

6.1.1 Experiments

To observe qualitatively, whether the defects lead to scattering of an edge mode into the bulk, we perform experiments using waveguide arrays. The samples are fabricated as described in section 3.1. All of the waveguides' coordinates are programmed using a *MATLAB* code for one period Z. Also, during the DLW process, a framework was co-written in each layer to stabilize the waveguide structure. SEM images of the direct laser written inverse waveguide structure after development for the case of a weak and a strong defect are shown in Fig. 6.4. These images as well as the one of the measurements might give the impression that the defect is farther away from the edge

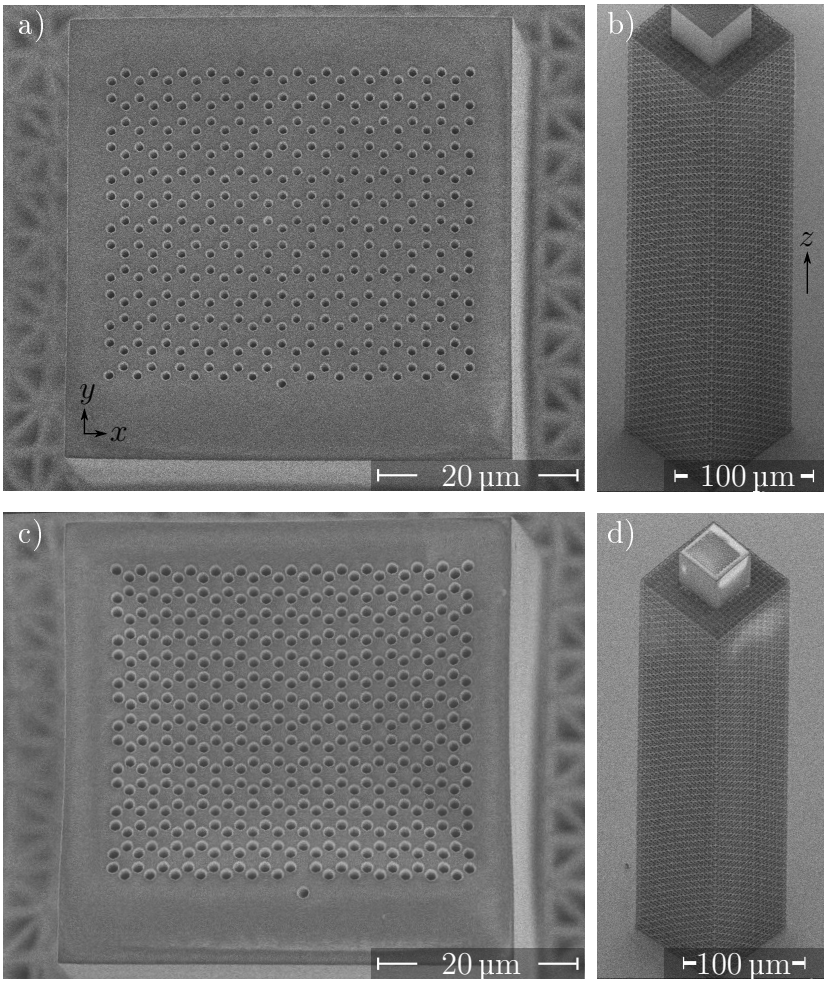

Figure 6.4: Scanning electron microscopy images of the inverse waveguide samples with phase-shifted defect: a) top view and b) view tilted by 42° (structure with supporting framework) of sample with weak defect. c) top view and d) view tilted by 42° of sample with strong defect.

than the rest of the waveguides. However, the defect's mean position is still at a regular lattice site (see Fig. 6.2 or insets to Fig. 6.6 and 6.7). The impression only arises, as the height of the samples was chosen to be a half integer multiple of Z.

For each kind of defect we fabricated two samples in different parameter ranges. The first set is for weak defects, i.e., weak modulation of the coupling between defect and neighbors. This corresponds to a large spacing between waveguides $a = (1.65 \pm 0.06)\,\mu\text{m}$ and a small helix radius $R = (0.36 \pm 0.01)\,\mu\text{m}$ at a helix pitch of $Z = (72 \pm 6)\,\mu\text{m}$ and waveguide radius of $r = (0.37 \pm 0.03)\,\mu\text{m}$. In the measurements we used a wavelength of $\lambda = 810\,\text{nm}$, to have a large enough group velocity of the edge mode. In the second set, the modulation in the coupling is strong for $a = (1.40 \pm 0.03)\,\mu\text{m}$ and $R = (0.89 \pm 0.01)\,\mu\text{m}$ at $Z = (85 \pm 3)\,\mu\text{m}$ and $r = (0.49 \pm 0.03)\,\mu\text{m}$. Here, the used wavelength was $\lambda = 710\,\text{nm}$. The parameters for r, a and h were determined via SEM

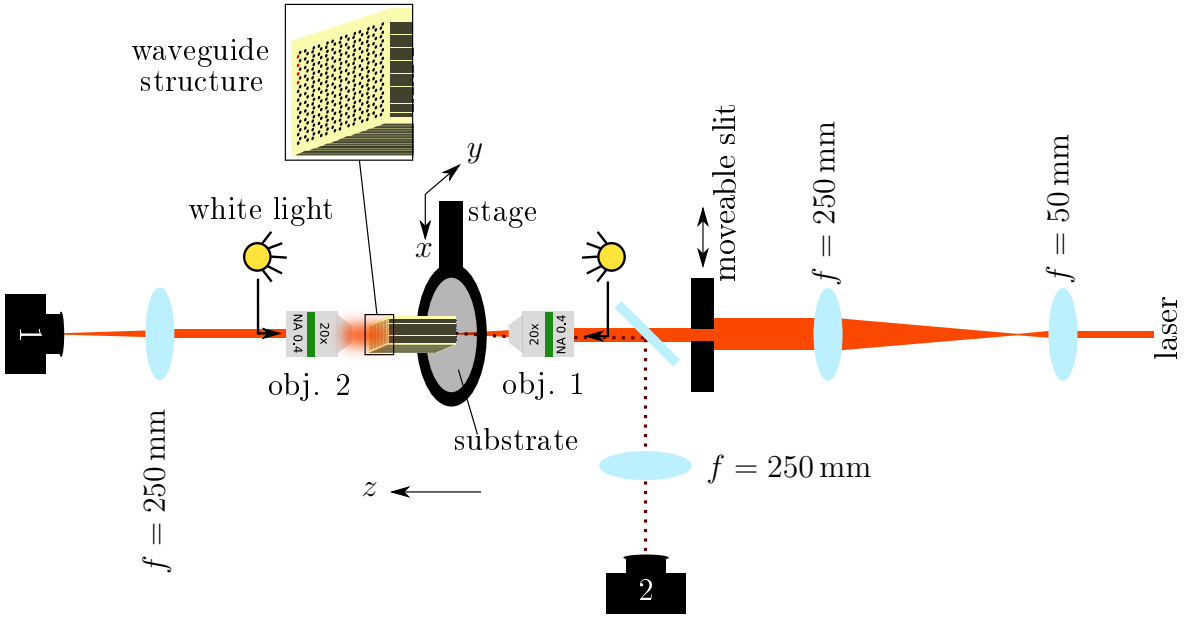

Figure 6.5: Sketch of the measurement setup. Adapted from [57] licensed under [38].

for each of the eight samples. As we can not look inside the sample, it is only possible to determine R and Z indirectly. The helix radius R is calculated from the product of the lateral shrinking of the sample and the value we designed R to have. The pitch Z shrinks by the same amount as the height h of the sample. Therefore, we can calculate Z from the fact that we used $h = 6.5Z$ for weak and $h = 5.5Z$ for strong defects. Here, only averaged values for each class of defects (weak or strong) are given. Slight differences between two samples in one class (e.g. straight strong defect and phase-shifted strong defect) might arise during fabrication. These are reflected in the given uncertainty values.

To excite a topological edge mode in the experiment the beam of a femtosecond-pulsed laser was expanded and sent through a movable slit in front of the first objective (see Fig. 6.5). By moving the slit, an angle in the in-coupling beam is created and thus a range around a certain $k_x\sqrt{3}a$ selected. We choose $k_x\sqrt{3}a \approx \pi$ to excite an edge mode at the lower zigzag edge, in front of the defect. The position of the excitation is indicated by the ellipse in Fig. 6.6 and 6.7. We then image the intensity at the sample's output facet, after the propagation distance $z = h$. The results are given in Fig. 6.6 and 6.7 for the case of weak and strong defects, respectively. The left columns show the measurements, compared to OptiBPM calculations in the right columns.

We first look at the known case of a missing waveguide. For both classes of defects we observe that the light moves around this missing waveguide. This shows that we are indeed in the regime of a topological insulator.

For the case of weak dynamic defects, the light mainly moves through the other types

of defect waveguides. In this regime, the time-averaged defect coupling constants do not differ too much from the usual coupling between bulk waveguides (maximum 15%, see Fig. 6.3 a)). It seems that the topological edge mode does not even notice them as defects.

This changes for the case of strong dynamic defects. Here, we observe that the edge mode partially moves around the defect, but also partially through it. However, the edge mode survives passing a defect in all of the observed cases. For the case of strong defects this is somehow surprising, as the waveguides overlap at some values of z. At certain z the coupling to next-nearest neighbors even exceeds the coupling to its nearest neighbors.

Our experimental observations are restricted to the output facet of the sample. In the analogy of Schrödinger and paraxial Helmholtz equation this corresponds to a certain time t only. To examine the behavior of the edge mode at different times experimentally, we would need to fabricate many sample with different heights. Another way would be to change the laser wavelength and thus the coupling constants, as was done in [42]. However, this has more implications on the band structure properties and, e.g., the relation to the defect frequency (see also section 6.2.4). Therefore, this method might lead to wrong conclusions regarding the effect of the dynamic defects on the edge mode. One further possibility is to move the input spot along the sample's edge [3]. Here, we are however restricted, as we want to keep a certain distance from the defect to make sure we excite the edge mode properly (and do not excite the defect). Furthermore, this way any population in the bulk is neglected that might accumulate over time. A more reliable approach here is to resort to numerical calculations. Figures 6.6 and 6.7 show that the numerical calculations match the measurements well. Therefore, we use OptiBPM for quantitative analysis of the robustness of edge transport.

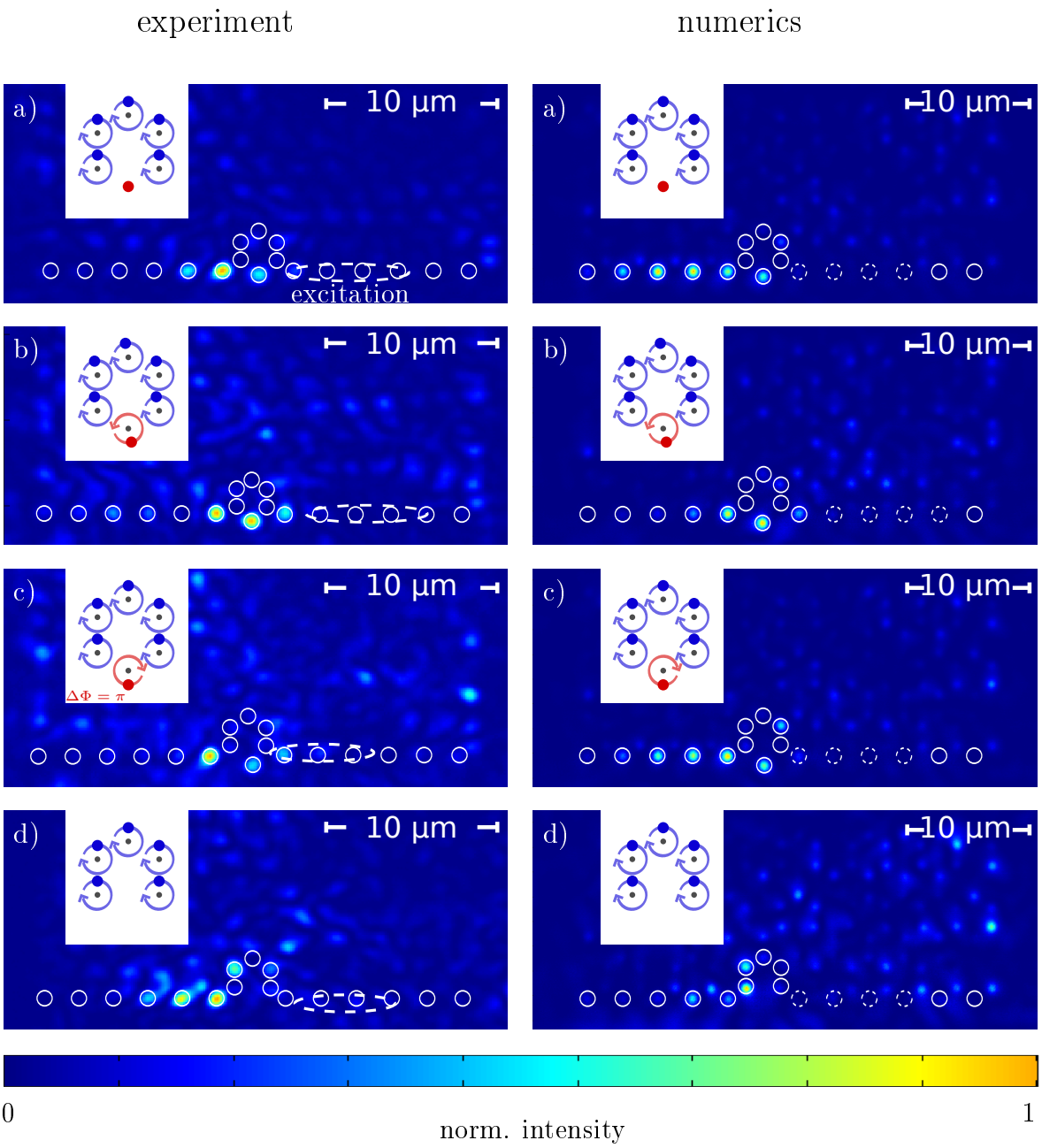

Figure 6.6: Weak dynamic defects: measured (left) and numeric (right, see section 6.1.2) intensity distributions at the output facet of the samples. The edge modes, excited at the location of the dashed ellipse, move around different kinds of defects: a) straight defect, b) defect with opposite helicity, c) defect shifted by half a helix pitch, d) missing waveguide. White circles indicate edge waveguides. Intensity is scaled to maximum separately for each image. The insets show the geometry at the defect. Output after $z = (471 \pm 38)\,\mu\text{m}$ (experiment) and $z = 468\,\mu\text{m}$ (numerics) of propagation. Taken from [57] licensed under [38].

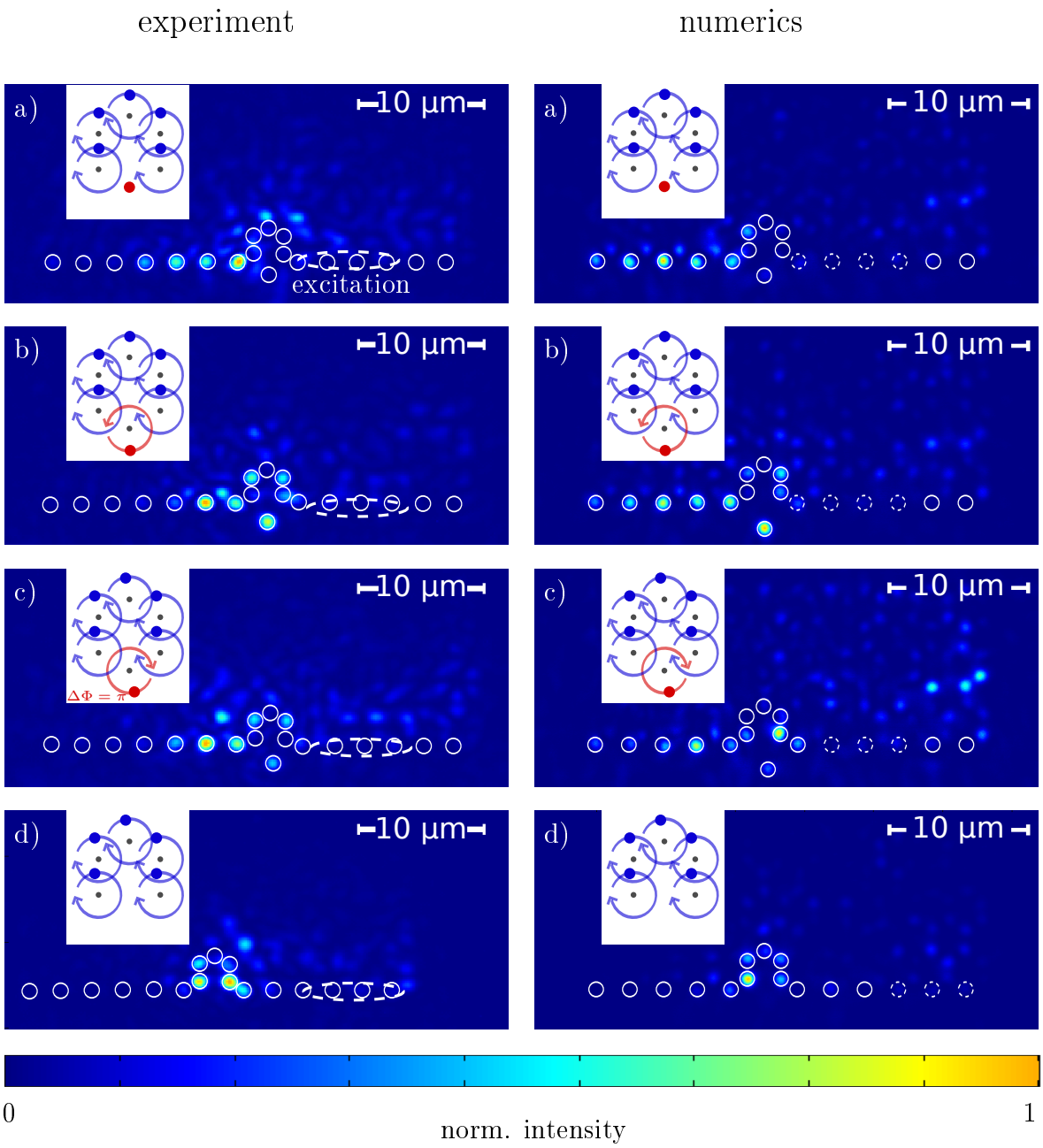

Figure 6.7: Strong dynamic defects: measured (left) and numeric (right, see section 6.1.2) intensity distributions at the output facet of the samples. The edge modes, excited at the location of the dashed ellipse, move around different kinds of defects: a) straight defect, b) defect with opposite helicity, c) defect shifted by half a helix pitch, d) missing waveguide. White circles indicate edge waveguides. Intensity is scaled to maximum separately for each image. The insets show the geometry at the defect. Output after $z = (465 \pm 15)\,\mu\text{m}$ (experiment) and $z = 467.5\,\mu\text{m}$ (numerics) of propagation. Taken from [57] licensed under [38].

6.1.2 Numerical calculations

Numerical calculations are done using OptiBPM (see section 3.3). Ten models are built to mirror the experimental waveguide arrays, five for each parameter regime (strong or weak defects). These five models consist of one system without defect for comparison, and each of the four defect cases, i.e. straight waveguide, waveguide with opposite helicity, with same helicity but phase-shifted, and missing waveguide. At the zigzag edge of the sample, three waveguides are excited by Gaussian beams with a phase difference of π, corresponding to $k_x\sqrt{3}a = \pi$. The input position, similar to the experiment, is several waveguides to the right of the defect, to ensure proper excitation of an edge mode.

Using the intensity distribution in the array's x-y-plane at different z-positions along propagation, a video is assembled for each model. These videos give a visual impression of the propagation of the edge mode and can be found in the supplemental material of [57]. They show some further interesting effects, that are not captured in the single experimental 'snapshots': Certain defects are able to retard part of the edge mode and thus split it into several packets, that later propagate along the edge separately. We observe this for the straight strong defect and the strong defect with opposite helicity. For the parameters used in the samples with weak defects, we observe severe intensity loss during propagation. This is due to bending losses. In these samples the losses are increased, as expected, due to the small helix pitch and larger wavelength of light. We therefore decrease the colorbar in the videos exponentially with the propagation distance z, for better visibility. In the case of weak defects this leads to the impression that a large proportion of intensity is in the bulk. Note however, that the maximal intensity scaling for large z is very low ($\approx 3 \cdot 10^{-3}$).

For quantitative analysis the intensity in the edge waveguides as well as in the bulk waveguides is summed up for each z-step and normalized to the intensity at the excitation point ($z = 0$). As mentioned, for some samples with defects, the edge mode partially moves through and partially around the defect (see videos and section 6.1.1). Therefore, also the waveguides immediately surrounding the defect are counted as edge waveguides in these cases. Waveguides considered as edge waveguides are indicated by white circles in Fig. 6.7. We note that edge modes are of course not strictly confined to these edge waveguides, but exponentially decay into the bulk. In the same vein, when coupling light into waveguides at the edge we will always also populate bulk modes to some amount. This is why the intensity in the bulk increases in about the first 100 µm of propagation (see Fig. 6.8 a) and 6.9 a)), even for the sample without defect. It is moreover not possible to thoroughly distinguish between light from edge and bulk modes in the same waveguide. Bulk modes are, however, spread over many waveguide sites. Hence, upon excitation at the edge, the light propagates inwards to the bulk and is diluted quickly. The edge modes, on the other hand, stay more strongly localized at the edge sites. Therefore, we claim that we make only a small error in counting the

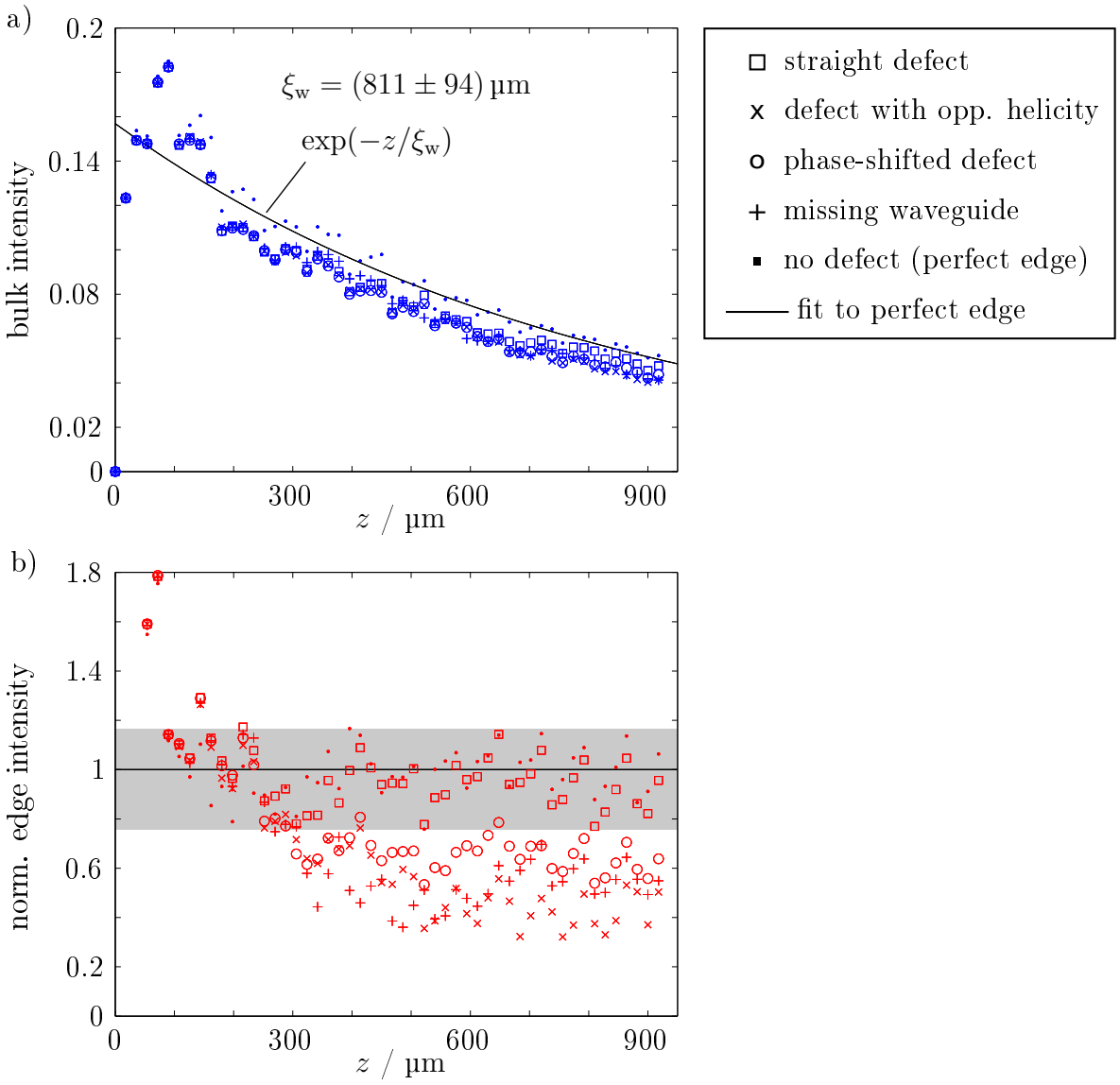

Figure 6.8: Numerical calculations for weak dynamic defects: Intensity in edge (red) and bulk (blue) for samples with and without defects. The edge intensity (b) is normalized to the fitting curve in (a) to remove overall losses. Taken from [57] licensed under [38].

intensity in the edge waveguides and inferring to the edge states from that.

The simulated situation corresponds to a scattering experiment: A wave-packet (excited at the three waveguides at $z = 0$) travels along the edge, meets the defect and interacts with it for a certain time interval ($100\,\mu m < z_{scatter} < 600\,\mu m$), and then moves on along the edge. To determine if the defect causes scattering into the bulk, we examine the intensity in the edge and in the bulk waveguides. We need to look at both intensities, as we have to distinguish between two effects: scattering into the bulk, and losses into the continuum induced by the defect. In addition to that, overall losses are present in our system. These are mainly absorption and bending losses and lead to an

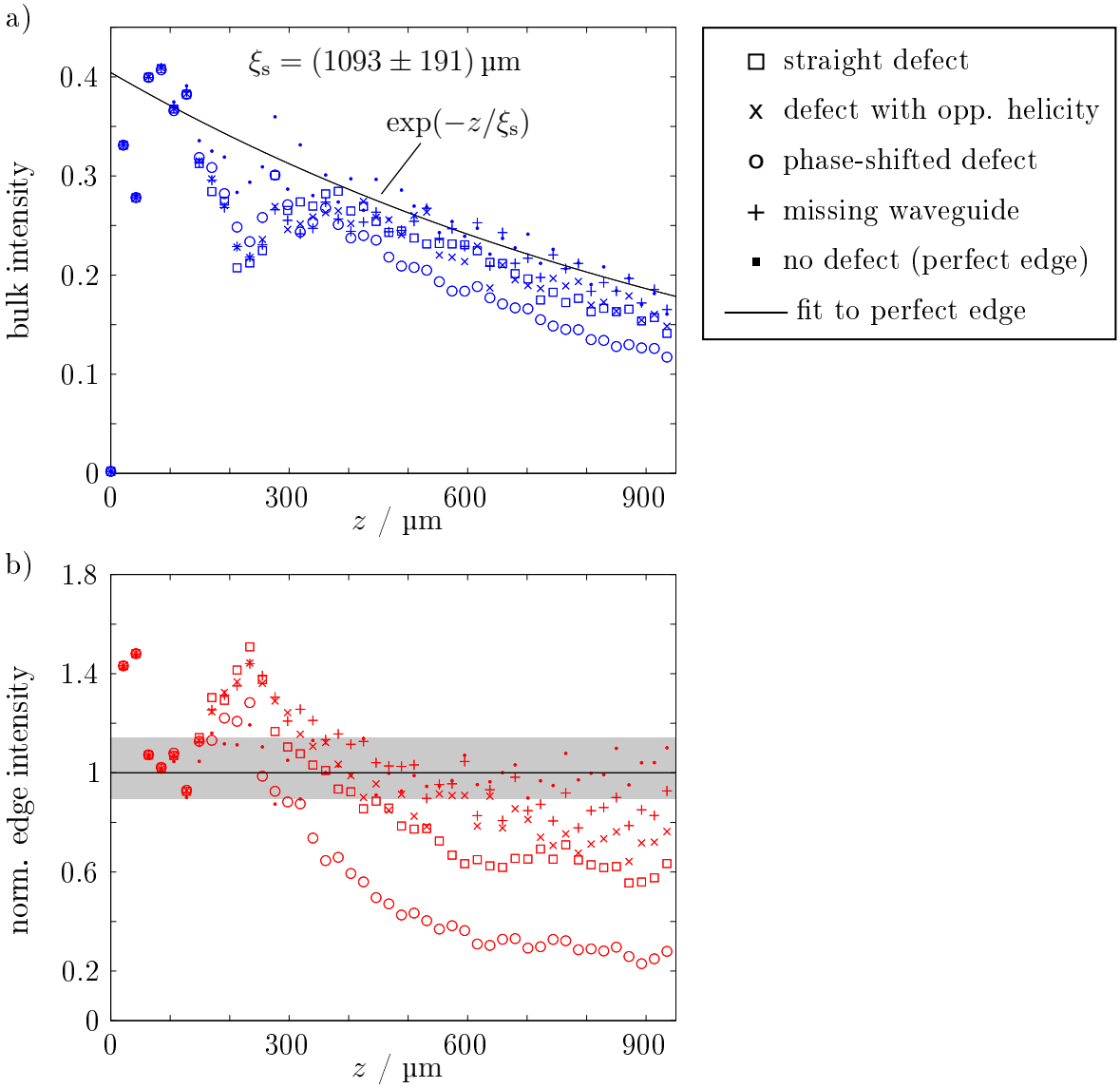

Figure 6.9: Numerical calculations for strong dynamic defects: Intensity in edge (red) and bulk (blue) for samples with and without defects. The edge intensity (b) is normalized to the fitting curve in (a) to remove overall losses. Taken from [57] licensed under [38].

exponential decay of the intensities (compare for Fig. 6.8 a) and 6.9 a)). To separate these overall losses from the dynamics, we fit an exponential decay to the curves of the defect-free sample (perfect edge) for $z \gg z_{\text{scatter}}$, where the influence of the defect is negligible. The edge intensities in Fig. 6.8 b) and 6.9 b) are then normalized to the respective fit. The grey shading indicates the intensity range for the defect-free sample. We assume that intensity, that is radiated off due to bending, is picked up by neighboring waveguides and thus leads to fluctuations of the data. Figures 6.8 and 6.9 show two things: First, the exponential decay rate for $z \gg z_{\text{scatter}}$ is not influenced by any of the examined defects, as one would expect. This means, that the normalized curves are approximately constant for $z \gg z_{\text{scatter}}$. Second, the defects do not lead to

scattering into the bulk, but only to losses into the continuum. Figures 6.8 a) and 6.9 a) show, that the intensity in the bulk does not rise above the value for the defect-free sample. The drop in the intensity in the edge therefore has to be interpreted as loss into the continuum. This drop is most prominent for the sample with the phase-shifted and with the straight strong dynamic defect (Fig. 6.9 b)). Considering both the bulk and edge intensity indicates, that rather than scattering into the bulk, the intensity is radiated away. This can be explained by mode mismatching, as the phase-shifted and the straight defect are overlapping with their neighbors at certain z.

The numerical calculations using OptiBPM show no increased scattering into the bulk. Therefore, both experiment and numerical calculation indicate that the edge mode is still robust in the presence of the examined time-dependent defects. This is somehow surprising, as time-dependency violates the energy conservation of the system and could lead to a coupling to bulk states. However, all of the defects considered in this section share the periodicity of the bulk waveguides. Coupling between edge and bulk states should be possible, if the defect has the 'right' quasi-energy to conciliate between edge and bulk modes. We want to examine rigorously, how we have to choose amplitude and period of the driving to obtain such coupling. To do so, we resort to an analytically simpler model, the one-dimensional SSH model, in the next section.

6.2 Limits of topological protection (in 1D)

The work presented in this chapter was done in collaboration with Zlata Feodorova (Universität Bonn), Christoph Dauer and Fabian Letscher (TU Kaiserslautern) and published in [153]. Z. Feodorova performed complimentary experiments in plasmonic waveguides. C. Dauer developed the Floquet analysis. F. Letscher contributed to the theoretical understanding of the effects.

We want to understand how we have to design a time-dependent defect, such that the topological protection of an edge state is destroyed, i.e., the edge state couples to bulk states. To do so, we look at a one-dimensional topological system with only one timescale, the SSH model with local driving.

6.2.1 SSH model

The SSH-model — named after its discoverers Su, Schrieffer and Heeger [11] — provides us with a one-dimensional topologically non-trivial system. It consists of dimers of sites, where the sites are alternately coupled via a strong bond J_1 and a weak bond J_2. As there are two sites in one unit cell, its band structure consists of two bands. They are separated by a band gap of size $2|J_1 - J_2|$, and have a maximum absolute energy of $|J_1 + J_2|$ (see Fig. 6.10 i)). Depending on the choice of the unit cell, the chain exhibits trivial or non-trivial topology, indicated by a topological invariant, the Zak phase. The Zak phase corresponds to the Berry-phase in a 1D lattice [154]. Zak realized that in 1D lattices this phase can only take the values of 0 and π if inversion symmetry is present in the system.

Non-trivial topology exists in chains that have a non-zero Zak phase. In the SSH model these are chains that are terminated with a weakly bound site. In the non-trivial case there exists an edge state. As the edge state has dimension zero, it is exponentially localized around the terminating site. The localization length, i.e., the exponential decay constant, depends on the energetic distance between the edge state and the bulk bands and thus on the gap size (the closer the edge band to the bulk band, the larger the localization length). Chiral symmetry ensures that this edge state lies at zero energy in the band gap of the bulk band structure and occupies only every second lattice site [95].

Interfacing two chains, one with trivial and one with non-trivial topology, creates a domain wall. We enumerate the sites in the chain such, that the location of the interface is at site 0 (see, e.g., Fig. 6.11). There, also an edge state exists, that is exponentially localized around this site. This is also reflected by the bulk-boundary correspondence, as the Zak phases between the two chains differ by π relative to each

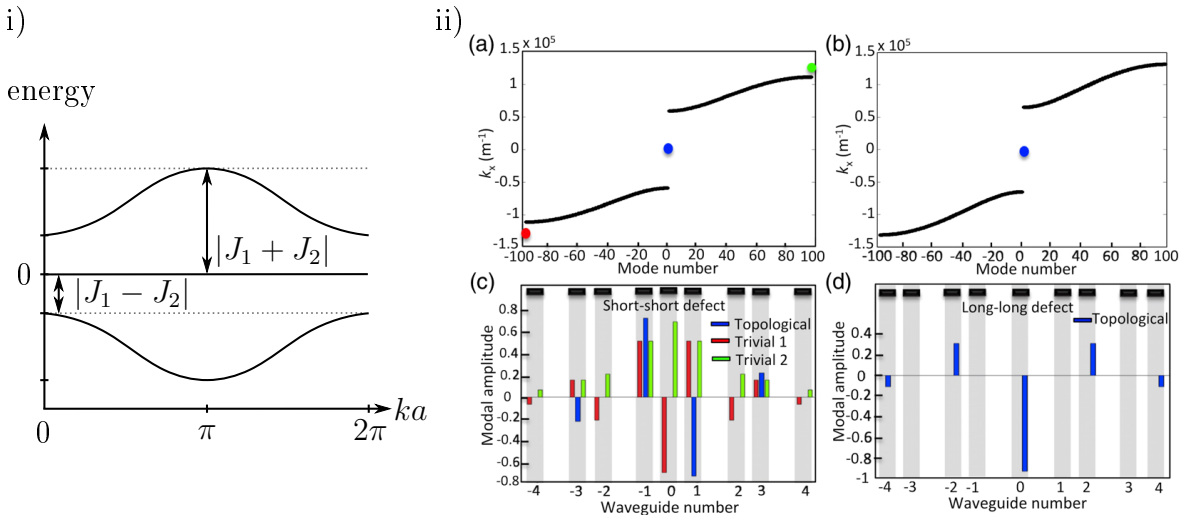

Figure 6.10: i) Band structure of the SSH model with the edge state at zero energy. Here, $a = d_1 + d_2$. ii) Short-short (a,c) and long-long (b,d) defect with corresponding modal amplitudes (c,d). Taken from [42].

other. Interfacing these two different chains can be done in two possible configurations (see Fig. 6.10 ii)): Firstly, we can create a weak-weak domain wall (i.e. J_2 is repeated twice). In the waveguide picture this is also called a long-long defect, as the large distance is repeated twice. Remember that $J \propto \exp(-d)$ where d is the distance between waveguides. In this configuration, one topologically non-trivial edge state at energy $E = 0$ exists. In real-space, its wave function is mirror symmetric around the domain wall. The second configuration is a strong-strong defect, i.e., J_1 is repeated twice. This corresponds to a short-short defect in the waveguide picture, as the spacing from the defect to its neighbors corresponds to the short distance on both sides. This arrangement gives rise to one topologically non-trivial state at $E = 0$, with a wave function that is point symmetric around the defect. Furthermore, two trivial defect states exist. Energetically, they lie above and below the bulk band structure. In real-space, their wave functions occupy each lattice site, in contrast to the topologically non-trivial state [42]. In order to only excite the topological edge state when we couple light into site 0, we will use a chain with a long-long defect.

6.2.2 Modulation of the defect

We now want to see, if the modulation of the defect in this system leads to coupling of the edge state to bulk states. Therefore, we drive the system locally. We modulate the position of the waveguide at site 0 either in the x- or y-direction, by bending the waveguide sinusoidally (see Fig. 6.11). This results in time-dependent hoppings $J_{-1,0}$ and $J_{0,1}$ between site 0 and its neighbors. Thus our Hamiltonian becomes time-dependent. However, this does not change the topological properties of our system.

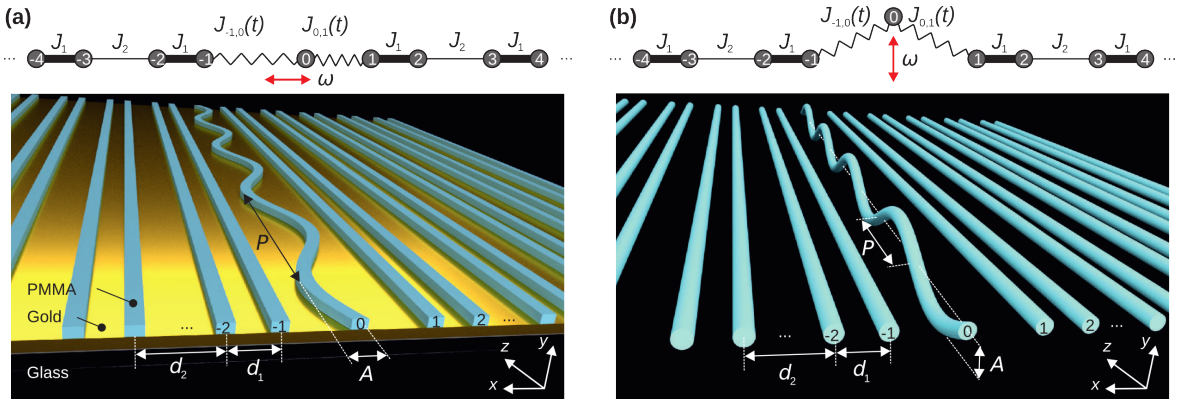

Figure 6.11: Sketch of the two experimental systems. a) Implementation of the in-plane modulation using surface plasmon polaritons by Z. Feodorova. b) Implementation of the out-of-plane modulation in the DLW dielectric waveguides done in this thesis. A is the maximum deflection of the 0th waveguide. Note that in b) the period of modulation P is defined to be half the waveguide period. As the distance between the defect and its neighbors is the same whether the waveguide bends up or down, the couplings vary with twice the waveguide period. Adapted from [153] licensed under [155].

The topological invariants are properties of the global system, i.e., of the bulk of the system, and cannot change under local transformations. Therefore, the system is still topologically invariant.

6.2.3 Floquet analysis

To treat the problem of our time-dependent Hamiltonian analytically, we use the Floquet theory described in section 2.5. Note that we do not want to derive an effective Hamiltonian of our system, that is projected onto a subspace of $\mathbb{H}$ (compare for section 2.6). Instead, our Floquet Hamiltonian is an element of the extended Hilbert space $\mathbb{H} \otimes \mathbb{T}$. This means that we do not restrict the band structure to one Floquet Brillouin zone, and the energy axis we will use is not periodic.

To obtain the term $H^{(m)}$ (see Eq. (2.51)) that couples different Floquet orders, we have to look at the Hamiltonian of our specific system

$$H = H^{(0)} + H_{\mathrm{P}}(t). \tag{6.7}$$

It consists of a time-independent part $H^{(0)}$ and a time-periodic part $H_{\mathrm{P}}(t)$, where

$$\begin{aligned} H^{(0)} = &\sum_{s=-M+1}^{0} (J_1\ \hat{a}_{2s-2}^{\dagger}\hat{a}_{2s-1} + J_2\ \hat{a}_{2s-1}^{\dagger}\hat{a}_{2s}) \\ &+ \sum_{s=0}^{M-1} (J_2\ \hat{a}_{2s}^{\dagger}\hat{a}_{2s+1} + J_1\ \hat{a}_{2s+1}^{\dagger}\hat{a}_{2s+2}) \\ &+ \mathrm{h.c.} - \Delta V\ \hat{a}_0^{\dagger}\hat{a}_0 \end{aligned} \tag{6.8}$$

describes the static interfaced SSH-chains.

$$H_{\mathrm{P}}(t) = (J_{-1,0}(t) - J_2)\hat{a}_0^{\dagger}\hat{a}_{-1} + (J_{0,1}(t) - J_2)\ \hat{a}_0^{\dagger}\hat{a}_1 + \mathrm{h.c.} + \Delta V \cos(\omega t)\ \hat{a}_0^{\dagger}\hat{a}_0 \tag{6.9}$$

is the time-dependent part that arises due to the modulation of the defect. The additional on-site potential $V(t) = -\Delta V + \Delta V \cos(\omega t)$ at site 0 results from a change in the effective refractive index due to the curvature of the modulated waveguide [156]. ΔV was calculated by Fabian Letscher to be

$$\Delta V = r_{\mathrm{wg}} \frac{2\pi}{\lambda} n_{\mathrm{wg}} A \left(\frac{\omega}{2}\right)^2 \tag{6.10}$$

with the maximum deflection of the waveguide A, and shifts the energy of the edge state by the amount of ΔV. The Hamiltonians are described by $(4M+1) \times (4M+1)$ matrices, connecting the $4M+1$ lattice sites with M dimers in either side chain and the defect in the middle.

We Fourier-decompose the time-periodic Hamiltonian and its Floquet modes in time. Inserting both into the Schrödinger equation, yields a set of coupled equations (see Eq. (2.51)). To calculate the specific Floquet coupling term $H^{(m)}$ therein in our model, we have to look at the time-dependent hoppings and on-site potential. As the hopping J decays exponentially with the center-to-center distance between waveguides[(2)], the time-dependent hopping is

$$J_{-1,0}(t) = J_{0,1}(t) = p_1 \exp\left(-p_2 \sqrt{d_2^2 + \frac{A^2}{2}(1 - \cos(\omega t))}\right) \tag{6.11}$$

for out-of-plane modulation and

$$J_{-1,0}(t) = p_1 \exp\left(-p_2(d_2 + A\sin(\omega t))\right), \tag{6.12a}$$

$$J_{0,1}(t) = p_1 \exp\left(-p_2(d_2 - A\sin(\omega t))\right), \tag{6.12b}$$

for in-plane modulation. The parameters p_1 and p_2 depend on the specifics of the

(2) for non-overlapping waveguides, as is the case in this section

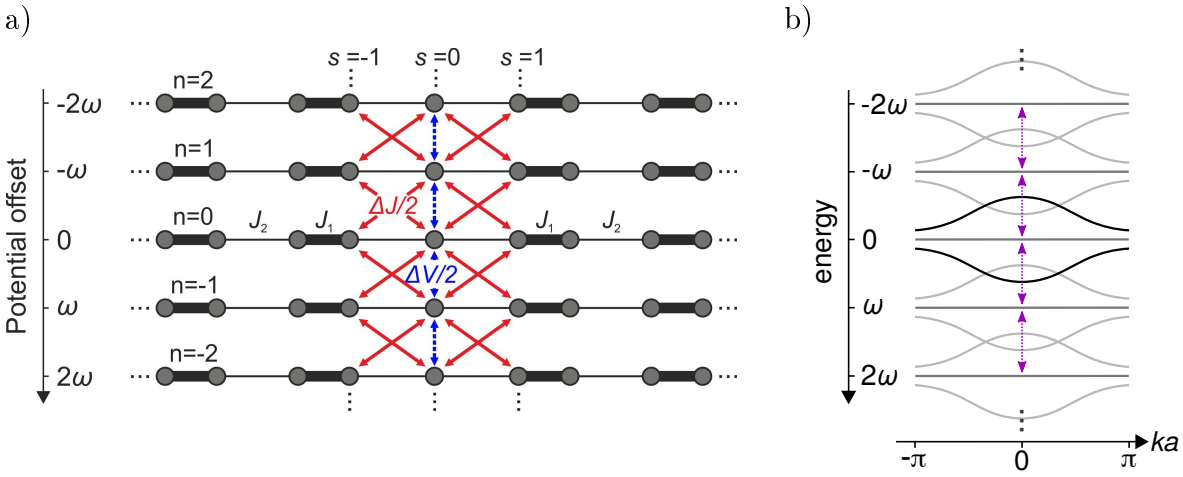

Figure 6.12: Graphical representation of the Floquet terms. a) Real-space display of the copies of $H^{(0)}$ with global on-site potentials $n\omega$. Different Floquet replicas are coupled with $\Delta V/2$ and $\Delta J/2$, where ΔV is the amplitude of the periodically changing on-site potential at site 0 and ΔJ is the amplitude of modulation in the coupling. Taken from [153] licensed under [155]. b) Sketching the band structure, shows a stack of the static band structure, where mainly the replicas of the edge state are coupled along the Floquet dimension. The copies of the bulk bands are only shown as guide to the eye (see also comment below).

sample (i.e. refractive index contrast, wavelength of light used, etc.). We approximate the time-dependent hopping by a sinusoidal function in both cases, for easier analytic treatment:

$$J_{-1,0}(t) = J_2 + \Delta J \sin(\omega t + \phi_1)\,, \tag{6.13a}$$

$$J_{0,1}(t) = J_2 + \Delta J \sin(\omega t + \phi_2)\,. \tag{6.13b}$$

ϕ_1 and ϕ_2 are phases and are $\phi_1 = 0$ and $\phi_2 = \pi$ for in-plane modulation and $\phi_1 = \phi_2 = \pi/2$ for out-of-plane modulation. ΔJ is the amplitude of the modulation in the coupling. The on-site potential also varies sinusoidally as

$$V_0(t) = -\Delta V + \Delta V \cos(\omega t)\,. \tag{6.14}$$

Fourier-decomposition with Eq. (2.50) of $H_{\mathrm{P}}(t)$ then yields only $H^{(\pm 1)}$ components:

$$H^{(\pm 1)} = \mp\frac{1}{2}\begin{pmatrix} \ddots & & & & & & & & \\ & 0 & & & & & & & \\ & & 0 & & i\Delta J\exp(\mp \mathrm{i}\phi_1) & & 0 & & \\ & & i\Delta J\exp(\mp \mathrm{i}\phi_1) & & \mp\Delta V & & i\Delta J\exp(\mp \mathrm{i}\phi_2) & & \\ & & 0 & & i\Delta J\exp(\mp \mathrm{i}\phi_2) & & 0 & & \\ & & & & & & & 0 & \\ & & & & & & & & \ddots \end{pmatrix}. \tag{6.15}$$

Fig. 6.12 gives a graphical representation of the Floquet system. It sketches copies of $H^{(0)}$ spaced with ω, which means that each copy of $H^{(0)}$ has a global on-site potential of $n\omega$. Different Floquet replicas at site 0 are coupled with $\Delta V/2$, corresponding to the amplitude ΔV of the periodically changing on-site potential at site 0. Furthermore, site 0 in Floquet replica n is coupled to sites +1/-1 in Floquet replicas $n+1$ / $n-1$ with $\Delta J/2$ and vice versa. The coupling between different sites at different Floquet orders therefore depends on the amplitude of modulation in the coupling. Remember that we only apply the modulation locally, and do not drive the complete system, as was done in [149]. There, the modulation of the bulk led to couplings between bulk sites of different Floquet orders, which opened new gaps in the spectrum and changed the topology of the system. This cannot happen in our system, as the bulk is kept static.

Looking at Fig. 6.13 we see that we obtain mainly three different regimes:
1) The driving frequency is larger than the band width $\omega > |J_1 + J_2|$. This means that the Floquet replicas of the edge state lie outside the energy range of the bulk band structure. No coupling can occur, and the population of the edge state stays constant over time.
2) For driving frequencies $|J_1 - J_2| < \omega < |J_1 + J_2|$ in the energetic range of the bulk bands, coupling between edge and bulk states occurs. The initial population of the edge state decreases exponentially, as it is transferred into the bulk. This is due to hybridization between edge and bulk states. The population transfers from the 0th order edge state to the replicas (compare for Fig. 6.12), and from them to the bulk. In the band structure this displays as a depopulated edge state and a Lorentzian shape of the original line of the edge state (exponential decay in real-space leads to a Lorentzian shape in k-space).
3) Driving frequencies $\omega < |J_1 - J_2|$ imply that the first ($n = \pm 1$) order Floquet replicas lie inside the band gap. Coupling from bulk to edge states is still possible through higher order replicas, but much weaker.

For a more rigorous treatment, we would need to add higher order components depend-

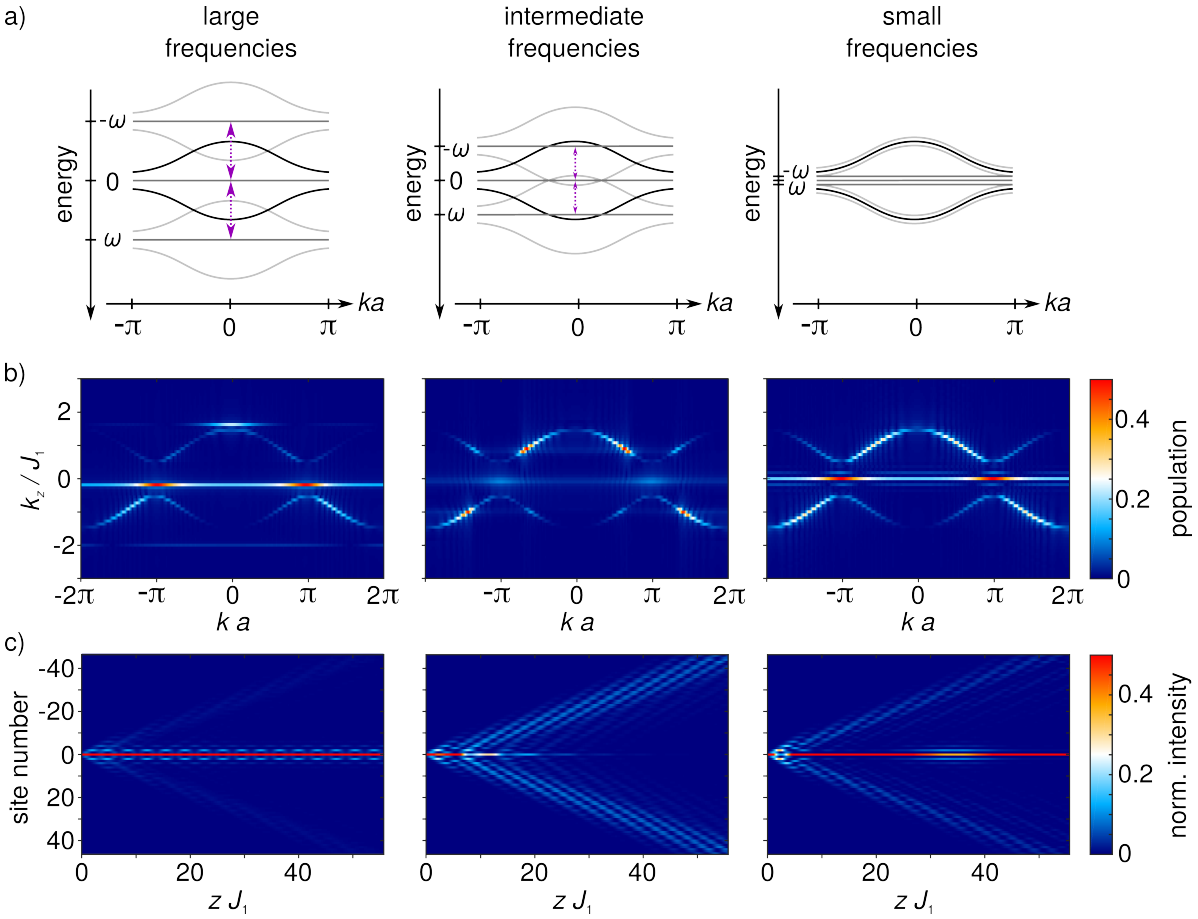

Figure 6.13: The three different regimes of defect driving. a) Sketch of the band structure, b) population of the states in the band structure calculated numerically by Fourier transformation of c). c) Real-space propagation of the light in the waveguide system along z or time zJ_1, calculated by numerically solving the time-dependent Schrödinger equation with the time-dependent tight-binding Hamiltonian, including the modulation in the coupling and on-site potential of the defect. At $zJ_1 = 0$ only the waveguide at site 0 is excited. For frequencies larger than the band width (left column) the Floquet replicas of the edge state lie outside the static bulk bands. Coupling between edge and bulk states takes place for frequencies in the energetic range of the bulk bands (middle column). The edge state is depopulated and light is transferred into the bulk. For frequencies smaller than the band gap, the light mainly stays localized in the defect site (right column).

ing on the amplitude of the modulation. In the following, we will restrict the analysis to the out-of-plane modulation. To see the weight of the higher orders of $H^{(m)}$ we calculate the Fourier components of the hopping, $J^{(n)}$, by Fourier decomposition:

$$J^{(n)} = 1/T \int_0^T J_{0,1}(t) \exp(-in\omega t) dt \tag{6.16}$$

It should be noted that there is also an additional component from $H^{(0)}$ that shifts the original J_2, such that the average value of $J_{0,1}$ is smaller than J_2. Fig. 6.14 shows

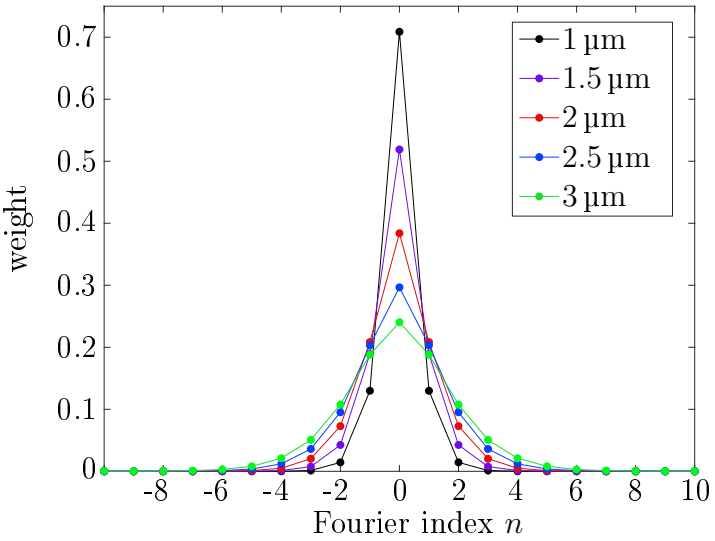

Figure 6.14: The weight of the Fourier components of $J_{0,1}(t)$ for out-of-plane modulation (compare Eq. (6.16)). Colors indicate the deflection A of the waveguide. With increasing A the higher order components gain more weight.

the weight of the Floquet components $J^{(n)}$ in dependence on the waveguide deflection A (color coded), which translates into the driving amplitude. We see that the higher order components with $|n| > 1$ gain more weight with increasing deflection. That means that also coupling of higher order Floquet sidebands with the bulk are possible for large enough amplitudes. These couplings correspond to 'multi-photon' processes. For driving frequencies smaller than the bandgap, depopulation of the edge state will always occur due to these higher order sidebands, but in timescales that can be very large, depending on the amplitude of the driving.

Note that, although sketched in Fig. 6.12 b), there are no Floquet copies of the bulk, as the bulk is not modulated. We can see that from a purely photonic argument: The modulation of the defect makes additional propagation constants in the defect become possible. In the bulk, however, only the propagation constants of the static bulk exist. As we associate propagation constants with energies, this means that also higher energetic bulk band copies cannot exist. This is why we get no 'direct' depopulation of the 0th Floquet order edge state into a higher Floquet order bulk replica. Direct depopulation would be visible as increased population in the k-region of the bulk replica at zero energy.

In the corresponding paper [153], we also showed the decay rates for the depopulation of the edge state, calculated by C. Dauer. He obtained them by numerically calculating the Floquet eigenstates $|\Psi(t)\rangle$, and fitting the overlap of these with the initial condition $|\Psi(t=0)\rangle = |E=0\rangle$ (where $|E=0\rangle$ is the state with zero energy) by

$$|\langle E=0|\Psi(t)\rangle|^2 \approx (1-c)\exp(-\Gamma t) + c. \tag{6.17}$$

Additionally, he compared them to decay rates obtained by Fermi's golden rule. The results are shown in Fig. 6.15. We see that the decay rates are largest for frequencies

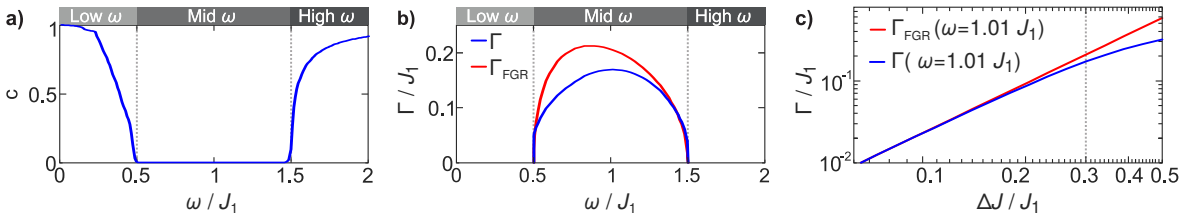

Figure 6.15: a) Fitting parameter c (see Eq. (6.17)) over driving frequency ω. b) Decay rates Γ for intermediate frequencies calculated numerically (blue) and by Fermi's golden rule (red) for $\Delta J = 0.3J_1$. c) Decay rate at fixed frequency $\omega = 1.01J_1$ in dependence on ΔJ. The dashed line highlights the experimentally relevant value of $\Delta J = 0.3J_1$. Adapted from [153] licensed under [155].

around $\omega = 1J_1$ (Fig. 6.15 b)) and tend to zero in the high and low frequency regime, as expected (Fig. 6.15 a)). They also agree qualitatively with Fermi's golden rule for small amplitudes in the hopping modulation (Fig. 6.15 c)).

6.2.4 Experiments

We now want to verify the calculations by experimental measurements. The experiments were done in two complementary systems (see Fig. 6.11):

1) The model with in-plane modulation, where the defect is modulated in the x-direction, was implemented by Z. Feodorova in the group of Prof. Linden (Universität Bonn) [153] in a plasmonic waveguide system. There, the leakage radiation of the surface plasmon polaritons allows to capture both real-space and Fourier-space [41]. Thus, the population in the band structure can be imaged. Fig. 6.16 reveals the location of the edge state's Floquet replicas in the Fourier-space measurements, in nice agreement with the theoretical predictions. For more details about these experiments see [153].

2) The out-of-plane modulation (in y-direction) of the defect was implemented in the dielectric waveguides. The inverse structure was fabricated by direct laser writing and infiltrated with *SU8* (see section 3.1). Several samples with SSH chains, each containing a long-long defect at site 0 with different period of modulation P, were made. For a SEM image of one of the samples with five chains see Fig. 6.17. Here, the distance between the defect and its neighbors is the same whether the waveguide bends up or down (see Fig. 6.11). This means that the defect couplings $J_{-1,0} = J_{0,1}$ (see Eq. (6.11)) vary with twice the waveguide period, as well as the on-site potential modulation V_0. Therefore, we define the period of modulation P to be half the waveguide period. The common parameters for all samples were the waveguide radius $r = (0.52 \pm 0.03)\,\mu\text{m}$, short center-to center distance between waveguides $d_1 = (1.42 \pm 0.02)\,\mu\text{m}$ corresponding to the strong hopping J_1, and long distance $d_2 = (1.69 \pm 0.01)\,\mu\text{m}$ corresponding to J_2. These parameters were chosen such that, in the wavelength range from

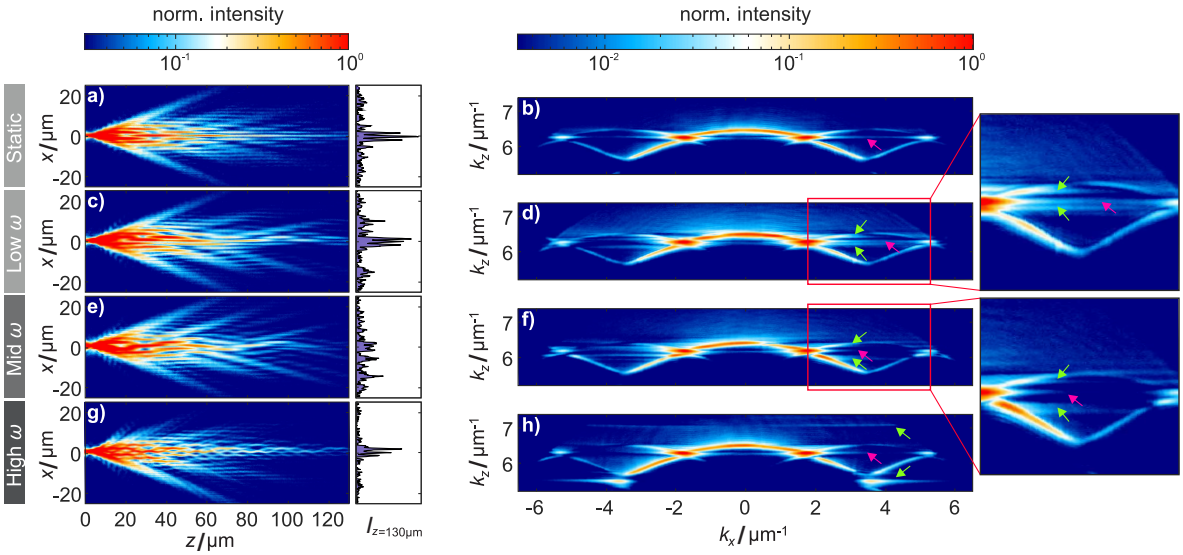

Figure 6.16: Real-space (left) and Fourier-space measurements (right) of the system with in-plane modulation. Implementation and measurements were done by Z. Feodorova in surface plasmon polariton waveguides. The Fourier-space measurements show the location of the edge state's ±1st Floquet replicas (green arrows) and 0th order edge state (red arrow). Adapted from [153] licensed under [155].

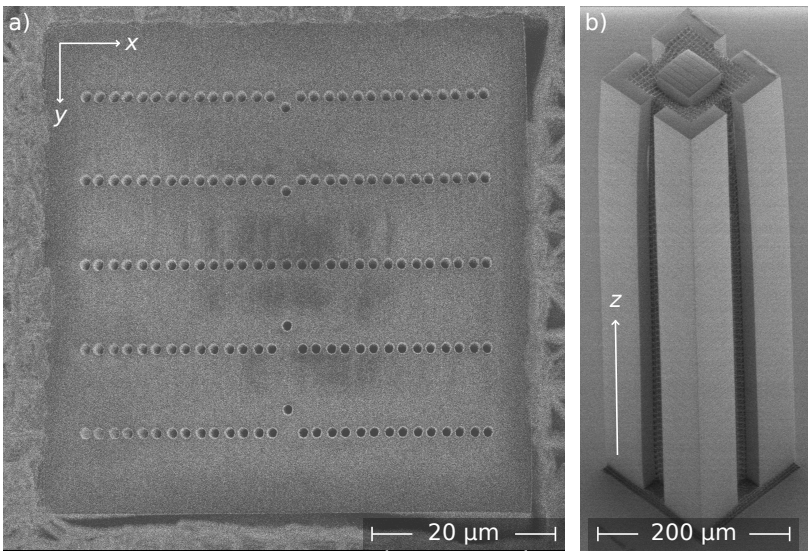

Figure 6.17: SEM image of a dielectric waveguide sample: a) top view, b) side view (tilted by 42°). The sample contains five rows of SSH chains with a long-long defect in the center. The defects have different modulation frequencies ω (period P). The central y-position of the defects lies in line with the SSH chain, although a different impression arises at the image taken of the output facet (a), as the defects are each deflected differently at this z -position due to their different pitch. Adapted from [153] licensed under [155].

$\lambda = 680\,\text{nm}$ to $835\,\text{nm}$, the relation between the weak and strong hopping was around $J_2/J_1 \approx 0.5$ (more exact: between 0.48 and 0.57). This leads to a total band gap of size $2|J_1 - J_2| \approx 2 \cdot 0.5 J_1$ and a total band width of $2|J_1 + J_2| \approx 2 \cdot 1.5 J_1$.

To conduct the measurements, the beam from a tunable white light laser (*SuperK EVO, NKT photonics*) was sent through a *VARIA* (*NKT photonics*) filter box to select a certain wavelength (bandwidth 10 nm). The beam was then expanded and focused through an objective (*Zeiss*, NA 0.4, 20x) into the defect waveguide at site 0 at the input facet. We observed the intensity distribution in the sample at the opposite output facet by imaging it through an identical objective and a lens onto the CMOS-camera 1, as shown in Fig. 3.6. This corresponds to a propagation length of $h = 833\,\mu\text{m}$ in z or about 24 hops with J_1. As we cannot capture the electric field from the side of the sample, only the intensity in real-space at the output facet is accessible.

Figure 6.18 a) shows the intensity distribution at the output facet in five SSH chains with a defect with different waveguide period $2P$, where $2P = (979.0 \pm 1.4)\,\mu\text{m}$, $(783.0 \pm 1.1)\,\mu\text{m}$, $(588.0 \pm 1.1)\,\mu\text{m}$, $(392.0 \pm 0.6)\,\mu\text{m}$, and $(200.0 \pm 0.3)\,\mu\text{m}$), respectively. The waveguide's maximum deflection was $A = (1.36 \pm 0.04)\,\mu\text{m}$. This means that $J_{0,1}$ varied from $0.48 J_1$ to $0.13 J_1$, according to Eq. (6.11).

We see that for modulation pitches corresponding to $0.5 \leq \omega/J_1 \leq 1.5$ (highlighted in red in Fig. 6.18) light propagates into the bulk waveguides, while for frequencies outside this range light is localized in the defect. The same was observed for measurements on the plasmonic samples by Zlata Feodorova [153]. This agrees well with the theory, as in this range, the energies of the bulk coincide with that of the $\pm$1st Floquet copies of the edge. Then, the edge state hybridizes with the bulk states, and is depopulated into the bulk. Outside the frequency range, edge and bulk states cannot couple and the light stays localized.

To exclude fabricational deviations, we repeated the measurement on just one sample of an SSH chain with a fixed period of the defect $2P = (302.0 \pm 0.2)\,\mu\text{m}$ and $A = (2.63 \pm 0.08)\,\mu\text{m}$. To tune through the modulation frequency, we changed the wavelength of light, used for the measurement. This corresponds to changing the couplings, as they are dependent on the wavelength. Therefore, the ratio ω/J_1 changes. Note that here, also the variation of $J_{0,1}$ depends on the wavelength: its maximum and minimum values in time (according to Eq. (6.11)) are $0.47 J_1$ and $0.01 J_1$ respectively for $\lambda = 680\,\text{nm}$, $0.48 J_1$ and $0.01 J_1$ (710 nm), $0.52 J_1$ and $0.02 J_1$ (750 nm), $0.53 J_1$ and $0.02 J_1$ (780 nm), and $0.55 J_1$ and $0.03 J_1$ (810 nm).

The results are shown in Fig. 6.18 b). We see that the light is localized for $\omega \geq 1.5 J_1$. If we compare the numerically calculated band structures in Fig. 6.19 we can also see that the on-site potential is not negligible anymore for these size of frequencies. The on-site potential shifts the energy of the edge state by the amount ΔV (compare for Eq. (6.10)). Due to this shift, one of the replicas hits the bulk bands a bit earlier

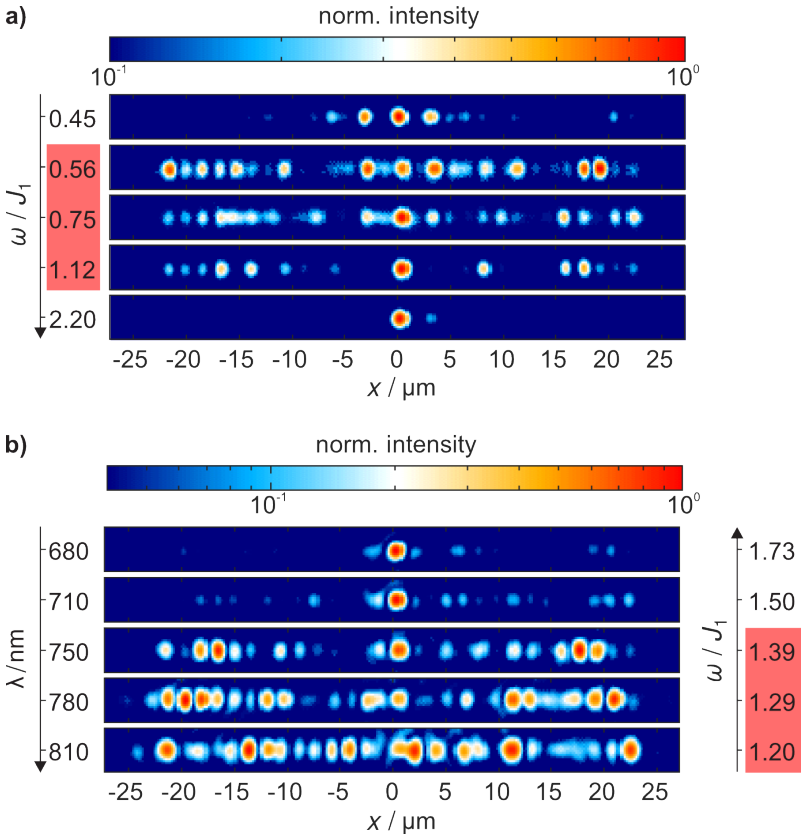

Figure 6.18: Measurements in 3D printed dielectric waveguides for out-of-plane modulation of the defect. Shown are the intensities in the waveguides at the output facet. (a) Measurements for several structures with different waveguide period (frequency of modulation ω) with otherwise the same parameters, at a fixed wavelength of light $\lambda = 710\,\text{nm}$. For small frequencies, the light is localized around the defect (at $x = 0$). When the frequency is increased to $0.56 \leq \omega/J_1 \leq 1.12$ (highlighted in red), light couples to the bulk states. It localizes in the defect again for large frequencies. (b) In a structure with a fixed period of the defect modulation the wavelength is tuned, which corresponds to changing the ratio ω/J_1. Light is delocalized/couples to the bulk, when the first Floquet mode hits the bulk band, starting at $\lambda = 750\,\text{nm}$. Note that the ratio J_2/J_1 changes with the wavelength: $J_2/J_1 = 0.47$ at $\lambda = 680\,\text{nm}$, 0.48 (710 nm), 0.52 (750 nm), 0.53 (780 nm) and 0.55 (810 nm). Adapted from [153] licensed under [155].

than the other. Thus, the range of frequencies ω, for which coupling to bulk states is possible, becomes larger. However, as can be seen in Fig. 6.19 even for $\omega = 2.2J_1$, ΔV is still smaller than the bandgap, and ω is so large that the first Floquet replicas lie well outside the bulk bands. For the measurements in Fig. 6.18 b), $\Delta V < \Delta J$ is valid for all wavelengths used. Therefore, the on-site potential does not change the overall picture qualitatively.

In conclusion, we see that the topological protection of an edge state against scattering to the bulk is destroyed in the presence of driven defects, if the frequency is such that

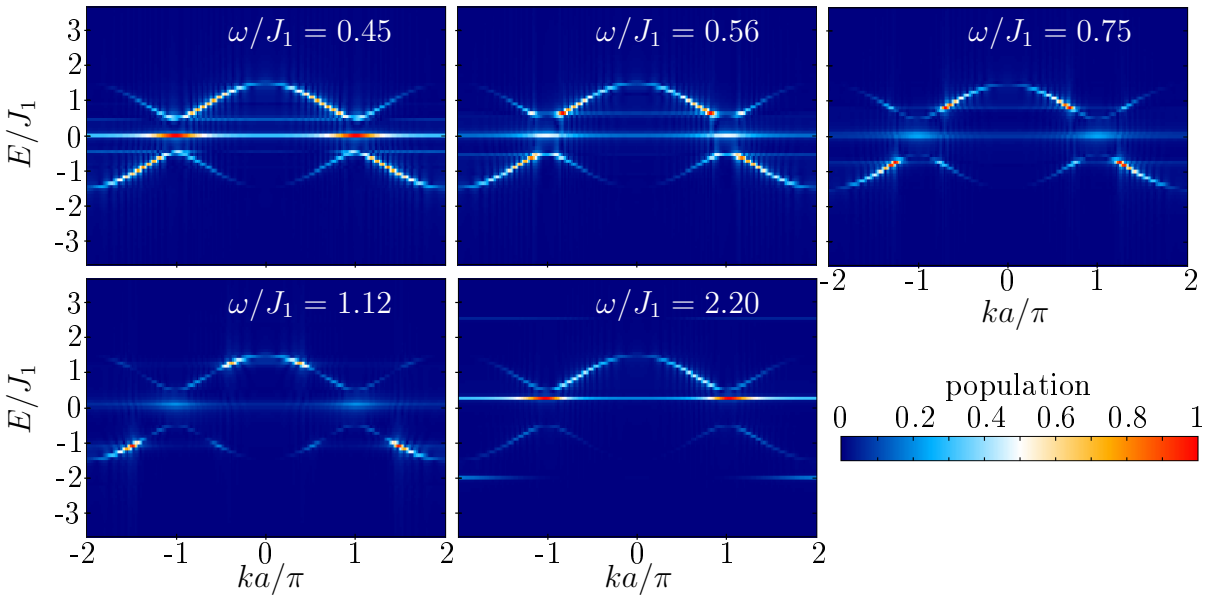

Figure 6.19: Numerically calculated band structures for the experimental parameters of Fig. 6.18 a).

the Floquet replicas coincide with bulk bands. Now, we want to look again into 2D systems (driven honeycomb).

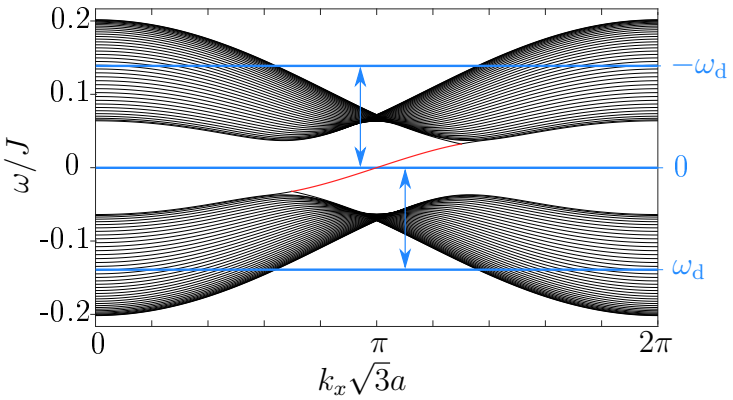

Figure 6.20: Sketch of the band structure settings such that a time-dependent defect can couple an edge to a bulk mode. The edge state is marked in red and the Floquet replicas of the defect in blue. One of the Floquet copies (quasi-)energetically coincides with the edge mode and another one with bulk modes, such that scattering of the edge state into the bulk can occur.

6.3 Dynamic defects in the FTI — other periodicity

After understanding, which local driving results in coupling of edge and bulk states, we return to the two-dimensional case of a Floquet topological insulator.

We look at a single defect incorporated into the zigzag edge of the FTI used in section 6.1. This defect now has the same helicity and helix radius R as the bulk waveguides, but we allow it to have a different frequency. We write ω for the frequency of the system and $\omega_\mathrm{d} \neq \omega$ for the frequency of the defect. The distance of the defect to its neighbors changes in time (along z) as

$$\boldsymbol{d}_{2,\mathrm{def}} = \boldsymbol{d}_2 + (R\cos(\omega_\mathrm{d} t), R\sin(\omega_\mathrm{d} t)) - (R\cos(\omega t), R\sin(\omega t))\,, \tag{6.18}$$

$$\boldsymbol{d}_{3,\mathrm{def}} = \boldsymbol{d}_3 + (R\cos(\omega_\mathrm{d} t), R\sin(\omega_\mathrm{d} t)) - (R\cos(\omega t), R\sin(\omega t))\,, \tag{6.19}$$

so that we have again a time-dependent amplitude and phase of the hopping. By tuning ω_d we should now be able to make one of the Floquet copies (quasi-)energetically coincide with an edge mode and another one with bulk modes (see Fig. 6.20), such that we depopulate the edge state. First calculations by C. Dauer using a Fermi's golden rule for Floquet system that he developed, indicate that this is indeed the case.

We want to compare the case of a defect with different frequency quantitatively to the cases considered in section 6.1. To do so, we numerically calculate the projected band structure /dispersion relation of the system including the defect. This is done by numerically solving the time-dependent Schrödinger equation for small time-steps with the time-dependent Hamiltonian of the system. Note that this time we write down the Hamiltonian in real-space. We set up the tight-binding Hamiltonian to contain 800 sites and only zigzag edges. We use the parameters of the strong defects of section 6.1. As initial condition we populate four edge waveguides with $k_y\sqrt{3}a = \pi$ at some distance from the defect. The excited state propagates along the edge unidirectionally, and then encounters the defect. Movies of the real-space propagation obtained this

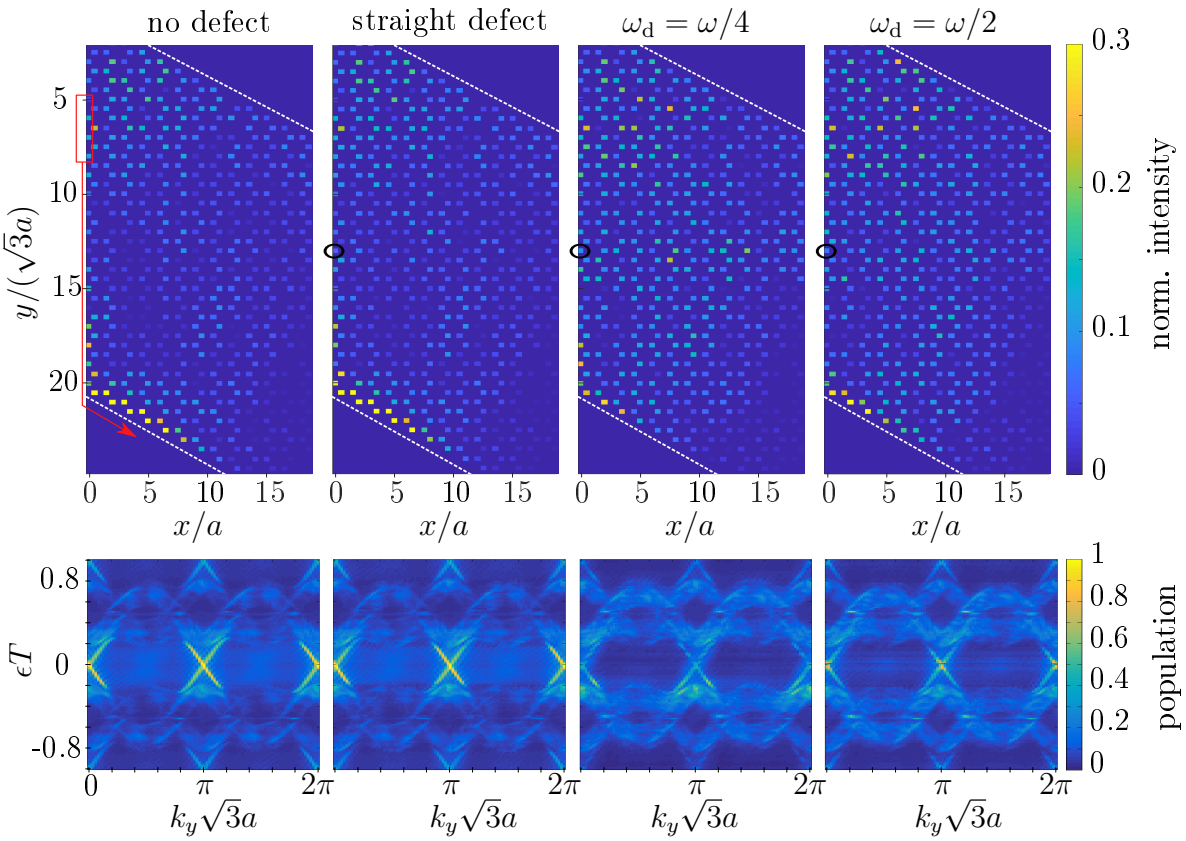

Figure 6.21: Numerically calculated population in real-space (upper row) and in projected k-space (lower row) for different defects. The upper row shows the intensity in real-space at $z = 850\,\mu m$. In the lower row, only one Floquet-Brillouin zone is shown. At $z = 0$ the sites marked by the red box in the real-space are populated. The black circle highlights the defect. The edge mode is robust against defects with $\omega_d = \omega$, but scatters into the bulk for defects with $\omega_d = \omega/2$ and $\omega_d = \omega/4$.

way can be found in [142]. The complex wave function of the distribution in the lattice is recorded for each time-step and stored into a 3D-matrix. This matrix is then Fourier transformed to yield the population of the states in k-space (β over k_x and k_y[3]). The resulting 'band structure' is projected onto the k_y-component along the zigzag edge containing the defect. The defect appears as a straight line in the band structure (fixed β for all values of k_y). As expected, in the energy direction it repeats with ω_d, while the bulk and edge bands repeat with ω.

Remember that a different curvature of the defect with respect to the rest of a waveguides amounts in an additional on-site potential in the Hamiltonian at the site of the defect (compare chapter 2, Eq. (2.73)). For the straight defect this was simply $\Delta V = \frac{k_0}{2} R^2 \omega^2$, while for defects with a different frequency the on-site potential becomes $\Delta V = \frac{k_0}{2} R^2 (\omega_d^2 - \omega^2)$. This on-site potential leads to an additional shift of the energy of the defect.

[3] z or 'time' transforms to β, and x and y to k_x and k_y respectively.

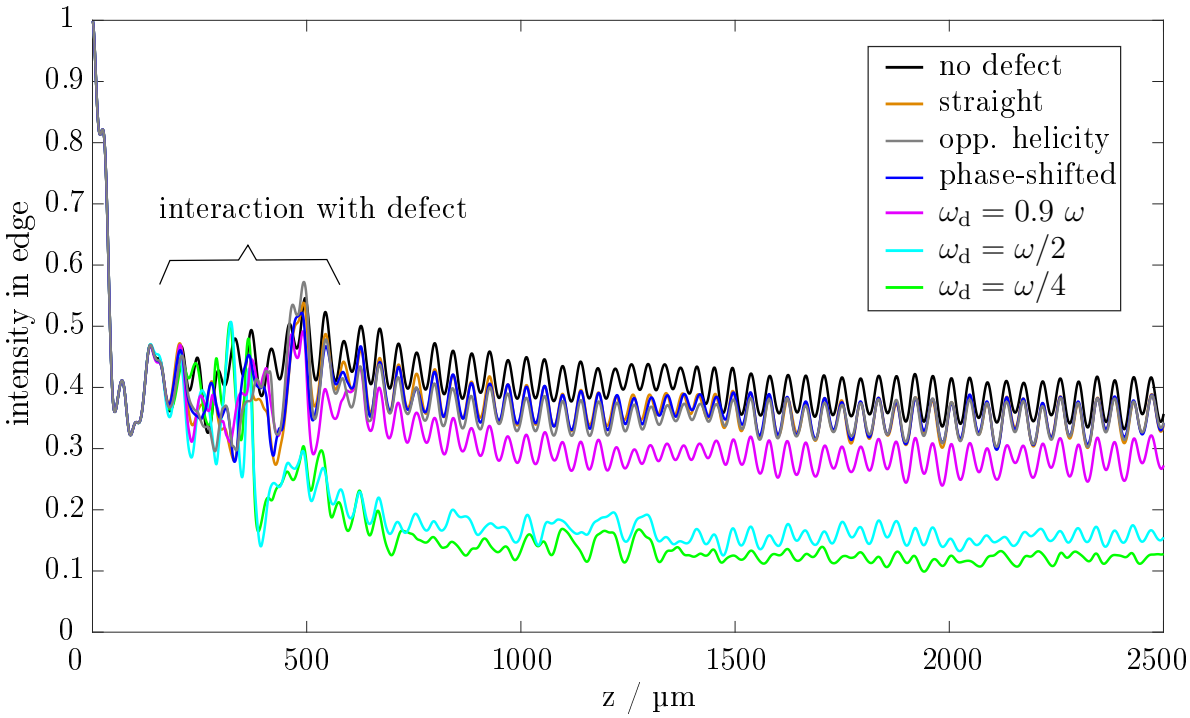

Figure 6.22: Sum of the intensity in the edge waveguides along z for different kinds of defects.

The results of the numerical calculations with an initially excited edge mode are shown in Fig. 6.21. The upper row shows a snapshot of the real-space (intensity in real-space at 'time' $z = 850\,\mu\text{m}$) and the lower row shows the population of the projected band structure, both for different kinds of defects. We see that for the lattice without defect and with straight defect (and for other defects with $\omega_d = \omega$ that are not shown) the edge modes are clearly visible in the real-space. Also, they are populated most strongly in the band structure. As $\omega_d = \omega$, the Floquet copies of both the defect and the edge bands, as well as the bulk bands always repeat with the same spacing in energy. This means that we can never get a (quasi-) energetic coincidence between a defect replica and an edge replica in one Floquet order, and between a defect replica and a bulk replica in another Floquet order. However, this is possible for $\omega_d = \omega/4$ and $\omega_d = \omega/2$, where we see that the population of the edge state in k-space decreases and the population of the bulk states increases. In the real-space snapshot we also see that the intensity of the edge mode is scattered into the bulk.

Summing up the intensity in the edge waveguides, and plotting it over z yields Fig. 6.22. As we can see, the remaining intensity in the edge after interaction with the defect is significantly smaller for the defects with $\omega_d = \omega/4$ and $\omega_d = \omega/2$, than for the defects with $\omega_d = \omega$. For $\omega_d = 0.9\omega$ the intensity in the edge also decreases, but not as much as for the defects with $\omega_d = \omega/4$ and $\omega_d = \omega/2$.

In conclusion, we see that even a single time-dependent defect can cause scattering of

edge states to bulk states. Whether the scattering occurs depends on the frequency of the defect with respect to the rest of the lattice. As the population in the edge state drops significantly, this means that already one single time-dependent defect can be rather harmful for topological edge transport. Regarding applications this means that one has to beware of these types of time-dependent defects.

6.4 What's left to do

So far we have only considered a single periodic time-dependent defect. One could extend the analysis to more defects with possibly different frequencies. This would amount in temporal disorder in the FTI. As has been shown in the course of topological Anderson insulators, (spatial) disorder does not always have a negative effect on the topology of a system, but can even induce non-trivial topology [157, 158]. An investigation of the effect of temporal disorder also seems worthwhile. In the same vein, one could also tune the frequency of the helices along the propagation length z.

Independent of topology, more interesting Floquet effects wait to be implemented in waveguide systems. Among them is transport through driven impurities [151]. As we have seen in this chapter, coupled waveguides provide an ideal platform to research all kinds of temporal effects in lattices.

7 Outlook

There are many other aspects of topological waveguide systems that are interesting to address in the future. One example, the creation of artificial gauge fields by states of light carrying orbital angular momentum, is introduced in the following section. In section 7.2 we also briefly want to highlight a different fabrication scheme for waveguides using DLW. In the end, we will list further interesting things to explore with coupled waveguide systems.

7.1 Waveguides with orbital angular momentum states

In the previous chapters we have created artificial gauge fields in our waveguide system by changing the waveguide axis. This was done either by bending the waveguides helically or tilting them by an angle with respect to each other. However, we can also use the modal properties of light to tailor AGF, e.g. by using states of light with orbital angular momentum (OAM).

States of light carrying OAM are characterized by a helical phase front and a donut-shaped intensity distribution in their cross-section (see Fig. 7.1). In their mathematical description they include an l-dependent azimuthal phase angle ϕ, such that their wave function is proportional to $\exp(-\mathrm{i}l\phi)$. The integer l is called rotational number (or sometimes also topological charge). A single photon carries $l\hbar$ orbital angular momentum. OAM can for example be created using q-plates [160], spiral phase-plates [161] or SLMs [162]. OAM of light is, e.g., used in optical tweezers [163, 164], stimulated emission depletion microscopy [165, 166] and lithography [67, 121, 167], and has potential applications for multiplexing [168].

Lately, it has been shown theoretically that light (and also ultracold atoms) carrying OAM can induce non-trivial topological phases in certain lattice geometries [169, 170]. This adds more degrees of freedom to the way we can create artificial gauge field, as we have a multitude of states available. Also, OAM of light bears the potential to unite topological protection with multiplexing.

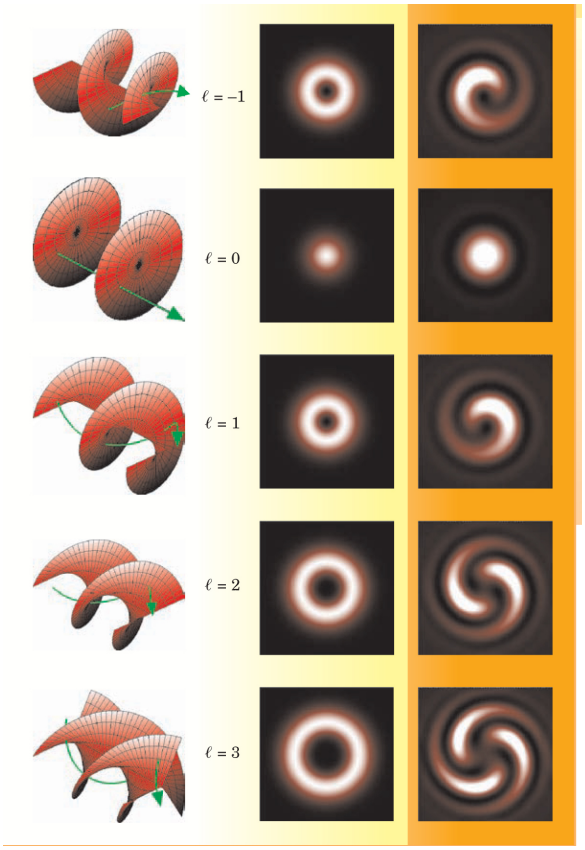

Figure 7.1: States with orbital angular momentum of light with different rotational numbers l. The left column shows the wave front of the beams, middle column displays the intensity, and right column displays the phase. Taken from [159].

The work on waveguides with orbital angular momentum is currently carried out in cooperation with Gerard Queralto (Universitat Autònoma de Barcelona) and Mark Kremer (University of Rostock), who provide the theory and numerical calculations.

Here, we review how OAM can induce non-trivial topology, following [169–173] and show first steps towards an implementation of the model in waveguides.

In cylindrical waveguides, states of light carrying OAM arise naturally as higher order Bessel beams (where the radial part of the beam is described by a Bessel function), that are solutions to the Helmholtz equation in cylindrical coordinates. We can express these waveguide modes as [73]

$$U(r, \phi, z) = u(r) \exp(-\mathrm{i}l(\phi - \phi_0)) \exp(-\mathrm{i}\beta z), \tag{7.1}$$

where $u(r)$ accounts for the radial part of the mode and ϕ_0 is the origin of the azimuthal coordinate, i.e. a phase offset, defined with respect to the x-axis.

For two equal waveguides m and n the coupling between modes with OAM of $l_1\hbar$ and

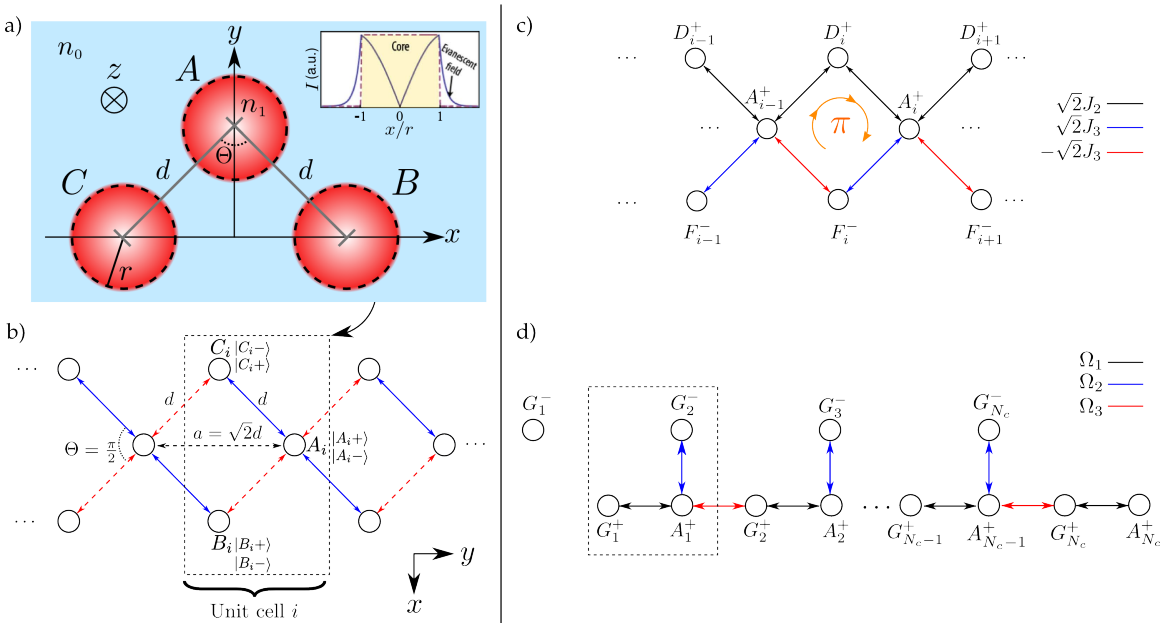

Figure 7.2: a) Sketch of the system of three waveguides arranged in a right triangle, adapted from [173] licensed under [155]. b) Diamond lattice of waveguides, adapted from [170]. Dashed red lines indicate complex hopping. '+' stands for OAM states of $l = +1$, while '-' stands for $l = -1$. c) After the first basis rotation we can identify a π flux through the plaquette of each subsystem Hamiltonian. d) A second basis rotation allows to display the subsystem as a modified SSH chain with dangling bonds. c) and d) are taken from [169]. Note that in c) and d) the circles do not denote the actual waveguides anymore, but sites in the new basis.

$l_2\hbar$ is given by [171]

$$J^{nl_2}_{ml_1} \propto \exp(\mathrm{i}(l_1 - l_2)\phi_0) \iint u^*_m(r_m) \exp(\mathrm{i}l_1\phi_m) u_n(r_n) \exp(-\mathrm{i}l_2\phi_n)\; r_n \mathrm{d}r_n \mathrm{d}\phi_n \qquad (7.2)$$

where the integration is over the complete space[(1)]. This means that the coupling for $l_1 \neq l_2$ depends on ϕ_0, i.e., how we choose to position the coordinate system. For two waveguides we can always choose the x-axis to coincide with the line connecting the waveguides, such that ϕ_0 vanishes. For three angled waveguides (see, e.g., Fig. 7.2 a)) we can not make ϕ_0 vanish for all directions. There, one of the couplings depends on the angle θ between the waveguides, and can in general become complex. Therefore, using OAM modes in waveguides naturally induces complex couplings, depending on the geometry.

We start with a system of three equal waveguides arranged in a right triangle where $\theta = \pi/2$, as shown in Fig. 7.2 a), with $d_{AC} = d_{AB} = d$ and $|l_1| = |l_2| = 1$. We choose $\phi_0 = 0$ for the A and C waveguide, such that the hopping between them is real. For

(1) The index n at the integration variables indicates that we choose the origin of integration in the waveguide n.

modes with equal OAM in the A and B waveguide the hopping between them is also real, whereas it is complex and $\propto \exp(\pm i2\theta)$ for different signs of the OAM modes $l_1/l_2 = -1$. We neglect the coupling between the B and C waveguide, as the hopping decreases exponentially with the distance, such that we can assume that it is much smaller than between A and C. Note that there is also self-coupling between OAM modes of different sign in the same waveguide when a second waveguide is present, as there is no rotational symmetry of the complete system anymore. However, the self-coupling is small compared to the coupling between different waveguides (cross-coupling). In general, spin-orbit coupling between the polarization of the light mode and its OAM can also take place [174–177], but we can neglect it when the index contrast between waveguide and surrounding material is small.

Stacking multiple of these triangles along the y direction creates a diamond lattice, as shown in Fig. 7.2 b). There, two of the couplings between the $l_1 = 1$ and $l_2 = -1$ OAM modes in one plaquette are complex. Naively, one would think that this amounts to a flux of 2π for an angle of $\theta = \pi/2$. However, the authors of [170] showed that the diamond chain exhibits non-trivial topology for OAM modes of $|l| = 1$. This can be better understood when a basis rotation is performed. The old basis included the six possible states for either $l = +1$ or $l = -1$ in each site A, B, or C, denoted as $|A, +\rangle$ etc. The new basis keeps the $|A, \pm\rangle$ states, but uses superpositions of $|B, \pm\rangle$ and $|C, \pm\rangle$. In this basis, one can see that the complete Hamiltonian of the system actually consists of two uncoupled Hamiltonians, where each of them has a flux of π in the plaquette (see Fig. 7.2 c). By another basis rotation of similar vein[(2)], it can be shown that this system corresponds to a modified SSH chain with extra dangling sites (G_i^-, Fig. 7.2 d), and that the Zak phase is always π [170].

For equal absolute value of the coupling J_2 between states with equal sign of the rotational number $l = \pm 1$, and J_3 between states with opposite sign, the coupling Ω_3 in the last basis rotation becomes zero. Then, the chain decouples into trimers, where one of them is marked by the dashed box in Fig. 7.2 d). This decoupling leads to the formation of only flat bands in the band structure and to Aharonov-Bohm caging [169, 170]. This way, upon the excitation of the central site A_i with a superposition of $l = 1$ and $l = -1$ (i.e. linear combination of $|A_i, -\rangle$ and $|A_i, +\rangle$) the light only couples to its four neighbors and back. Thus, in time it never populates more than these five sites.

We want to implement this Aharonov-Bohm caging induced by OAM of light in our micro-printed waveguide lattice. While doing so, we face the following challenges:
1) The refractive index contrast Δn between waveguide and surrounding material needs to be small, such that we can neglect the spin-orbit coupling.
2) The absolute values of the coupling J_2 and J_3 differ significantly for small values of the spacing, see Fig. 7.3. The cross-coupling between states with opposite sign of

(2) for details see [170]

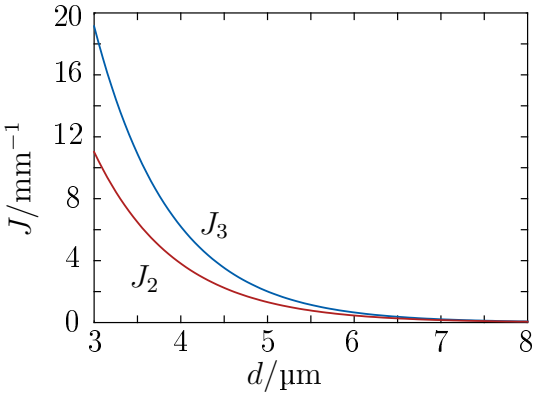

Figure 7.3: Coupling J_2 between states with equal sign of the rotational number $l = \pm 1$ and J_3 between states with opposite sign, in dependence of the distance between waveguides d. The parameters are: $r = 1.3\,\mu\mathrm{m}$, $n_{\mathrm{wg}} = 1.56$, $n_0 = 1.54$, $\lambda = 700\,\mathrm{nm}$.
Figure courtesy of Gerard Queralto.

OAM is always bigger than that with the same sign. Therefore, we have to use a relatively large distance between the waveguides to come close to equal coupling. This also means that we either need long samples in terms of the propagation distance, or that we can not observe much of the dynamics in z, otherwise.

In the previous works we had used *SU8* to create waveguides. While we were able to propagate OAM states with $l = 1$, and superposition of $l = 1$ and $l = -1$ through *SU8* waveguides nicely (see Fig. 7.4 a) and b)), the refractive index contrast was far too large to fulfill points 1) and 2). Due to this, we tried another photoresist, *KMPR 1005* [178] thinned with the solvent Cyclopentanone in relation 2:1, with a contrast of $\Delta n = 0.02$. While it worked well for short samples up to $h < 250\,\mu\mathrm{m}$ (see Fig. 7.4 c), it did not infiltrate longer samples. Therefore, we looked for alternative fabrication methods and came across Ref. [145].

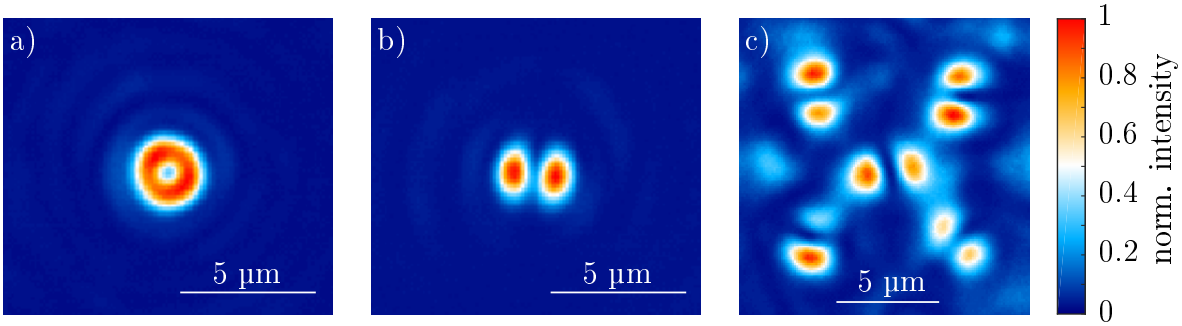

Figure 7.4: a) Measurement of OAM $l = 1$ mode propagated through a single waveguide. b) superposition of $l = 1$ and $l = -1$ propagated through a single waveguide. c) Output intensity distribution when the superposition of $l = 1$ and $l = -1$ is coupled into the central site of a diamond lattice. In a) and b) *SU8* was used as waveguide material, while in c) we used the photoresist *KMPR*. In all experiments, we used an aberration compensated phase-image loaded onto an SLM, in combination with a $4f$-setup of lenses and an objective to excite the corresponding OAM modes in the waveguides.

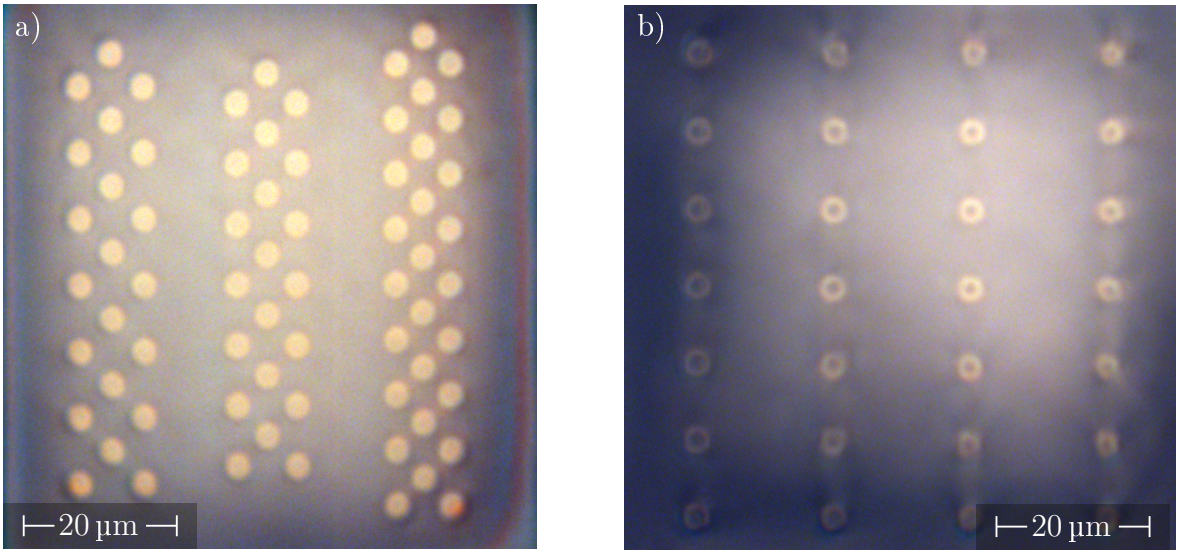

Figure 7.5: Microscope images of waveguides, fabricated with the new method. a) Diamond chain. The laser power used for the surrounding material was 30% of the maximum value, and for the waveguides 50%. At maximum laser power, the power in the objective's entrance pupil is about 80 mW. b) Waveguides with a donut-shaped cross-section; laser power of the donuts 40%, rest 22%. The contrast in the images was increased for better visibility.

7.2 New fabrication methods

A recent paper [145] states that the refractive index of *IP-Dip* varies in dependence of the exposure dose. A similar behavior has also been stated to occur in a different photoresist [179]. We use this exposure dependence to directly create low index contrast waveguides in a single fabrication step. Using direct laser writing, we fabricate arrays of waveguides as shown in Fig. 7.5, where the inside of the waveguides is written with high laser power and the outside with low laser power, just above the polymerization threshold. Usually, such low laser dose leads to strong deformation of the structure during development (see also section 3.1.1). Therefore, we do not develop the sample, but post-cure it completely using UV exposure. To do so, the sample (including the uncured resist) is illuminated with UV light in the wavelength range of 320 nm − 500 nm for 60 s, using an *OmniCure S2000* system [180] with 95% iris opening, amounting to an approximate irridiance of $10\,\mathrm{W/cm^2}$. This method has the extra advantage of greater stability for high structures [131]. One draw-back could be a remaining bulb of resist on top of the structures. However, this method approach also saves a lot of working steps, as one can skip development, infiltration and baking.

We deduce the refractive index contrast between waveguides and surrounding material by measuring the coupling in a 1D chain of waveguides in dependence on the exposure difference, see Fig. 7.6. We couple light with $\lambda = 700\,\mathrm{nm}$ into the central waveguide of the chain, and observe the output intensity after a propagation distance of $h = 270\,\mu\mathrm{m}$.

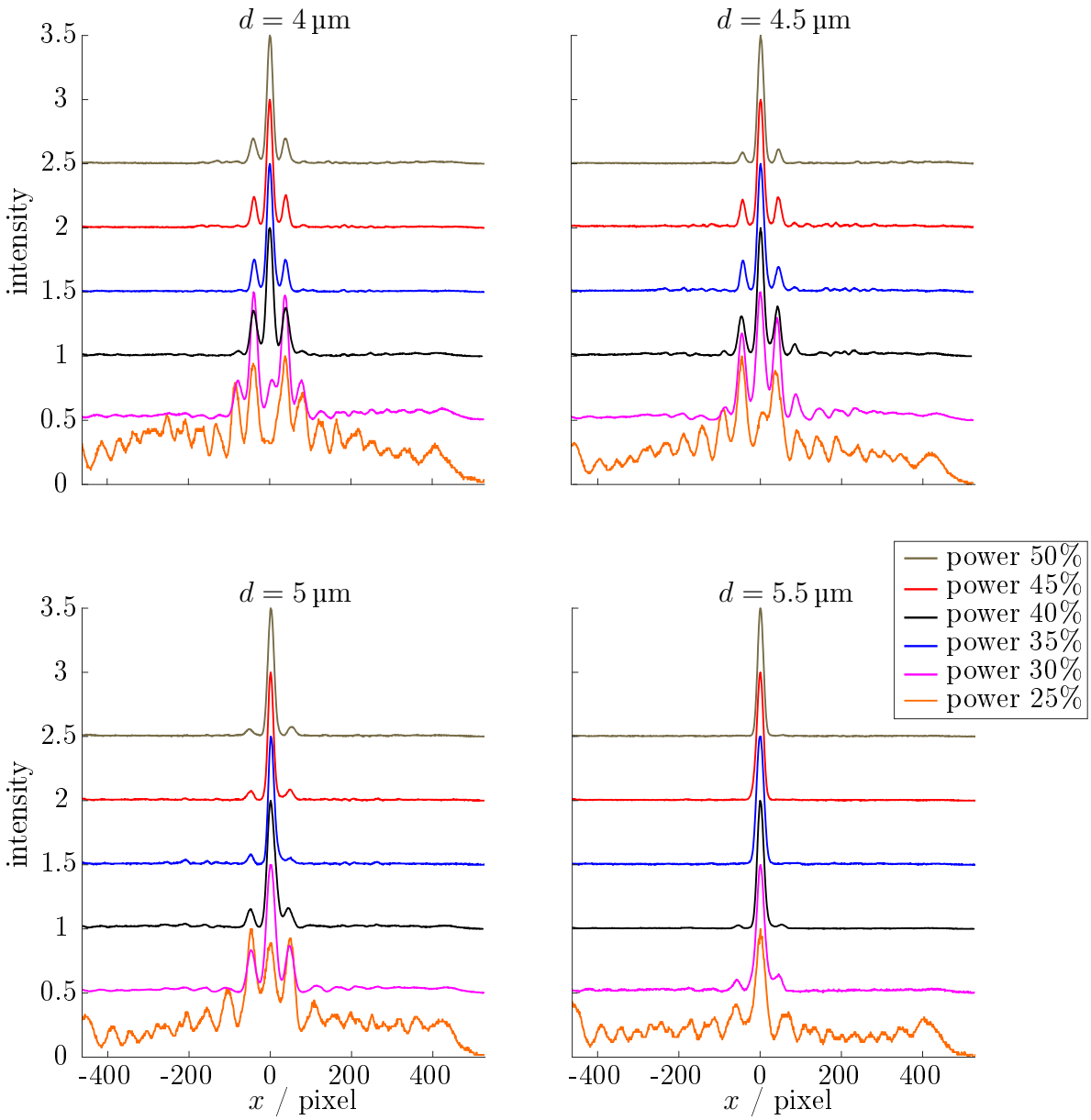

Figure 7.6: Measurements of the coupling in a 1D chain of waveguides, fabricated by the new method. The legend indicates the laser power used for the waveguides, while the power for the surrounding block was fixed at 22%. Note that for a laser power of 25% the confinement is very weak and thus radiation losses are severe, hence the noise in the data. Propagation distance is $h = 270\,\mu\text{m}$, waveguide radius $r = 1.2\,\mu\text{m}$ for different center-to-center distances d.

The measurements indicate a strong dependence of the index contrast on the exposure for low laser power. For high laser power, almost no change is observed anymore. Therefore, we assume that in the regime of high laser power, almost all the resist is cross-linked. The measurements also indicate that we can achieve a refractive index contrast of up to $\Delta n \approx 0.01$ in accordance with [145].

The new fabrication method also allows to fabricate more complex refractive index landscapes and waveguide geometries, e.g. waveguides with a donut-shaped cross-section (Fig. 7.5 b). These waveguides transmit OAM modes more easily, as they suppress the transmission of the Gaussian ground mode [181]. DLW allows to fabricate such waveguides even with modulation along the propagation axis, creating, e.g., segmented waveguides [58] or temporally modulated on-site potentials. Due to the increased stability of the samples, we also hope to achieve higher waveguide structures than the present ones, which allows to observe more of the hopping dynamics.

7.3 Summary and more to explore

As pointed out in this thesis, model systems of evanescently coupled waveguides serve to explore a multitude of effects. We have seen how interfaces between artificial gauge fields change the wave vector components of light, an effect useful for routing. We have also explored oscillating interface states at the boundary between two FTIs. Such a system could be used as a beamsplitter for a topological edge mode, or — possibly — to trap a topological state and release it at the desired time. In the presence of time-dependent defects we have evaluated the robustness of a topological edge mode. The results showed that such defects lead to scattering of the edge mode to the bulk for certain frequencies of the driving. This knowledge is especially useful in view of future applications that harness topological edge modes.

Currently, the field of topological photonics is restricted to non-interacting (linear) systems. Introducing interactions between photons, or between photons and host materials, would add another degree of freedom and open up a new branch for topological photonics. Interactions between photons can be induced using (Kerr) nonlinear materials. This would enable these systems to simulate many-body physics in the mean-field limit – more accurately reflecting the real world – and render them even more versatile. Adding interactions globally, waveguide systems provide a complementary platform to ultra-cold atoms in optical lattices. Furthermore, due to the possible manipulation of single sites in waveguide systems, the local influence of interactions can be examined. Many novel effects have been predicted to occur in interacting lattice systems. For example, a recent theory paper predicts that topological protection breaks down when interactions are strong enough [182]. Another work [183] proposes coherent perfect absorption in waveguide arrays, facilitated by nonlinear effects. However, none of these predicted effects has been observed so far, as realizable nonlinearities accessible in fabricated waveguides are too weak. Inverse structures of 3D printed waveguide systems could be infiltrated by materials with large nonlinearities. This seems to be a very promising approach for the implementation of interactions in photonic model systems. With that, many more interesting phenomena await to be explored.

A Appendix

A.1 How to choose the best laser power for the inverse waveguide samples

As said in section 3.1.2, the laser dose deposited into the resist is a critical parameter for the sample quality. In our DLW setup, the laser power entering the objective, as well as the point-spread function of the laser focus and its aberrations, changed with every re-alignment of the setup. Therefore, the power values of the laser needed to be adjusted. To be able to identify the current optimal value of the laser power, the following procedure was used: Several small samples were printed onto the same substrate using different laser powers. The laser power was varied in small steps. The threshold of polymerization was determined visually, i.e., by observing the writing process via the camera to determine if a change in the refractive index was visible and a printed structure appeared. The power value at which the first structure became visible, was determined as the threshold. To this value we added 2% (of the maximum power) for the printing of the actual sample, to guarantee reliable polymerization and to prevent exceedingly strong shrinking of the sample.

A.2 How to improve NanoWrite's writing times

To print a structure via DLW the trajectory of it must be given in form of coordinate triplets x, y, z. A following *Write* command indicates that a line is finished and that the positioning should start again. Via this software, also the velocity of the relative movement between laser focus and substrate is controlled, given by the variable *ScanSpeed*. At a *Write* point, this movement is decelerated, and accelerated again towards the new starting position. The deposited laser power is modulated by the AOM, and in the software chosen by the product of the variables *LaserPower* and *PowerScaling*. It can also be controlled keeping the *PowerScaling* fixed and adding a fourth row to the coordinate triplets, that varies the *LaserPower*. Depending on the envisaged structure this can be of benefit, as *Write* commands along a connected line can be replaced by just setting the *LaserPower* to zero at this position. Thereby, writing times can be

reduced tremendously, while ensuring a constant writing velocity, that is not altered due to accelerating and decelerating at a *Write* point.

Bibliography

[1] Z. Wang, Y. Chong, J. D. Joannopoulos, and M. Soljačić. Observation of unidirectional backscattering-immune topological electromagnetic states. *Nature*, 461(7265):772, 2009.

[2] M. Hafezi, E. A. Demler, M. D. Lukin, and J. M. Taylor. Robust optical delay lines with topological protection. *Nature Physics*, 7(11):907, 2011.

[3] M. C. Rechtsman, J. M. Zeuner, Y. Plotnik, Y. Lumer, D. Podolsky, F. Dreisow, S. Nolte, M. Segev, and A. Szameit. Photonic Floquet topological insulators. *Nature*, 496(7444):196, 2013. Reprinted by permission from Nature/Springer, copyright Springer Nature (2013).

[4] M. C. Rechtsman, Y. Lumer, Y. Plotnik, A. Perez-Leija, A. Szameit, and M. Segev. Topological protection of photonic path entanglement. *Optica*, 3(9):925, 2016.

[5] S. Barik, A. Karasahin, C. Flower, T. Cai, H. Miyake, W. DeGottardi, M. Hafezi, and E. Waks. A topological quantum optics interface. *Science*, 359(6376):666, 2018.

[6] G. Harari, M. A. Bandres, Y. Lumer, M. C. Rechtsman, Y. D. Chong, M. Khajavikhan, D. N. Christodoulides, and M. Segev. Topological insulator laser: Theory. *Science*, 359(6381):eaar4003, 2018.

[7] M. A. Bandres, S. Wittek, G. Harari, M. Parto, J. Ren, M. Segev, D. N. Christodoulides, and M. Khajavikhan. Topological insulator laser: Experiments. *Science*, 359(6381):eaar4005, 2018. Reprinted with permission from AAAS.

[8] L. Lu, J. D. Joannopoulos, and M. Soljačić. Topological photonics. *Nature Photonics*, 8(11):821, 2014.

[9] B.-Y. Xie, H.-F. Wang, X.-Y. Zhu, M.-H. Lu, Z. D. Wang, and Y.-F. Chen. Photonics meets topology. *Optics Express*, 26(19):24531, 2018.

[10] T. Ozawa, H. M. Price, A. Amo, N. Goldman, M. Hafezi, L. Lu, M. C. Rechtsman, D. Schuster, J. Simon, O. Zilberberg, and I. Carusotto. Topological photonics. *Reviews of Modern Physics*, 91(1):015006, 2019.

[11] W. P. Su, J. R. Schrieffer, and A. J. Heeger. Soliton excitations in polyacetylene. *Physical Review B*, 22(4):2099, 1980.

[12] NobelPrize.org. Nobel Media AB 2019. The Nobel Prize in Physics 2016 – Prize announcement. https://www.nobelprize.org/prizes/physics/2016/prize-announcement/, (accessed 23.07.2019).

[13] N. H. D. Khang, Y. Ueda, and P. N. Hai. A conductive topological insulator with large spin Hall effect for ultralow power spin–orbit torque switching. *Nature Materials*, 17(9):808, 2018.

[14] S. D. Sarma, M. Freedman, and C. Nayak. Majorana zero modes and topological quantum computation. *npj Quantum Information*, 1:15001, 2015.

[15] B. Lian, X.-Q. Sun, A. Vaezi, X.-L. Qi, and S.-C. Zhang. Topological quantum computation based on chiral Majorana fermions. *Proceedings of the National Academy of Sciences*, 115(43):10938, 2018.

[16] M. Aidelsburger, M. Atala, M. Lohse, J. T. Barreiro, B. Paredes, and I. Bloch. Realization of the Hofstadter Hamiltonian with Ultracold Atoms in Optical Lattices. *Physical Review Letters*, 111(18):185301, 2013.

[17] G. Jotzu, M. Messer, R. Desbuquois, M. Lebrat, T. Uehlinger, D. Greif, and T. Esslinger. Experimental realization of the topological Haldane model with ultracold fermions. *Nature*, 515(7526):237, 2014.

[18] N. Fläschner, B. S. Rem, M. Tarnowski, D. Vogel, D.-S. Lühmann, K. Sengstock, and C. Weitenberg. Experimental reconstruction of the Berry curvature in a Floquet Bloch band. *Science*, 352(6289):1091, 2016.

[19] M. Leder, C. Grossert, L. Sitta, M. Genske, A. Rosch, and M. Weitz. Real-space imaging of a topologically protected edge state with ultracold atoms in an amplitude-chirped optical lattice. *Nature Communications*, 7:13112, 2016.

[20] V. Peano, C. Brendel, M. Schmidt, and F. Marquardt. Topological Phases of Sound and Light. *Physical Review X*, 5(3):031011, 2015.

[21] C. W. Peterson, W. A. Benalcazar, T. L. Hughes, and G. Bahl. A quantized microwave quadrupole insulator with topologically protected corner states. *Nature*, 555(7696):346, 2018.

[22] M. Fitzpatrick, N. M. Sundaresan, A. C. Y. Li, J. Koch, and A. A. Houck. Observation of a Dissipative Phase Transition in a One-Dimensional Circuit QED Lattice. *Physical Review X*, 7(1):011016, 2017.

[23] C. H. Lee, S. Imhof, C. Berger, F. Bayer, J. Brehm, L. W. Molenkamp, T. Kiessling, and R. Thomale. Topolectrical Circuits. *Communications Physics*, 1(1):39, 2018.

[24] S. Imhof, C. Berger, F. Bayer, J. Brehm, L. W. Molenkamp, T. Kiessling, F. Schindler, C. H. Lee, M. Greiter, T. Neupert, and R. Thomale. Topolectrical-circuit realization of topological corner modes. *Nature Physics*, 14(9):925, 2018. Reprinted by permission from Nature/Springer, copyright Springer Nature (2018).

[25] N. A. Olekhno, E. I. Kretov, A. A. Stepanenko, D. S. Filonov, V. V. Yaroshenko, B. Cappello, L. Matekovits, and M. A. Gorlach. Topological edge states of interacting photon pairs realized in a topolectrical circuit. *arXiv preprint, arXiv:1907.01016*, 2019.

[26] Z. Yang, F. Gao, X. Shi, X. Lin, Z. Gao, Y. Chong, and B. Zhang. Topological Acoustics. *Physical Review Letters*, 114(11):114301, 2015.

[27] C. He, X. Ni, H. Ge, X.-C. Sun, Y.-B. Chen, M.-H. Lu, X.-P. Liu, and Y.-F. Chen. Acoustic topological insulator and robust one-way sound transport. *Nature Physics*, 12(12):1124, 2016.

[28] S. Yves, R. Fleury, F. Lemoult, M. Fink, and G. Lerosey. Topological acoustic polaritons: robust sound manipulation at the subwavelength scale. *New Journal of Physics*, 19(7):075003, 2017.

[29] S. Klembt, T. H. Harder, O. A. Egorov, K. Winkler, R. Ge, M. A. Bandres, M. Emmerling, L. Worschech, T. C. H. Liew, M. Segev, C. Schneider, and S. Höfling. Exciton-polariton topological insulator. *Nature*, 562(7728):552, 2018.

[30] S. Mittal, J. Fan, S. Faez, A. Migdall, J. M. Taylor, and M. Hafezi. Topologically Robust Transport of Photons in a Synthetic Gauge Field. *Physical Review Letters*, 113(8):087403, 2014.

[31] H. M. Price, T. Ozawa, N. Goldman, O. Zilberberg, and I. Carusotto. Towards four-dimensional photonics. In *Advances in Photonics of Quantum Computing, Memory, and Communication IX*, volume 9762, page 97620V. International Society for Optics and Photonics, 2016.

[32] E. Lustig, S. Weimann, Y. Plotnik, Y. Lumer, M. A. Bandres, A. Szameit, and M. Segev. Photonic topological insulator in synthetic dimensions. *Nature*, 567(7748):356, 2019.

[33] F. Schindler, A. M. Cook, M. G. Vergniory, Z. Wang, S. S. P. Parkin, B. A. Bernevig, and T. Neupert. Higher-order topological insulators. *Science Advances*, 4(6):eaat0346, 2018.

[34] A. El Hassan, F. K. Kunst, A. Moritz, G. Andler, E. J. Bergholtz, and M. Bourennane. Corner states of light in photonic waveguides. *arXiv preprint, arXiv:1812.08185*, 2018.

[35] L. Lu, Z. Wang, D. Ye, L. Ran, L. Fu, J. D. Joannopoulos, and M. Soljačić. Experimental observation of Weyl points. *Science*, 349(6248):622, 2015.

[36] M.-A. Miri and A. Alù. Exceptional points in optics and photonics. *Science*, 363(6422):eaar7709, 2019.

[37] L. B. Stauffer. Scientists Find Same Wild Physical Effect Happening in Two Vastly Different Materials. https://gizmodo.com/scientists-find-same-wild-physical-effect-happening-in-1823765700, 2018 (accessed 24.07.2019).

[38] Creative Commons public license. CC BY 3.0. https://creativecommons.org/licenses/by/3.0/legalcode, 2017 (accessed 20.03.2019).

[39] M. I. Shalaev, W. Walasik, A. Tsukernik, Y. Xu, and N. M. Litchinitser. Robust topologically protected transport in photonic crystals at telecommunication wavelengths. *Nature Nanotechnology*, 14(1):31, 2019.

[40] M. Wimmer, H. M. Price, I. Carusotto, and U. Peschel. Experimental measurement of the Berry curvature from anomalous transport. *Nature Physics*, 13(6):545, 2017.

[41] F. Bleckmann, Z. Cherpakova, S. Linden, and A. Alberti. Spectral imaging of topological edge states in plasmonic waveguide arrays. *Physical Review B*, 96(4):045417, 2017.

[42] A. Blanco-Redondo, I. Andonegui, M. J. Collins, G. Harari, Y. Lumer, M. C. Rechtsman, B. J. Eggleton, and M. Segev. Topological Optical Waveguiding in Silicon and the Transition between Topological and Trivial Defect States. *Physical Review Letters*, 116(16):163901, 2016. Reprinted with permission. Copyright (2016) by the American Physical Society.

[43] J. Zeuner. *Complex edge states in tailored photonic graphene.* PhD Thesis, Friedrich-Schiller-Universität Jena, 2017.

[44] S. Mukherjee, A. Spracklen, M. Valiente, E. Andersson, P. Öhberg, N. Goldman, and R. R. Thomson. Experimental observation of anomalous topological edge modes in a slowly driven photonic lattice. *Nature Communications*, 8:13918, 2017.

[45] S. Longhi. Quantum-optical analogies using photonic structures. *Laser & Photonics Reviews*, 3(3):243, 2009.

[46] A. Szameit and S. Nolte. Discrete optics in femtosecond-laser-written photonic structures. *Journal of Physics B*, 43(16):163001, 2010.

[47] Q. Lin and S. Fan. Light guiding by effective gauge field for photons. *Physical Review X*, 4(3):031031, 2014.

[48] Y. Plotnik, M. A. Bandres, S. Stützer, Y. Lumer, M. C. Rechtsman, A. Szameit, and M. Segev. Analogue of Rashba pseudo-spin-orbit coupling in photonic lattices by gauge field engineering. *Physical Review B*, 94(2):020301, 2016.

[49] Y. Lumer, M. A. Bandres, M. Heinrich, L. J. Maczewsky, H. Herzig-Sheinfux, A. Szameit, and M. Segev. Light guiding by artificial gauge fields. *Nature Photonics*, 13(5):339, 2019.

[50] F. D. M. Haldane and S. Raghu. Possible Realization of Directional Optical Waveguides in Photonic Crystals with Broken Time-Reversal Symmetry. *Physical Review Letters*, 100(1):013904, 2008.

[51] S. Raghu and F. D. M. Haldane. Analogs of quantum-Hall-effect edge states in photonic crystals. *Physical Review A*, 78(3):033834, 2008.

[52] T. Kitagawa, E. Berg, M. Rudner, and E. Demler. Topological characterization of periodically driven quantum systems. *Physical Review B*, 82(23):235114, 2010.

[53] N. H. Lindner, G. Refael, and V. Galitski. Floquet topological insulator in semiconductor quantum wells. *Nature Physics*, 7(6):490, 2011.

[54] I. L. Garanovich, S. Longhi, A. A. Sukhorukov, and Y. S. Kivshar. Light propagation and localization in modulated photonic lattices and waveguides. *Physics Reports*, 518(1-2):1, 2012.

[55] T. Oka and H. Aoki. Photovoltaic Hall effect in graphene. *Physical Review B*, 79(8):081406, 2009.

[56] M. C. Rechtsman, Y. Plotnik, J. M. Zeuner, D. Song, Z. Chen, A. Szameit, and M. Segev. Topological Creation and Destruction of Edge States in Photonic Graphene. *Physical Review Letters*, 111(10):103901, 2013. Reprinted with permission. Copyright (2013) by the American Physical Society.

[57] C. Jörg, F. Letscher, M. Fleischhauer, and G. von Freymann. Dynamic defects in photonic Floquet topological insulators. *New Journal of Physics*, 19(8):083003, 2017.

[58] S. Longhi. Image reconstruction in segmented waveguide arrays. *Optics Letters*, 33(5):473, 2008.

[59] S. Mukherjee, A. Spracklen, D. Choudhury, N. Goldman, P. Öhberg, E. Andersson, and R. R. Thomson. Modulation-assisted tunneling in laser-fabricated photonic Wannier–Stark ladders. *New Journal of Physics*, 17(11):115002, 2015.

[60] C. Jörg. Erste Schritte in Richtung optischer topologischer Isolatoren durch direktes Laserschreiben. Diploma thesis, Technische Universität Kaiserslautern, 2015.

[61] J. Schulz. Herstellung und Charakterisierung evaneszent gekoppelter Wellenleiterstrukturen. Master's thesis, Technische Universität Kaiserslautern, 2018.

[62] S. Maruo, O. Nakamura, and S. Kawata. Three-dimensional microfabrication with two-photon-absorbed photopolymerization. *Optics Letters*, 22(2):132, 1997.

[63] H.-B. Sun, S. Matsuo, and H. Misawa. Three-dimensional photonic crystal structures achieved with two-photon-absorption photopolymerization of resin. *Applied Physics Letters*, 74(6):786, 1999.

[64] M. Deubel, G. von Freymann, and M. Wegener. Direct laser writing of three-dimensional photonic-crystal templates for telecommunications. *Nature Materials*, 3(7):444, 2004.

[65] S. Juodkazis, V. Mizeikis, and H. Misawa. Three-Dimensional Structuring of Resists and Resins by Direct Laser Writing and Holographic Recording. In *Photoresponsive Polymers I*, page 157. Springer, 2007.

[66] G. von Freymann, A. Ledermann, M. Thiel, I. Staude, S. Essig, K. Busch, and M. Wegener. Three-Dimensional Nanostructures for Photonics. *Advanced Functional Materials*, 20(7):1038, 2010.

[67] J. Fischer and M. Wegener. Three-dimensional optical laser lithography beyond the diffraction limit. *Laser & Photonics Reviews*, 7(1):22, 2013.

[68] M. Malinauskas, M. Farsari, A. Piskarskas, and S. Juodkazis. Ultrafast laser nanostructuring of photopolymers: A decade of advances. *Physics Reports*, 533(1):1, 2013.

[69] H. Fouckhardt. *Halbleiterlaser: unter Verwendung Fourier-optischer Methoden.* Vieweg+Teubner Verlag, 1st edition, 2011.

[70] G. Czycholl. *Theoretische Festkörperphysik.* Springer-Verlag Berlin Heidelberg, 3rd edition, 2008.

[71] L. J. Maczewsky, S. Weimann, M. Kremer, M. Heinrich, and A. Szameit. Experimental study of non-orthogonal modes in tight-binding lattices. In *Conference on Lasers and Electro-Optics*, page FM1C.6. Optical Society of America, 2019.

[72] A. Yariv. *Optical Electronics in Modern Communications.* Oxford University Press, USA, 5th edition, 1997.

[73] B. E. A. Saleh and M. C. Teich. *Grundlagen der Photonik.* Wiley-VCH Verlag, 2nd edition, 2008.

[74] K. Okamoto. *Fundamentals of Optical Waveguides.* Academic press, 2nd edition, 2006.

[75] J. Noh, S. Huang, D. Leykam, Y. D. Chong, K. P. Chen, and M. C. Rechtsman. Experimental observation of optical Weyl points and Fermi arc-like surface states. *Nature Physics*, 13(6):611, 2017.

[76] R. Morandotti, U. Peschel, J. S. Aitchison, H. S. Eisenberg, and Y. Silberberg. Experimental Observation of Linear and Nonlinear Optical Bloch Oscillations. *Physical Review Letters*, 83(23):4756, 1999.

[77] A. Block, C. Etrich, T. Limboeck, F. Bleckmann, E. Soergel, C. Rockstuhl, and S. Linden. Bloch oscillations in plasmonic waveguide arrays. *Nature Communications*, 5:3843, 2014.

[78] L. Martin, G. Di Giuseppe, A. Perez-Leija, R. Keil, F. Dreisow, M. Heinrich, S. Nolte, A. Szameit, A. F. Abouraddy, D. N. Christodoulides, and B. E. A. Saleh. Anderson localization in optical waveguide arrays with off-diagonal coupling disorder. *Optics Express*, 19(14):13636, 2011.

[79] J. M. Zeuner, M. C. Rechtsman, Y. Plotnik, Y. Lumer, S. Nolte, M. S. Rudner, M. Segev, and A. Szameit. Observation of a Topological Transition in the Bulk of a Non-Hermitian System. *Physical Review Letters*, 115(4):040402, 2015.

[80] S. Weimann, M. Kremer, Y. Plotnik, Y. Lumer, S. Nolte, K. G. Makris, M. Segev, M. C. Rechtsman, and A. Szameit. Topologically protected bound states in photonic parity-time-symmetric crystals. *Nature Materials*, 16(4):433, 2016.

[81] L. J. Maczewsky, J. M. Zeuner, S. Nolte, and A. Szameit. Observation of photonic anomalous Floquet topological insulators. *Nature Communications*, 8:13756, 2017.

[82] J. Noh, S. Huang, K. P. Chen, and M. C. Rechtsman. Observation of Photonic Topological Valley Hall Edge States. *Physical Review Letters*, 120(6):063902, 2018.

[83] J. Guglielmon, S. Huang, K. P. Chen, and M. C. Rechtsman. Photonic realization of a transition to a strongly driven Floquet topological phase. *Physical Review A*, 97(3):031801, 2018.

[84] L. J Maczewsky, B. Höckendorf, M. Kremer, T. Biesenthal, M. Heinrich, A. Alvermann, H. Fehske, and A. Szameit. Fermionic time-reversal symmetry in a photonic topological insulator. *arXiv preprint, arXiv:1812.07930*, 2018.

[85] K. v. Klitzing, G. Dorda, and M. Pepper. New method for high-accuracy determination of the fine-structure constant based on quantized hall resistance. *Physical Review Letters*, 45(6):494, 1980.

[86] K. von Klitzing. The quantized Hall effect. *Reviews of Modern Physics*, 58(3):519, 1986.

[87] R. B. Laughlin. Quantized Hall conductivity in two dimensions. *Physical Review B*, 23(10):5632, 1981.

[88] D. J. Thouless. Quantization of particle transport. *Physical Review B*, 27(10):6083, 1983.

[89] M. Z. Hasan and C. L. Kane. Colloquium: Topological insulators. *Reviews of Modern Physics*, 82(4):3045, 2010.

[90] C. L. Kane and E. J. Mele. A New Spin on the Insulating State. *Science*, 314(5806):1692, 2006.

[91] M. König, S. Wiedmann, C. Brüne, A. Roth, H. Buhmann, L. W. Molenkamp, X.-L. Qi, and S.-C. Zhang. Quantum Spin Hall Insulator State in HgTe Quantum Wells. *Science*, 318(5851):766, 2007.

[92] A. Kitaev. Periodic table for topological insulators and superconductors. In *AIP Conference Proceedings*, volume 1134, pages 22–30. AIP, 2009.

[93] K. Kawabata, K. Shiozaki, M. Ueda, and M. Sato. Symmetry and Topology in Non-Hermitian Physics. *arXiv preprint, arXiv:1812.09133*, 2018.

[94] B. A. Bernevig and T. L. Hughes. *Topological insulators and topological superconductors*. Princeton university press, 2013.

[95] J. K. Asbóth, L. Oroszlány, and A. Pályi. A Short Course on Topological Insulators. *Lecture Notes in Physics*, 919, 2016.

[96] F. D. M. Haldane. Model for a Quantum Hall Effect without Landau Levels: Condensed-Matter Realization of the "Parity Anomaly". *Physical Review Letters*, 61(18):2015, 1988.

[97] NobelPrize.org. Nobel Media AB 2019. F. Duncan M. Haldane – Biographical. https://www.nobelprize.org/prizes/physics/2016/haldane/biographical/, 2019 (accessed 03.06.2019).

[98] M. V. Berry. Quantal phase factors accompanying adiabatic changes. *Proceedings of the Royal Society of London A*, 392(1802):45, 1984.

[99] D. Xiao, Mi.-C. Chang, and Q. Niu. Berry phase effects on electronic properties. *Reviews of Modern Physics*, 82(3):1959, 2010.

[100] J. Zak. Berry's phase for energy bands in solids. *Physical Review Letters*, 62(23):2747, 1989.

[101] H. M. Price, T. Ozawa, and I. Carusotto. Quantum Mechanics with a Momentum-Space Artificial Magnetic Field. *Physical Review Letters*, 113(19):190403, 2014.

[102] G. Floquet. Sur les équations différentielles linéaires à coefficients périodiques. *Annales scientifiques de l'École Normale Supérieure*, 12:47, 1883.

[103] J. H. Shirley. Solution of the Schrödinger equation with a Hamiltonian periodic in time. *Physical Review*, 138(4B):B979, 1965.

[104] A. Gómez-León and G. Platero. Floquet-Bloch theory and topology in periodically driven lattices. *Physical Review Letters*, 110(20):200403, 2013.

[105] M. Holthaus. Floquet engineering with quasienergy bands of periodically driven optical lattices. *Journal of Physics B*, 49(1):013001, 2016.

[106] A. Eckardt. Colloquium: Atomic quantum gases in periodically driven optical lattices. *Reviews of Modern Physics*, 89(1):011004, 2017.

[107] T. Oka. Floquet theory of photo-induced topological phase transitions: Application to graphene. http://www2.yukawa.kyoto-u.ac.jp/~nqs2011/archive/PresenFiles/WS-E/1207/Oka.pdf, 2011 (accessed 05.08.2019).

[108] M. S. Rudner, N. H. Lindner, E. Berg, and M. Levin. Anomalous edge states and the bulk-edge correspondence for periodically driven two-dimensional systems. *Physical Review X*, 3(3):031005, 2013.

[109] D. Leykam, M. C. Rechtsman, and Y. D. Chong. Anomalous Topological Phases and Unpaired Dirac Cones in Photonic Floquet Topological Insulators. *Physical Review Letters*, 117(1):013902, 2016.

[110] T. Mikami, S. Kitamura, K. Yasuda, N. Tsuji, T. Oka, and H. Aoki. Brillouin-Wigner theory for high-frequency expansion in periodically driven systems: Application to Floquet topological insulators. *Physical Review B*, 93(14):144307, 2016. Reprinted with permission. Copyright (2016) by the American Physical Society.

[111] A. Eckardt and E. Anisimovas. High-frequency approximation for periodically driven quantum systems from a Floquet-space perspective. *New Journal of Physics*, 17(9):093039, 2015.

[112] R. Peierls. Zur Theorie des Diamagnetismus von Leitungselektronen. *Zeitschrift für Physik*, 80(11-12):763, 1933.

[113] A. Alexandrov and H. Capellmann. Energy of electrons on a two-dimensional lattice in a magnetic field: perturbation theory versus "Peierls substitution". *Zeitschrift für Physik B Condensed Matter*, 83(2):237, 1991.

[114] M. Höck. Exakte und approximative Untersuchung kleiner Systeme im Hubbard-Modell. Master's thesis, Universität Bielefeld, 2008.

[115] S. Freund and S. Teufel. Peierls substitution for magnetic Bloch bands. *Analysis & PDE*, 9(4):773, 2016.

[116] F. Letscher. Topologische Zustände in bosonischen Gittermodellen. Diploma thesis, Technische Universität Kaiserslautern, 2014.

[117] J. Fischer. *Three-dimensional optical lithography beyond the diffraction limit.* PhD thesis, Karlsruher Insitut für Technologie, 2012.

[118] J. K. Hohmann, M. Renner, E. H. Waller, and G. von Freymann. Three-Dimensional µ-Printing: An Enabling Technology. *Advanced Optical Materials*, 3(11):1488, 2015.

[119] S. Hengsbach and A. D. Lantada. Direct Laser Writing of Fractal Surfaces: Strategy to Design and Manufacture Textured Materials. *Advanced Engineering Materials*, 17(2):172, 2015.

[120] E. Waller. *Structured light in direct laser writing.* PhD thesis, Technische Universität Kaiserslautern, 2015.

[121] J. Hering. Aufbau und Inbetriebnahme einer SLM-basierten STED-Lithographie. Master's thesis, Technische Universität Kaiserslautern, 2015.

[122] E. H. Waller, M. Renner, and G. von Freymann. Active aberration- and point-spread-function control in direct laser writing. *Optics Express*, 20(22):24949, 2012.

[123] J. Hering, E. H. Waller, and G. von Freymann. Automated aberration correction of arbitrary laser modes in high numerical aperture systems. *Optics Express*, 24(25):28500, 2016.

[124] P. Macak, Y. Luo, P. Norman, and H. Ågren. Electronic and vibronic contributions to two-photon absorption of molecules with multi-branched structures. *The Journal of Chemical Physics*, 113(17):7055, 2000.

[125] Nanoscribe GmbH. Photonic Professional (GT) User Manual, 2017.

[126] Märzhäuser. Scan IM 130x100, 1mm. https://www.marzhauser.com/de/pim/produktdetail-popup.html?view=details&pimid=a223&no_cache=1&m=null&p=null, (accessed 03.04.2019).

[127] Physik Instrumente. P-563.3CD. https://www.physikinstrumente.de/de/produkte/piezo-nanopositioniertische/mehrachsen-piezotische/p-561-p-562-p-563-pimars-nanopositioniertisch-201550/, (accessed 03.04.2019).

[128] Carl Zeiss MicroImaging GmbH. Operating Manual Axio Observer, Inverted microscope, 2006.

[129] T. Bückmann, N. Stenger, M. Kadic, J. Kaschke, A. Frölich, T. Kennerknecht, C. Eberl, M. Thiel, and M. Wegener. Tailored 3D Mechanical Metamaterials Made by Dip-in Direct-Laser-Writing Optical Lithography. *Advanced Materials*, 24(20):2710, 2012.

[130] Carl Zeiss MicroImaging GmbH. Operating Manual Definite Focus, 2008.

[131] J. S. Oakdale, J. Ye, W. L. Smith, and J. Biener. Post-print UV curing method for improving the mechanical properties of prototypes derived from two-photon lithography. *Optics Express*, 24(24):27077, 2016.

[132] B. Richter. *Selektive Funktionalisierung dreidimensionaler Mikrostrukturen für kontrolliertes Zellwachstum*. Diploma thesis, Karlsruher Institut für Technologie, 2010.

[133] Thorlabs. CCD-Kamera DCC1545m. http://www.thorlabs.de/newgrouppage9.cfm?objectgroup_id=4024&pn=DCC1545M, (accessed 03.04.2019).

[134] Zaber. Linear Actuator T-NA08a25. http://www.zaber.com/products/product_detail.php?detail=T-NA08A25. (accessed 03.04.2019).

[135] Optiwave. OptiBPM Manual. https://optiwave.com/optibpm-manuals/introduction-2/, 2019 (accessed 26.03.2019).

[136] R. O. Umucalilar and I. Carusotto. Artificial gauge field for photons in coupled cavity arrays. *Physical Review A*, 84(4):043804, 2011.

[137] M. Aidelsburger, S. Nascimbene, and N. Goldman. Artificial gauge fields in materials and engineered systems. *Comptes Rendus Physique*, 19(6):394, 2018.

[138] M. C. Rechtsman, J. M. Zeuner, A. Tünnermann, S. Nolte, M. Segev, and A. Szameit. Strain-induced pseudomagnetic field and photonic Landau levels in dielectric structures. *Nature Photonics*, 7(2):153, 2012.

[139] M.-I. Cohen, Y. Lumer, H. Herzig-Sheinfux, Y. Plotnik, J. Nemirovsky, and M. Segev. Reflection and refraction in artificial photonic gauge fields. In *Conference on Lasers and Electro-Optics*, page FM3G.4. Optical Society of America, 2017.

[140] K. Fang and S. Fan. Controlling the Flow of Light Using the Inhomogeneous Effective Gauge Field that Emerges from Dynamic Modulation. *Physical Review Letters*, 111(20):203901, 2013.

[141] M.-I. Cohen, C. Jörg, Y. Lumer, Y. Plotnik, E. H. Waller, J. Schulz, G. von Freymann, and M. Segev. Experimental Observation of Generalized Snell's Law at an Interface Between Different Photonic Artificial Gauge Fields. (in preparation).

[142] Link to the videos. Videos of the measurements for chapter 4, OptiBPM calculations for chapter 5, and the numerical tight-binding calculations for section 6.3, can be found under the following link:. https://seafile.rlp.net/d/f1e8f55d532d4c7089d1/.

[143] NKT Photonics. SuperK EVO. https://www.nktphotonics.com/lasers-fibers/product/superk-evo-supercontinuum-laser/, (accessed 23.11.2018).

[144] J. A. Kurvits, M. Jiang, and R. Zia. Comparative analysis of imaging configurations and objectives for Fourier microscopy. *Journal of the Optical Society of America A*, 32(11):2082, 2015.

[145] S. Dottermusch, D. Busko, M. Langenhorst, U. W. Paetzold, and B. S. Richards. Exposure-dependent refractive index of Nanoscribe IP-Dip photoresist layers. *Optics Letters*, 44(1):29, 2019.

[146] A. Slobozhanyuk, S. H. Mousavi, X. Ni, D. Smirnova, Y. S. Kivshar, and A. B. Khanikaev. Three-dimensional all-dielectric photonic topological insulator. *Nature Photonics*, 11(2):130, 2017.

[147] Y. T. Katan, Y. Lumer, Y. Plotnik, M. Rechtsman, and M. Segev. Photonic Topological Edge Modes without an Edge. In *Conference on Lasers and Electro-Optics*, page FTu4C.7. Optical Society of America, 2015.

[148] F. Piccioli, L. J. Maczewsky, M. Kremer, M. Heinrich, and A. Szameit. Switching light at the interface between anomalous Floquet topological insulators. In *Conference on Lasers and Electro-Optics*, page FW3D.8. Optical Society of America, 2019.

[149] V. Dal Lago, M. Atala, and L. E. F. Foa Torres. Floquet topological transitions in a driven one-dimensional topological insulator. *Physical Review A*, 92:023624, 2015.

[150] O. Balabanov and H. Johannesson. Robustness of symmetry-protected topological states against time-periodic perturbations. *Physical Review B*, 96(3):035149, 2017.

[151] S. A. Reyes, D. Thuberg, D. Pérez, C. Dauer, and S. Eggert. Transport through an AC-driven impurity: Fano interference and bound states in the continuum. *New Journal of Physics*, 19(4):043029, 2017.

[152] H. Li, T. Kottos, and B. Shapiro. Driving-induced metamorphosis of transport in arrays of coupled resonators. *Physical Review A*, 97(2):023846, 2018.

[153] Z. Fedorova (Cherpakova), C. Jörg, C. Dauer, F. Letscher, M. Fleischhauer, S. Eggert, S. Linden, and G. von Freymann. Limits of topological protection under local periodic driving. *Light: Science & Applications*, 8(1):63, 2019.

[154] M. Atala, M. Aidelsburger, J. T. Barreiro, D. Abanin, T. Kitagawa, E. Demler, and I. Bloch. Direct measurement of the Zak phase in topological Bloch bands. *Nature Physics*, 9(12):795, 2013.

[155] Creative Commons public license. CC BY 4.0. https://creativecommons.org/licenses/by/4.0/legalcode, (accessed 07.08.2019).

[156] K. Thyagarajan, M. R. Shenoy, and A. K. Ghatak. Accurate numerical method for the calculation of bending loss in optical waveguides using a matrix approach. *Optics Letters*, 12(4):296, 1987.

[157] P. Titum, N. H. Lindner, M. C. Rechtsman, and G. Refael. Disorder-Induced Floquet Topological Insulators. *Physical Review Letters*, 114(5):056801, 2015.

[158] S. Stützer, Y. Plotnik, Y. Lumer, P. Titum, N. H. Lindner, M. Segev, M. C. Rechtsman, and A. Szameit. Photonic topological Anderson insulators. *Nature*, 560(7719):461, 2018.

[159] M. Padgett, J. Courtial, and L. Allen. Light's Orbital Angular Momentum. *Physics Today*, 57(5):35, 2004. Reproduced with the permission of the American Institute of Physics.

[160] L. Marrucci, C. Manzo, and D. Paparo. Pancharatnam-Berry phase optical elements for wave front shaping in the visible domain: Switchable helical mode generation. *Applied Physics Letters*, 88(22):221102, 2006.

[161] M. W. Beijersbergen, R. P. C. Coerwinkel, M. Kristensen, and J. P. Woerdman. Helical-wavefront laser beams produced with a spiral phaseplate. *Optics Communications*, 112(5):321, 1994.

[162] L. Zhu and J. Wang. Arbitrary manipulation of spatial amplitude and phase using phase-only spatial light modulators. *Scientific Reports*, 4:7441, 2014.

[163] A. Ashkin. Acceleration and Trapping of Particles by Radiation Pressure. *Physical Review Letters*, 24(4):156, 1970.

[164] D. Gao, W. Ding, M. Nieto-Vesperinas, X. Ding, M. Rahman, T. Zhang, C. Lim, and C.-W. Qiu. Optical manipulation from the microscale to the nanoscale: fundamentals, advances and prospects. *Light: Science & Applications*, 6(9):e17039, 2017.

[165] S. W. Hell and J. Wichmann. Breaking the diffraction resolution limit by stimulated emission: stimulated-emission-depletion fluorescence microscopy. *Optics Letters*, 19(11):780, 1994.

[166] T. A. Klar and S. W. Hell. Subdiffraction resolution in far-field fluorescence microscopy. *Optics Letters*, 24(14):954, 1999.

[167] R. Wollhofen, J. Katzmann, C. Hrelescu, J. Jacak, and T. A. Klar. 120 nm resolution and 55 nm structure size in STED-lithography. *Optics Express*, 21(9):10831, 2013.

[168] M. J. Padgett. Orbital angular momentum 25 years on. *Optics Express*, 25(10):11265, 2017.

[169] G. Pelegrí, A. M. Marques, R. G. Dias, A. J. Daley, J. Mompart, and V. Ahufinger. Topological edge states and Aharanov-Bohm caging with ultracold atoms carrying orbital angular momentum. *Physical Review A*, 99(2):023613, 2019. Reprinted with permission. Copyright (2019) by the American Physical Society.

[170] G. Pelegrí , A. M. Marques, R. G. Dias, A. J. Daley, V. Ahufinger, and J. Mompart. Topological edge states with ultracold atoms carrying orbital angular momentum in a diamond chain. *Physical Review A*, 99(2):023612, 2019. Reprinted with permission. Copyright (2019) by the American Physical Society.

[171] J. Polo, J. Mompart, and V. Ahufinger. Geometrically induced complex tunnelings for ultracold atoms carrying orbital angular momentum. *Physical Review A*, 93(3):033613, 2016.

[172] G. Pelegrí, J. Polo, A. Turpin, M. Lewenstein, J. Mompart, and V. Ahufinger. Single-atom edgelike states via quantum interference. *Physical Review A*, 95(1):013614, 2017.

[173] A. Turpin, G. Pelegrí, J. Polo, J. Mompart, and V. Ahufinger. Engineering of orbital angular momentum supermodes in coupled optical waveguides. *Scientific Reports*, 7:44057, 2017.

[174] C. N. Alexeyev, N. A. Boklag, and M. A. Yavorsky. Higher order modes of coupled optical fibres. *Journal of Optics*, 12(11):115704, 2010.

[175] C. N. Alexeyev, N. A. Boklag, T. A. Fadeyeva, and M. A. Yavorsky. Tunnelling of orbital angular momentum in parallel optical waveguides. *Journal of Optics*, 13(6):064012, 2011.

[176] K. Y. Bliokh, F. J. Rodríguez-Fortuño, F. Nori, and A. V. Zayats. Spin-orbit interactions of light. *Nature Photonics*, 9(12):796, 2015.

[177] B. Mao, Y. Liu, H. Zhang, K. Yang, Y. Han, Z. Wang, and Z. Li. Complex analysis between CV modes and OAM modes in fiber systems. *Nanophotonics*, 8(2):271, 2018.

[178] MICROCHEM. KMPR®1000. http://www.microchem.com/pdf/KMPRDataSheetver4_2a.pdf, 2019 (accessed 15.07.2019).

[179] A. Žukauskas, I. Matulaitienė, D. Paipulas, G. Niaura, M. Malinauskas, and R. Gadonas. Tuning the refractive index in 3d direct laser writing lithography: towards GRIN microoptics. *Laser & Photonics Reviews*, 9(6):706, 2015.

[180] OmniCure®. S2000 Spot UV Curing System. https://www.excelitas.com/product/omnicure-s2000-spot-uv-curing-system, 2019 (accessed 15.07.2019).

[181] Y. Chen, J. Gao, Z.-Q. Jiao, K. Sun, W.-G. Shen, L.-F. Qiao, H. Tang, X.-F. Lin, and X.-M. Jin. Mapping Twisted Light into and out of a Photonic Chip. *Physical Review Letters*, 121(23):233602, 2018.

[182] Y. Lumer, M. C. Rechtsman, Y. Plotnik, and M. Segev. Instability of bosonic topological edge states in the presence of interactions. *Physical Review A*, 94(2):021801, 2016.

[183] D. A. Zezyulin, H. Ott, and V. V. Konotop. Coherent perfect absorber and laser for nonlinear waves in optical waveguide arrays. *Optics Letters*, 43(23):5901, 2018.

Publications

Parts of this thesis have been published in scientific journals and presented on international conferences.

Publications in scientific journals (peer-reviewed):

[57]: C. Jörg, F. Letscher, M. Fleischhauer, and G. von Freymann: Dynamic defects in photonic Floquet topological insulators, *New J. Phys.* 19, 083003 (2017).

[153]: Z. Feodorova (Cherpakova)*, C. Jörg*, C. Dauer, F. Letscher, M. Fleischhauer, S. Eggert, S. Linden, and G. von Freymann: Limits of topological protection under local periodic driving, *Light, Science and Applications* 8, 63 (2019).

* contributed equally

Other publications:

[60] C. Jörg, Erste Schritte in Richtung optischer topologischer Isolatoren durch direktes Laserschreiben, Diploma thesis, TU Kaiserslautern (2015).

Conference contributions (as speaker/presenter; selected):

Invited talk

Christina Jörg, Zlata Cherpakova, Fabian Letscher, Christoph Dauer, Julian Schulz, Sebastian Eggert, Michael Fleischhauer, Stefan Linden, Georg von Freymann: Waveguides for Quantum Optics: 3D-Micro-Printing and Topological Insulators. Universidad Autonoma de Barcelona, Spain, 2018

Talks

Christina Jörg, Christoph Dauer, Fabian Letscher, Michael Fleischhauer, Sebastian Eggert, and Georg von Freymann: Limits of topological protection. CLEO 2019, San Jose, USA

Christina Jörg, Moshe-Ishay Cohen, Yaakov Lumer, Yonatan Plotnick, Mordechai Segev, and Georg von Freymann: Refraction and reflection at an interface between two artificial photonic gauge fields. DPG spring meeting 2019, Rostock, Germany

Christina Jörg, Christoph Dauer, Fabian Letscher, Michael Fleischhauer, Sebastian Eggert, and Georg von Freymann: 3D printed photonic topological insulators, topological edge modes and time-periodic driving. SPIE Photonics West 2019, San Francisco, USA

Christina Jörg, Christoph Dauer, Fabian Letscher, Michael Fleischhauer, Sebastian Eggert, and Georg von Freymann: Transitions between States in Topological Waveguide Systems by Local Time-Periodic Driving, NANOP 2018, Rome, Italy

Christina Jörg, Fabian Letscher, Christoph Dauer, Axel Pelster, Sebastian Eggert, Michael Fleischhauer, Georg von Freymann: Driving Transitions between States in Topological Systems. DPG spring meeting 2018, Erlangen, Germany

Christina Jörg, Fabian Letscher, Michael Fleischhauer, and Georg von Freymann: Temporal Defects in Photonic Topological Insulators. CLEO 2017, San Jose, USA

Christina Jörg, Fabian Letscher, Michael Fleischhauer, and Georg von Freymann: Time-dependent defects in photonic topological insulators. DPG spring meeting 2017, Dresden, Germany

Posters

Christina Jörg, Zlata Cherpakova, Christoph Dauer, Fabian Letscher, Michael Fleischhauer, Sebastian Eggert, Stefan Linden and Georg von Freymann: Stability of topological edge mode under time-periodic driving. ToCoTronics 2018, Würzburg, Germany

Christina Jörg, Fabian Letscher, Michael Fleischhauer, and Georg von Freymann: Dynamic Defects in Photonic Floquet Topological Insulators. DIscrete, Nonlinear and Disordered OpticS (DINDOS17), Dresden, Germany

Christina Jörg, Fabian Letscher, Michael Fleischhauer, and Georg von Freymann: Waveguides for quantum simulation: Time-dependent defects in photonic topological insulators. 634. WE-Heraeus-Seminar: Merging Micro- and Nano-Optics: 3D Printing of Advanced and Functional Optics, Bad Honnef, 2017.

Curriculum Vitae

Hochschulstudium

10/2009–04/2015	Technische Universität Kaiserslautern, Diplomstudiengang Physik
01/2013–07/2013	Erasmus Semester an der Universidade de Santiago de Compostela (Spanien)
04/2015	Abschluss Diplom-Physik (mit Auszeichnung) Diplomarbeit mit dem Titel "Erste Schritte in Richtung optischer topologischer Isolatoren durch direktes Laserschreiben" Arbeitsgruppe von Prof. Dr. Georg von Freymann, Technische Universität Kaiserslautern

Promotion

seit 06/2015	Promotion zum Thema "Interfaces and defects in topological model systems of 3D micro-printed waveguides" Arbeitsgruppe von Prof. Dr. Georg von Freymann, Technische Universität Kaiserslautern

Danksagung

Ich möchte mich ganz herzlich bei allen bedanken, die zum Gelingen dieser Arbeit beigetragen haben:

- bei Prof. Dr. Georg von Freymann für die gute Betreuung, die Freiheit bei der Ausgestaltung des Themas und das Ermöglichen so vieler Konferenzbesuche.
- bei Prof. Dr. Michael Fleischhauer für die gute Zusammenarbeit und die Übernahme des Zweitgutachtens.
-bei allen ehemaligen und aktuellen Kolleginnen und Kollegen der Arbeitsgruppe. Besonders bei Peter, der immer eine schnelle Lösung für alle technischen Wünsche hat, und bei Heike, ohne die uns die Bürokratie über den Kopf wachsen würde. Auch an Erik und Julian geht besonderer Dank für das Einkoppeln des Lasers ins DLW.
- an Julian Schulz, für unheimlich hilfreiche Teamarbeit und Diskussionen. Es hat Spaß gemacht mit dir zu arbeiten.
- Großen Dank an Christoph Dauer und Fabian Letscher für unzählige Theorie-Diskussionen und die gute Zusammenarbeit.
- I want to give thanks to everyone I worked with on projects: Zlata Feodorova, Moshe-Ishay Cohen, Gerard Queralto, Mark Kremer, and corresponding group leaders. To all the nice people who made working on this thesis interesting and fun. And to anyone answering my countless questions with patience.
- A big thank you to the people that proof-read the thesis for your helpful comments.
- Danke an die Kollegen aus der Biologie für die überlassenen Patch-Clamps zum Infiltrieren der Proben.
- beim NSC-Team für die Benutzung der Ausstattung und hilfreichen Ratschläge.
- an Freunde und Familie für Geduld, Verständnis und Unterstützung. Danke!